5-2018

Polymer-based Piezoelectric Material and Device for Energy Harvesting/Health Monitoring in Civil Infrastructure

Eshan Ghafari
Purdue University

POLYMER-BASED PIEZOELECTRIC MATERIAL AND DEVICE FOR ENERGY HARVESTING AND SENSING IN CIVIL INFRASTRUCTURE
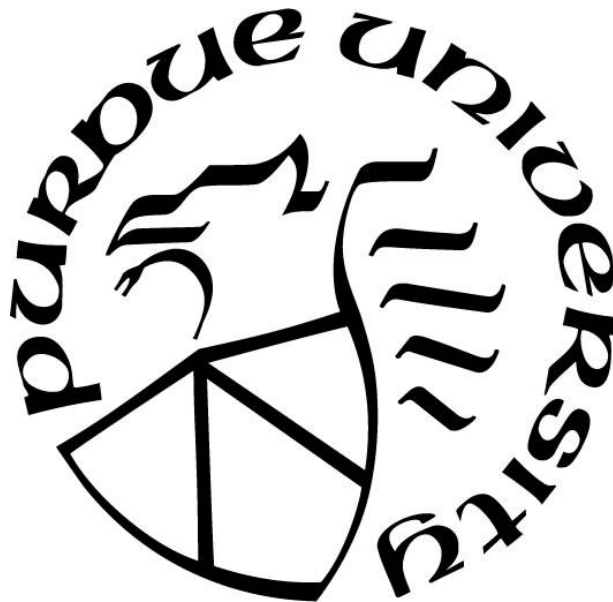
by

Eshan Ghafari

A Dissertation

Submitted to the Faculty of Purdue University

In Partial Fulfillment of the Requirements for the degree of

Doctor of Philosophy

Lyles School of Civil Engineering

West Lafayette, Indiana

May 2018

THE PURDUE UNIVERSITY GRADUATE SCHOOL
STATEMENT OF COMMITTEE APPROVAL

Dr. Na (Luna) Lu, Chair

      Lyles School of Civil Engineering

Dr. Jan Olek

      Lyles School of Civil Engineering

Dr. John Haddock

      Lyles School of Civil Engineering

Dr. Jeffrey Youngblood

      Department of Material Engineering

Approved by:

      Dr. Dulcy Abraham

        Head of the Graduate Program

ACKNOWLEDGEMENTS

TABLE OF CONTENTS

LIST OF FIGURES

LIST OF TABLES

ABBREVIATIONS

AE	Acoustic emission
AFM	Atomic force microscopy
ANOVA	Analysis of variance
CNT	Carbon nanotubes
FTIR	Fourier transform infrared spectroscopy
GO	Graphene oxide
HCNFES	Hollow cylindrical near-field electrospinning
IDT	Interdigitated transducer
MWCNT	Multiwalled carbon nanotube
NWS	Near distance-wheeling
PFM	Piezoelectric force microscopy technique
PR	Photoresist
PVDF	Polyvinylidene fluoride
PVDF-TrFE	Polyvinylidene fluoride trifluoroethylene
PZT	Lead zirconate titanate
RSM	Response surface method
SWCNT	Single-walled carbon nanotubes
SCCO$_2$	Supercritical carbon dioxide
Vpp	Voltage peak to peak
XRD	X-ray diffraction analysis

ABSTRACT

Author: Ghafari, Ehsan. Ph.D.
Institution: Purdue University
Degree Received: May 2018
Title: Polymer-Based Piezoelectric Material and Device for Energy Harvesting and Sensing in Civil Infrastructure
Committee Chair: Na Lu

Recent studies on piezoelectric materials have resulted in the development of a wide verity of piezoelectric devices such as nanogenerators and sensors. This technology is prevalently dominated by the ceramic materials which are brittle and have a very limited strain level. Moreover, despite a wide working frequency range, the ceramic-based piezoelectric devices can only work under tiny forces to avoid damage to the device. As such, due to inherent brittleness, the piezoelectric technology has not been widely explored in civil engineering applications due to the aforementioned drawbacks of ceramic materials. This thesis aims to develop an efficient piezoelectric polyvinylidene fluoride (PVDF) nanofiber device which can be used in both energy harvesting and sensing civil infrastructure applications. The β-phase of PVDF is responsible for its electroactive properties such as ferroelectric, piezoelectric and pyroelectric properties. In spite of several efforts to improve the β-phase content, it is still a challenge to fabricate a PVDF sensor with high efficiency due to the complication of the required post-treatment process which mainly includes electrical poling and mechanical stretching. The electrospinning method was used in this study to synthesize the cost-effective and large-scale piezoelectric nanofiber composite, making it feasible for commercial, industrial and civil engineering applications. The process-structure-property relations of electrospun PVDF nanofiber has been systematically studied. As a result, a reliable model was developed that enables an accurate prediction of PVDF structure properties, particularly morphological and a fraction of the β-phase content. It was found that the fraction of β-phase is considerably affected by evaporation rate so that the high concentration of PVDF and DMF/acetone decreases the evaporation rate of the solution resulting in a formation of a high fraction β-phase content. The electrospinning method was found to be very effective to promote the β-phase formation in PVDF nanofiber. Additionally, electrospun PVDF nanofibers were experienced high electrical field and mechanical stretching during the fabrication which eliminates a need for the post-treatment process.

This study proposes a core-shell structured PVDF-graphene oxide (GO) nanofiber composite, in which the polar phase content and piezoelectric properties are considerably improved. The results indicate that only 0.2 wt. % of GO is enough to nucleate most of the PVDF polymer chain. It was found that the β-phase content in core-shell structured PVDF-GO nanofiber composite can reach up to 92 % for which is 23% and 73% higher that of electrospun PVDF and spin coated PVDF, respectively. This suggests that the core-shell structure of PVDF-GO is effective in improving the phase transformation of α-phase to β-phase, even at a low content of GO. As an interior core-shell, the GO is solidified into nanofiber form which increases the number of heterogeneous nucleation sites to interact with the PVDF polymer chain. The d_{33} piezoelectric coefficient of PVDF-GO was found to be 61 pm/V which is almost two times higher than PVDF nanofiber. The enhancement of the piezoelectric coefficient can be attributed to the higher β-phase content which can induce a stronger displacement in the sample as a result of the applied electrical field. This might be because of the interaction between the π-bond in GO with the fluorine atoms and hydrogen atoms on adjacent carbon atoms in PVDF polymer chains. The alignment of atoms at two sides of the polymer chain not only induces the beta phase formation but also results in a formation of a net polarized dipole moment along the core-shell structure of PVDG-GO nanofiber. The feasibility of using PVDF device for energy harvesting and sensing applications was assessed by a series of experiments. According to the results, the optimized frequency range for the device was found to be 45 Hz. The results indicated that the voltage output starts to decay at a higher frequency which can be due to the insufficient time for the PVDF nanofiber to be recovered from the induced strain. The variation of the amplitude has a great influence on the voltage output of the piezoelectric device. The voltage output of the PVDF device is enhanced with increasing the amplitude due to the higher amount of induced strain. In fact, the amount of induced strain can be considered as the main source of the available mechanical energy which can be fed into the piezoelectric device to be converted to the electrical energy. The results clearly show that both frequency and amplitude can affect the voltage output of the piezoelectric device. The highest obtained voltage output can be obtained at the frequency range between 30-45 Hz. The sensing ability of the PVDF device was assessed in both active and passive situations. A pitch-catch system was set up in the lab to assess the efficiency of the flexible PVDF device for active sensing application. A series of experiments were conducted to evaluate the effect of several parameters of the transmitted signal such as amplitude and frequency on the received signal. The effect of transducer-sensor distance was also considered to evaluate the

attenuation of the transmitted signal. The PVDF sensor was found to be effective in detecting the pulsed and continuous generated Lamb wave.

It was found that the efficiency of the PVDF sensor in detecting the signal is not sensitive to the amplitude of the transmitted signal. Also, the transmitted signal's amplitude has an insignificant effect on the attenuation rate of the transmitted signal over the distance. It means that the efficiency of the PVDF sensor in detecting the Lamb wave signal is not affected by the amplitude of the transmitted signal. However, the efficiency of the PVDF sensor to detect the transmitted signal is highly affected by the distance between the transducer and receiver. The results indicate that the PVDF device is less efficient in detecting the transmitted signal either at a low-frequency range (<1 kHz) or the higher range of frequency (> 100 kHz). The optimized frequency was found to be in the range of 1 kHz to 100 kHz to enhance the efficiency of the PVDF sensor. The efficiency of PVDF sensor for detecting the acoustic wave was also studied by hammer impact testing. These results clearly indicate that the sensor is able to detect different magnitudes of surface acoustic waves propagating on the surface. The higher of the impact energy applied to the concrete, the higher the voltage generated by electrospun PVDF AE sensor. The results of this thesis can assist in adopting the electrospun PVDF piezoelectric sensor in a variety of sensing and energy harvesting applications in civil engineering infrastructure.

CHAPTER 1.   INTRODUCTION

1.1   Background and motivation

Recently piezoelectric materials have been extensively investigated due to their ability to convert mechanical energy into electricity, or vice versa. This unique property is known as piezoelectricity. Recent studies on piezoelectric materials have resulted in the development of a wide verity of piezoelectric devices such as nanogenerators and sensors. Piezoelectricity is an electromechanical interaction between the mechanical and electrical energy. Piezoelectric materials have the ability to produce electrical energy from mechanical energy; for example, they can convert mechanical behavior like vibrations into electricity. This effect is called "direct effect" in which the electric charge develops as a result of the mechanical stress. This effect has been applied to develop several devices such as energy harvester device which can be used in applications where outside power is unavailable, and batteries are not a feasible option. The energy harvester nanogenerator can also be used as an individual power source for small electronic devices [1-12]. In civil engineering, this can be applied to power the wireless sensor for health monitoring the bridges. Another application of the use of the direct effect is for sensing applications such as acoustic sensors, pressure sensors, strain sensor, etc. Such sensors have been widely used in many civil engineering applications. Likewise, the material will experience a geometric change when an electrical signal is applied to it. This effect is referred to "inverse effect" in which a mechanical force such as vibration develops due to the application of an electric field. A typical example of using inverse piezoelectric effect is transducers which are mainly used for structural purposes.

One-dimensional (1D) inorganic piezoelectric materials have attained considerable progress toward developing nanogenerators and potential applications. Wang *et al.* developed a nanogenerator using ZnO nanowire for energy harvesting application [13]. Recent researches have indicated significant progress towards developing high-performance ceramic nanogenerator using lead zirconate titanate (PZT) [14; 15]. PZT patch has been widely used in structural health monitoring applications in civil engineering infrastructure [16]. The major drawback of PZT, however, is their brittleness so that they can have a very limited strain level. This is a major obstacle for the use of these materials either in into flexible electronic devices or in high strain level applications. Moreover, in spite of a wide working frequency range of PZT, the PZT-based piezoelectric devices work only under tiny forces to avoid damage to the device [17]. The polymer

nanofibers on the other hands have shown good ability to harvest the mechanical force under high strain conditions, due to their excellent flexibility and process simplicity as compared to inorganic nanowires. Nanofibers have higher strain level which enables them to withstand larger mechanical deformations [18]. Among the known piezoelectric polymer materials, polyvinylidene fluoride (PVDF) is the only commercial product used as a piezoelectric material, due to its high flexibility, high piezoelectric properties, and good mechanical properties. Therefore, this flexible polymeric piezoelectric is a good candidate to be used in civil engineering application. The voltage coefficient of PVDF is 10 times higher than the ceramic material which makes it as an exceptional candidate for sensing applications [19; 20]. Also, PVDF polymer shows much lower density and acoustic impedance than piezoelectric crystals, which make them suitable for acoustic sensing applications [19-21]. The β-phase of PVDF is responsible for its electroactive properties such as ferroelectric, piezoelectric and pyroelectric properties. It has been reported that the sensitivity of PVDF sensors is related to the content of β-phase so that the higher β-phase will result in a better sensitivity of the sensor [22; 23]. Hence, the enhancement of β-phase of PVDF is a critical step for making an efficient PVDF piezoelectric sensor. In spite of several efforts to improve the β-phase content, it is still a challenge to fabricate a PVDF sensor with high efficiency due to the complication of the required post-treatment process which mainly includes electrical poling and mechanical stretching. These processes are costly and time-consuming which limits the scalable production of nanogenerators/sensor in the industrial fabrication process. Nevertheless, the mechanical vibrations can be very large in many cases such as civil infrastructure applications; e.g. pavement, the cable-stayed bridges, skyscrapers, railway tracks, etc. An efficient and scalable piezoelectric device is therefore needed which can be either used as an energy harvester to capture the mechanical vibration or as a robust sensor to monitor the structural behaviors in civil infrastructure applications.

In this scope, this thesis aims to develop an efficient piezoelectric nanofiber device which can be used in both energy harvesting and civil infrastructure sensing applications. The electrospinning method is used for the synthesis of a cost-effective, large-scale and efficient piezoelectric nanofiber composite, making it considerably more attractive for commercial industrial and civil engineering applications.

1.2   Objectives and Methodology

The goal of this thesis is to design, develop and engineer electrospun PVDF nanofibers and investigate its feasibility in energy harvesting and sensing applications in civil infrastructure. To achieve this goal, four major research objectives are studied in this program; details are listed as below:

1) Investigate process-structure-property relationship of electrospun PVDF nanofiber

In this thesis, PVDF nanofiber is fabricated using the electrospinning method through a sol-gel approach. The electrospinning method has been found to be an efficient tool to enhance the β-phase and piezoelectric properties of PVDF via in situ electrical poling and mechanical stretching of nanofiber during the fabrication process [17; 24-27]. However, the contradictory results were reported by some researchers to indicate that the electrospinning method has failed to promote the formation of β-phase [14; 28-31]. Therefore, a post-poling treatment was required to make the molecular dipoles oriented along the fiber length direction. Although the electrospinning process appears to be technically straightforward, several processing variables need to be well understood and optimized in order to fabricate nanofibers with the desired properties such as uniformity, alignment, β-phase and beads-less formation. Up to now, the conventional method to fabricate the electrospun PVDF nanofiber has been used, in which the interdependence of each processing parameter on nanofiber characteristics are overlooked since this method only involves changing one of the electrospinning process parameters while keeping the others fixed at certain values. As results, the conventional methods do not provide a reliable model to predict and optimize the properties of PVDF nanofiber. Therefore, it is important to develop a comprehensive and reliable model to elucidate the effect of the electrospinning processing parameters on the morphology and the β-phase formation of electrospun PVDF nanofiber. On the modeling part, the response surface methodology (RSM) has been approved as a powerful experimental design technique for the modeling and analysis of problems in which a response of interest is influenced by several variables [32-36]. Hence, this task aims to develop a robust model to investigate the effect of electrospinning process parameters on the morphology and crystallinity of PVDF nanofiber. A response surface model is proposed to predict the size, the probability of the beads formation, and the fraction of the β-phase content of electrospun PVDF nanofiber. In addition, the proposed model can be used to assess the effect of each electrospinning process parameters as well as the interdependencies of all parameters. Finally, a multi-objective numerical optimization

technique will be used to achieve a beads-free PVDF nanofiber and simultaneously with the maximum of β-phase content. The optimized parameters are identified and considered in the fabrication process of the piezoelectric device.

2) Investigate the fundamental mechanism of β-phase formation and the effective approaches to enhance the β-phase content in PVDF nanofiber

The β-phase of PVDF is responsible for its electroactive properties such as ferroelectric, piezoelectric and pyroelectric properties. The PVDF polymer chains in the unit cell of β-phase are arranged in a way that all the dipoles are aligned in a parallel manner leading to a net dipole moment, which is the strongest amongst all the phases [37]. In order to enhance the β-phase formation of piezoelectric devices, different approaches have been proposed. The electrical poling and mechanical stretching have been mostly used to improve piezoelectric performance due to change the crystallinity of PVDF. However, these processes are costly and time-consuming. Adding materials is another approach to promote the β-phase formation of PVDF. Regarding using additive material approach, the carbon-based materials such as carbon nanotubes (CNT) and graphene oxide (GO) were found to be effective in enhancing the electromechanical properties due to the nucleation effect which can promote crystallinity of the PVDF matrix. So far, these materials were incorporated into the PVDF solution which causes some problems such as agglomeration which limits the dosage of these additives. Although the enhancement of β-phase through adding these additives might induce a higher electrostatic charge potential, the transfer of the static charges has remained a challenge as PVDF is not conductive. The latter further affect the efficiency of the piezoelectric device. As an interior core-shell, the GO is solidified into nanofiber form which can provide a higher surface area to interact with PVDF molecular chain to enhance the β-phase formation. In addition, it is expected that the core-shell structure can prevent the agglomeration of the GO nanoparticles.

This task aims to address these issues by proposing a novel core-shell electrospinning system to enhances the β-phase of the PVDF nanofiber. The interior core consists of graphene oxide which acts as a nucleation site to enhance the β-phase while the exterior shell is responsible for facilitating the transferring of the accumulated static charges. The incorporation of ferroelectric materials tends to enhance the remnant polarization of the piezoelectric device due to the nucleation effect which can promote crystallinity of the PVDF matrix. At the first step, a series of experiments are conducted to investigate the nucleation effect of GO particles for enhancing β-

phase formation of the optimized PVDF. The Fourier transform infrared spectroscopy (FTIR), X-ray diffraction analysis (XRD) are used to study the possible the interaction between the polymer chain and graphene oxide. Secondly, the piezoelectric coefficient and ferroelectric properties of PVDF nanofiber composite are studied using atomic force microscopy (AFM).

3) Design, engineer and fabricate PVDF piezoelectric device

This task aims to evaluate the feasibility of using a PVDF piezoelectric device in both energy harvesting and sensing civil infrastructure applications. In this scope, several subtasks are considered to achieve this goal. This first step is focused on fabrication the device. A Lift-off lithography method is used to fabricate an interdigitated device. The thermal evaporation and e-beam evaporation methods are used to deposit electrode on the electrospun PVDF. The lithography process requires multiples devices and clean room fabrication environments which results in a small-scale PVDF nanogenerator/sensor scale. Thus, it is difficult to scale such designs for mass production, especially in civil engineering application which deals with large scales applications. Hence, an inkjet printing method is also evaluated for device fabrication process.

4) Investigate the feasibility of using electrospun PVDF piezoelectric nanogenerator/sensor for civil engineering applications.

The efficiency of the piezoelectric device is then investigated in both energy harvesting and sensing applications. A mechanical vibration test set up is developed in which the voltage output of nanogenerator with a different frequency is examined. A cantilever beam is simulated by using this set up to investigate the efficiency of the sensor in capturing the mechanical vibration at a different frequency. The lower acoustic impedance of PVDF polymer compared to ceramic materials, make it a good alternative for acoustic sensing applications. The efficiency of the sensor for health monitoring application is also studied. This section aims to investigate the feasibility of using electrospun PVDF nanofiber in both passive and active sensing state. Acoustic emission monitoring is considered as a passive method which can detect sensing acoustic waves generated by acoustic emission source. The pitch-catch approach is also considered for the active sensing approach. In this approach, a piezoelectric transducer acts an actuator to propagates the Lamb waves while another piezoelectric device works as a sensor to detect the signal.

1.3   Thesis Structure

This thesis is organized into five chapters. The details of each chapter are briefly discussed in the following:

Chapter 1 introduces the main thesis objectives and the methodology to achieve the goals.

Chapter 2 contains an extensive literature review of the piezoelectric effect, PVDF synthesis process, approaches to enhance the β-phase, PVDF nanogenerator devices, and PVDF sensor devices.

Chapter 3 presents the fabrication process of PVDF using electrospinning method. This chapter investigates different parameters for fabrication process of electrospun PVDF. The results for the developed RSM model is presented and discussed. A core-shell system is also discussed to promote the formation of β-phase. This chapter presents the results of the piezoelectric coefficient using piezoelectric force microscope technique.

Chapter 4 presents the fabrication process mainly by lift-off lithography and inkjet printing process. The results for energy harvesting application and sensing application of electrospun PVDF nanofiber are also discussed. The last part of this chapter presents the experimental procedure and the results PVDF piezoelectric device as an acoustic emission sensor.

Chapter 5 includes a summary of the conclusion of the thesis and propose some future works.

CHAPTER 2.   LITERATURE REVIEW

2.1.   Fundamental of piezoelectric effect

The "piezo" is derived from the Greek word which means pressure. In 1880 Curie brothers discovered the piezoelectric effect in certain solid crystalline dielectric substances such as quartz. The piezoelectric effect is defined as the relation between the mechanical energy with the electrical energy which originates from the displacement of the ions in the materials with asymmetric crystal structure [38; 39]. They realized that the applied force to quartz produces an electric charge in the crystal. This effect is known as a direct piezoelectric effect. They also discovered that an electric field applied to the quartz results in a deformation of the material which is known as a piezoelectric inverse effect. The piezoelectric devices operate in a variety of applications using the direct and inverse effect. Figure 2-1 shows the schematic of the piezoelectric effect (direct and inverse).
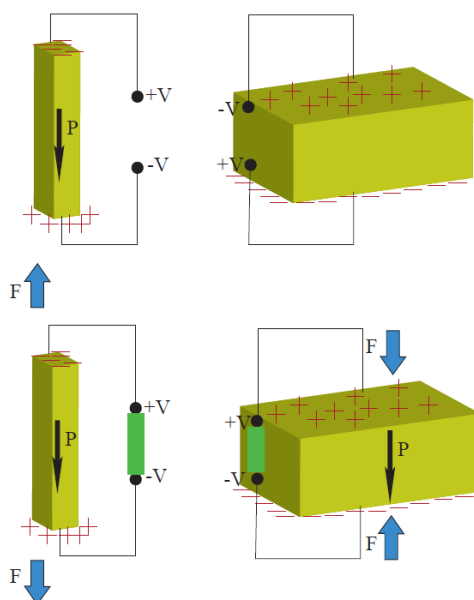
Figure 2-1-A schematic of the piezoelectric device based on the direct effect (left) and inverse effect (right).

The materials that exhibit a significant and useful piezoelectric effect fall under three main groups including 1) natural such as quartz, Rochelle salt; 2) synthetic such as lithium Sulfate and ammonium dihydrogen phosphate; and 3) polarized ferroelectric crystals such as Barium Titanate, Lead Zirconate-titanate. The materials in a natural group exhibit the piezoelectric effect without

further processing such a the post-treatment and poling due to their natural asymmetric structure. However, the crystal materials other than ferroelectric crystals must be artificially polarized by applying a strong electrical field to the material (poling process), while it is heated to a temperature above the Curie point of the material. They are then slowly cooled to the field still applied. When the external field is removed, they have a remnant polarization which allows them to exhibit the piezoelectric effect.

The piezoelectric effect for sensing applications is characterized mainly by calculating the piezoelectric coefficient (d_{ij}), also known as charge constant, where i is the direction of electric effect and j is the direction of mechanical effect. The charge constant is the strain induced by an applied electric field. The piezoelectric coefficient can be calculated using the following equation:

$$d_{ij} = \frac{\text{Strain developed}}{\text{Applied electrical field}} \left(\frac{m}{V}\right) \qquad (2-1)$$

The piezoelectric constitutive establish a relation between the linear elastic properties and linear dielectric properties using the following formula:

$$S_i = S_{ij}^{\ E} T_j + d_{ki} E_k \qquad (2-2)$$

$$D_i = d_{ij} T_j + \varepsilon^T_{\ ik} E_k \qquad (2-3)$$

Where D is electrical displacement, E is an electrical field, S is strain tensor induced by mechanical stress, and T is the stress induced by an electrical field, S^E is the elastic compliance matrix at a constant electric field; ε^T is the permittivity at constant stress [40]. The piezoelectric coefficient of the most common piezoelectric materials is shown in Table 2-1. As can be seen, the PZT shows the highest piezoelectric coefficient as compared to ZnO and PVDF.

Table 2-1- The piezoelectric coefficient of the piezoelectric materials

Materials	d_{33} (pm/V)	Sample	Processing method
PVDF [41]	17.4	Thin film	Spin coating
PVDF [42]	30	Nanofiber	Electrospinning
PZT [43]	330	Thin film	Molecular-beam epitaxy
PZT [44]	380	Nanofiber	Electrospinning
ZnO [45]	9.2	Nanowire	Hydrothermal
ZnO [46]	26.7	Nanobelt	Vapor transport deposition
ZnO [47]	6.4	Thin film	Pulsed laser deposition

2.2. PVDF nanofiber synthesis process

PVDF nanofibers have shown good ability to harvest the mechanical force under high strain conditions, due to their excellent flexibility and process simplicity [18]. PVDF has been widely investigated due to its piezoelectric, ferroelectric properties as well as its high flexibility, high durability, and good mechanical properties. The molecular structure of PVDF involves the repeating monomer unit $(-CH_2CF_2-)_n$. PVDF is a semi-crystalline polymer with the four distinctive crystal structures which can be divided into the polar and non-polar phase. Among them, three polar crystal forms exist (β, γ and δ phases), where β-phase (TTTT) is highly polar compared to the other two phases. The non-polar α-phase (TGTG'), however, is the most common and thermodynamically stable phase at ambient temperature and pressure [48; 49]. Figure 2-2a and Figure 2-2b presents the α-phase and β-phase of PVDF, respectively. The β-phase of PVDF is responsible for its electroactive properties such as ferroelectric, piezoelectric and pyroelectric properties. The PVDF polymer chains in the unit cell of β-phase are arranged in a way that all the dipoles are aligned in a parallel manner leading to a net dipole moment, which is the strongest amongst all the phases [37]. Hence, the enhancement of β-phase of PVDF is essential for many applications.
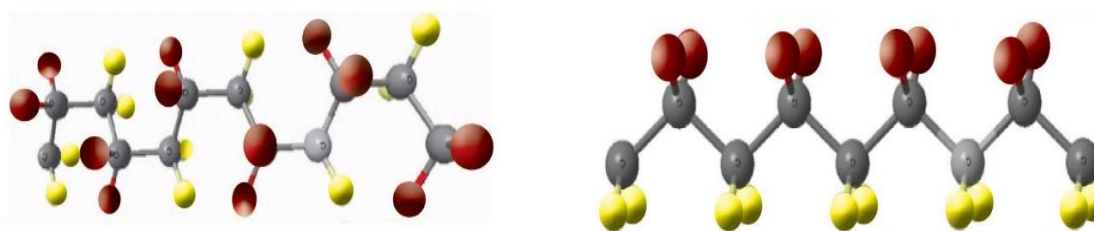
Figure 2-2- The structure of PVDF (left) α-phase (right) β-phase of PVDF.

In order to enhance the β-phase, different approaches have been utilized. These approaches can be classified into two main categories including additive material approach and post-treatment approach (electrical poling, mechanical drawing, etc.). The latter has been mostly used to improve piezoelectric performance due to the enhancement of the degree of crystallinity of PVDF. However, the process is costly and time-consuming which limits the scalable production of nanogenerators/actuator in an industrial fabrication process. Electrospinning is a widely used processing method to fabricate flexible PVDF nanofibers due since it is simple, efficient and cost-effective. It has been reported that electrospun PVDF nanofiber results in the formation of the piezoelectric β-phase [50-53]. The electrospinning process involves applying a high electrical field and elongation force on nanofiber jet, as such it eliminates the need for post-treatment processes including electric poling and mechanical stretching. The advantage of using electrospun nanofibers for energy harvesting is their high mechanical robustness and responsiveness to small mechanical disturbances [40].

The fabrication process and characterization of PVDF piezoelectric nanogenerators and sensors have been explored in many research programs. This chapter aims to review some of the PVDF piezoelectric energy harvester and sensors which have been used in a variety of applications. In order to easily control the deposition of the nanofiber, Chang *et al*. [18] developed a direct write technique by using Near-field electrospinning (NFES). A tungsten electrode is used to construct nanofibers with the size of 50~500 nm in line-width on silicon-based collectors (Figure 2-3). The electrical field was created by applying 600 V between electrode and collector while the electrode-to-collector distance is 500 μm to achieve controllable position deposition. Also, the PVDF nanofibers achieve both in-situ electrical poling and mechanical stretch to exhibit piezoelectric properties. It was found that under mechanical stretching, nanogenerators can show

repeatable electrical outputs with energy conversion efficiency an order of magnitude higher than those made of PVDF thin films [18]. In addition, a much smaller domain wall motion barrier in PVDF nanofibers was observed as compared to PVDF thin film [54], which results in large piezoelectric responses.

The size and alignment of the electrospun nanofiber were also reported in several works. A drum collector has been widely used to enhance the alignment of the electrospun nanofiber. The high speed of the drum rotates to allow the nanofiber to deposit along the direction of the rotation. It has to be noted that the drum's rotation speed needs to be adjusted to an optimum range [55]. It was reported that the low speed leads to non-uniform deposition of nanofiber while the high-speed rotation of drum will break up the nanofiber and cause fiber discontinuity [56; 57]. In some works, the drum collector has been used to control the fiber in which the higher speed of the drum results in a finer size of the fiber [58; 59]. However, some researchers confirmed that the drum's rotation speed has an insignificant little effect on the fiber diameter [57; 60].
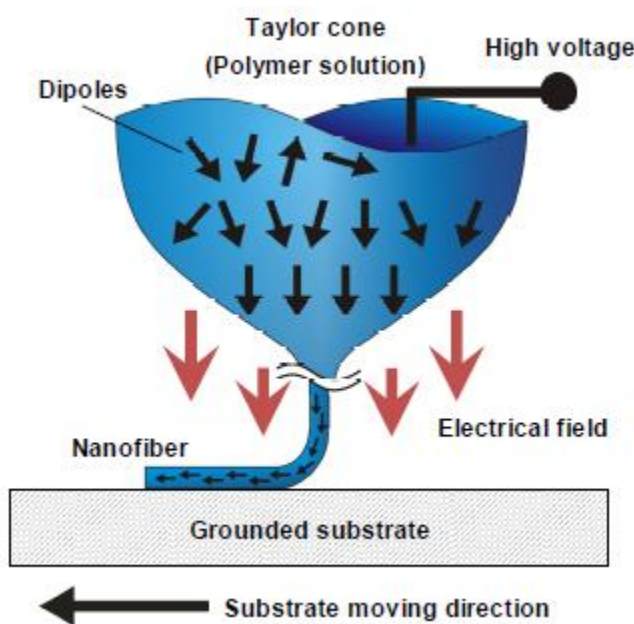
Figure 2-3-Schematic of the in-situ poling near-field electrospinning [18].

A hollow cylindrical near-field electrospinning (HCNFES) was developed to fabricate PVDF nanofiber [61]. In this method, the nanofiber was fabricated under high electrical field with a strong in-situ mechanical stretch. It was found that Young's modulus of the PVDF sample increased by 56.2 %. Figure 2-4 shows the aligned electrospun PVDF nanofibers using HCNFES process. The main drawback of near-field electrospinning process is that the nanofibers required a

post-treatment such as poling treatment and mechanical stretching to make the dipole of the polymer orient along the fiber length direction. It has been reported that far-field electrospinning is beneficial to make PVDF nanofiber with high piezoelectric properties in the absence of post-treatment process. It has been reported that electrospun PVDF nanofibers are fully poled right after fabrication using far filed electrospinning and show β-phase contents of 70%, therefore being able to be implemented into electroactive devices without further processing steps [52].
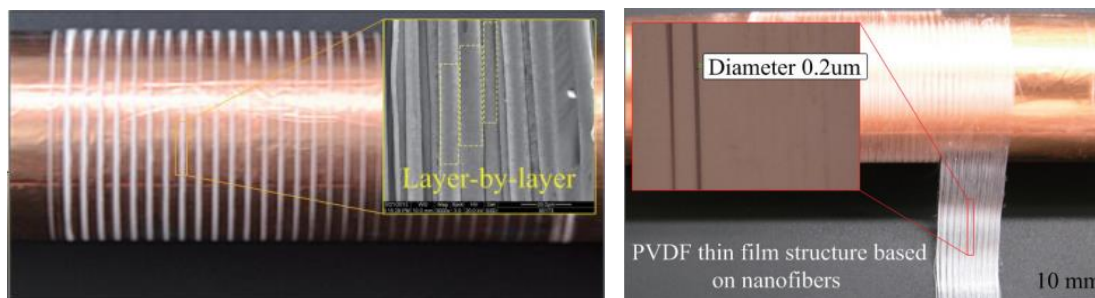
Figure 2-4-The aligned PVDF nanofibers with ultra-long length and large area form thin film structure using HCNFES process [61].

Researchers have been investigating the addition of additives such as inorganic salts (NaCl, KBr, KCl), organic salts (BTEAC,), and CNTs on fiber morphology for PVDF solutions [62]. Persano et al. introduced a large area, flexible piezoelectric material that consists of sheets of electrospun fibers of PVDF. Also, The process yields alignment at both the level of the fibers and the polymers, thereby enabling excellent response and high β-phase content without further processing [63]. Ahn et al. investigated an electrospun PVDF with multiwalled carbon nanotube (MWCNT) nanocomposites. The effects of MWCNT concentration and the post-treatment process including the mechanical drawing and poling on the piezoelectric properties of the PVDF were evaluated. It was found that the addition of 0.2 wt. % of MWCNTs promote the formation of higher β-phase in PVDF due to nuclei effect in the crystallization process and inducing charge accumulation at the interface [30]. Sharma et al. [42] studied the ferroelectric and piezoelectric of the electrospun PVDF nanofiber with two different nanoparticles: functionalized multiwall CNT and silver (Ag) decorated CNTs. This study was conducted in with electrospinning and melt-mix process. The results indicate that the formation of β-phase is highly dependent on the adopted process. It was found that the addition of both nanoparticles using electrospinning process results in a significant phase transformation of α-phase to β-phase. However, the highest piezoelectric

coefficient was obtained for the PVDF nanofiber with the silver decorated CNTs. Yee et al. [64] investigated the effect of single-walled carbon nanotubes (SWCNT) on the polymorphism behaviors of PVDF nanofiber. The nanofiber was collected under high extensional force and finally treated with supercritical carbon dioxide (SCCO$_2$). The results revealed that the existing hydroxyl groups in SWCNT could interact with PVDF molecular chain which can enhance the β-phase formation of PVDF nanofiber. Also, the SCCO$_2$ treatment effectively induced the β-phase formation due to the intense confinement effect of SWCNT for stabilizing the nuclei of the β-phase and the high pressure applied.

The piezoelectric properties of PVDF-CNT were examined by Wu et al. [65]. The results proved that addition of CNT could promote the β phase formation. The piezoelectric properties of the electrospun PVDF nanofiber were also improved through interfacial polarization. Bhavanasi et al. [66] reported the piezoelectric behavior of PVDF with GO addition. The bilayer PVDF-GO was fabricated. The post-treatment process was also applied to further improve the β phase formation. The PVDF-GO showed superior piezoelectric behavior compared to the neat PVDF sample, due to synergic effect of electrostatic force and the presence of charge at the interface of the PVDF and GO. Rahman *et al.* [67] developed a flexible energy harvester using PVDF–GO composite. The fabricated film was undergone the poling process. The PVDF-GO exhibited a significant piezoelectric and ferroelectric properties compared to those of pure PVDF.

Other than the carbon-based materials, several additives were also incorporated into PVDF polymer solution to further improve the properties of PVDF. The addition of LiCl was also found to be useful in enhancing the β-phase formation in PVDF crystal structure [68]. It was also found that the addition of LiCl can improve the piezoelectric behavior of nanofiber and the voltage output of the device [68]. Fashandi et al. [69] fabricated a PVDF-cellulose nanocrystal (PVDF/CNC) using electrospinning process. The results indicated that the addition of CNC could significantly promote the β phase formation due to the nucleation effect. Moreover, the presence of CNC particle can prevent the nucleation of α crystalline phases which finally enhanced the piezoelectric properties. Liu et al. [70] investigated the effect of nanoclay addition on β phase formation of PVDF. The results indicated that the α-phase is significantly reduced. The FTIR results proved the formation of long trans conformation. It was found that the nanoclay plate can stabilize the trans conformation as a result of the interaction between the PVDF chain and nanoclay layers. The latter can enhance the transformation of the nonpolar (α-phase) to polar phase (β phase). The effect of

ZnO nanoparticles addition was also studied by Bafqi et al. [71]. They found that the addition of ZnO into PVDF nanofiber can enhance the piezoelectric properties and the voltage output of the energy harvester device.

2.3. PVDF piezoelectric devices and applications

The main applications of PVDF piezoelectric materials can be categorized into three main groups including the energy harvesting, sensing and actuation applications. The flexibility of PVDF makes this material as an exceptional candidate for several applications, particularly for sensing applications. This section aims to review both the energy harvesting and sensing application of the PVDF piezoelectric device.

The energy harvesting efficiency of electrospun PVDF-TrFE doped with ceramic fillers was studied by Perreira et al. [72]. A controversial result was reported by Caroline et al. [73], in which the piezoelectricity generated voltage in response to mechanical deformation of $BaTiO_3$-PVDF composite nanofibers with various concentrations of $BaTiO_3$ nanoparticles was measured. It was found that the magnitude of the resultant voltage increases as the nanoparticles concentration increases. PVDF nanofiber with 16 wt.% $BaTiO_3$ nanoparticles exhibit piezoelectric output voltages that are 1.7 times greater than PVDF fiber without $BaTiO_3$ nanoparticles when subjected to the same degree of deformation. Zeng et al. [74] presented a wearable electric power nanogenerator, which consists of a PVDF–NaNbO3 nanofiber nonwoven fabric as an active piezoelectric component, and an elastic conducting knitted fabric, made from segmented polyurethane and silver coated polyamide multifilament yarns, as the top and bottom electrodes. The resultant generator exhibits high durability (greater than 1 000 000 cycles) and good electric power generating performance in a cyclic compression test simulating human walking conditions. Ji sun Yuh [75] investigated the piezoelectric nanofiber composites of electrospun PVDF polymer and PZT ($Pb(Zr0.53Ti0.47)O_3$) ceramics. The results demonstrated that a PZT content of 20 wt% could enhance the tensile and piezoelectric characteristics. An increased Pr (remnant polarization) of 60 % was observed from pure PVDF nanofiber of 0.15 μ C/cm2 to PZT/PVDF nanofiber (PZT 20 wt%) of 0.24 μ C/cm2. The carbon-based materials such carbon nanotubes (CNT) and MWCNTs are the most common types of additives to enhance the β-phase content as well as piezoelectric properties of PVDF. Ou et al. [76] used NFES method to fabricate PVDF nanofibers mixed with additional MWCNT. The results indicated that the addition of MWCNT could increase the crystalline of β which enhance the piezoelectric properties. Prakriti et al. [77] studied the effect

of PVDF-graphene-Eu^{3+} composite. It was found that the complete conversion of the piezoelectric β-phase and the improvement of the degree of crystallinity is governed by the incorporation of Eu^{3+} and graphene sheets into P(VDF-HFP) nanofibers. One of the main challenges in the piezoelectric device is to facilitate the transfer of accumulated static charges into the capacitor since PVDF is not conductive. Hao Yu showed that the addition of an appropriate amount of MWCNTs might result in a higher surface conductivity of PVDF which finally leads to higher power output [24]. However, the dispersion of MWCNTs was a deterrent factor for adding high dosage to PVDF. It was found that uniform distribution of MWCNT in the electrospun films helps efficient charge accumulation at the interface between the MWCNTs and the matrix PVDF molecules [78]. The effect of MWCNTs on mechanical properties of PVDF mats was investigated by Shu-Hua Wang et al. [79]. It was reported that with the increasing of MWCNT content, the β-phase was noticeably enhanced, and the fibers became more elastic, which was manifested by Young's modulus decreased drastically. Other than additives, the effect of substrate on piezoelectricity response of the flexible devices has been investigated by Sun-Lee [27]. The effects of different substrates such as slide glass, poly (ethylene terephthalate), poly (ethylene naphthalate), and paper and on the efficiency of the PVDF nanofiber energy harvesters was studied. It was found that the thinnest paper substrate (66 μm) with a moderate Young′s modulus showed the highest voltage output (0.4885 V) for the energy harvester with the dimension of 25mm x 31mm. Siddiqui et al. [80] developed a PVDF–TrFE piezoelectric nanogenerator for biomechanical energy harvesting application. The barium titanate nanoparticles were also embedded into PVDF polymer for charge storage. The flexible device was also proven to capture biomechanical energy from body movements and store the generated electrical energy in a rechargeable battery.

In addition to energy harvesting applications, PVDF has shown promising potential in sensing applications such as pressure sensor, an acoustic sensor, and ultrasound sensor [81]. Wang et al. [82] reported a force sensor based on PVDF fabrics with excellent flexibility and breathability, to be used as a specific human-related sensor. The results demonstrated the feasibility of using PVDF nanofiber to make a flexible pressure sensor without mechanical and poling treatment. Xin [83] investigated the straight PVDF/nano clay nanofibers fabricated by a "near distance-wheeling" electrospinning (NWS) method. The electrospun fibers were embedded into full-fiber sensors. The sensor based on the PVDF/nanoclay fibers exhibited considerable

piezoelectric properties with good reproducibility. Xumin Pan et al. [84] developed a flexible piezoelectric self-powered vibration sensor was fabricated by transferring the PVDF NFs from silicon to PDMS substrate. Accordingly, the sensor can be used for self-powered monitoring of the vibration state of a metal foil and measure the intrinsic resonance frequency of the objects without any powering source. Samiran Garain et al. [85] fabricated a low-cost in situ poled method to construct a scalable and flexible force sensor. The electrospun Ce^{3+} doped PVDF/ graphene composite nanofibers were used in this study. The higher sensing properties along with the flexibility enabled real-time monitoring of sound waves. James S. Lee [86] developed a PVDF-ZnO sensor which was able to measure pressure and temperature in real time simultaneously. The pressure was monitored by the change in the electrical resistance via the piezoresistance of the material, and the temperature was inferred based on the recovery time of the signal. Rathod [87] investigated using a large-area PVDF thin films for strain sensing applications. The results indicated that the scalable PVDF sensors could be better with the power output comparable to the PZT sensors. In addition, the PVDF sensors detect both A_0 and S_0 modes of Lamb wave successfully. Surface acoustic devices are considered as a useful and efficient sensor for health monitoring purposes [88]. Dodds et al. [89] investigated the performance of interdigitated transducers (IDTs) for active health monitoring. The feasibility of using these devices for sensing and actuation of Lamb waves on an aluminum pipe was validated. The results showed that the devices are able to detect the damages by using a pitch-catch setup onto an aluminum pipe and plate. Lang et al. [90] developed a sensitive acoustics sensor using electrospun piezoelectric nanofiber. The device was proven to detect the mechanical sound wave at low-frequency range.

2.4.   Summary

In spite of aforementioned researchers on fabricating electrospun PVDF nanofiber, the processing parameters of electrospun process on formation of β-phase is still not understood. Several research indicated that electrospun PVDF fibers could be used to fabricate a piezoelectric device without any extra poling treatment, while controversial results were reported by other authors indicating that the electrospun PVDF nanofibers required a post-poling treatment. This might be due to this fact that the electrospinning fabrication process involves several parameters which not only affect the morphology of the fibers but also might change the crystallinity of PVDF nanofibers. Hence, the controlled size of the fiber and β-phase formation requires a good understanding of the fabrication process parameters. Moreover, no robust model has been

presented to predict the performance of nanofiber in terms of morphological as well as crystallinity properties. Establishing a robust numerical model is therefore beneficial to predict the performance of PVDF nanofiber.

Several approaches have been utilized to enhance the β-phase of PVDF nanofiber. The poling and mechanical stretching were found to be the most efficient methods to improve the β-phase content. However, these methods limit the feasibility of large-scale production and also are expensive. Therefore, a hybrid structure needs to be designed to not only improve the β-phase but also helps to facilitate the transferring of the static charges. So far, most of the applications of PVDF piezoelectric devices are limited to the pressure sensor and only a few applications for health monitoring have been reported. The advantage of using PVDF as a sensor for health monitoring might be beneficial as the voltage constant of PVDF material is sufficiently high to be used as a sensor. Hence the feasibility of using piezoelectric sensors in civil engineering infrastructure applications need to be explored.

CHAPTER 3. FABRICATION PROCESS OF ELECTROSPUN PVDF NANOFIBER

Electrospinning is a simple, versatile and low-cost technique for fabricating flexible nanofibers with significant lengths, uniform diameters in nanoscale and various compositions [3]. Moreover, this method is an effective method for large-scale production of the nanofiber. Electrospinning method was used in this study to fabricate the PVDF nanofiber. Electrospinning process is a synthesis method that uses electric force to draw charged polymers into nanofiber with diameters ranging from few nanometers to several hundred nanometers. Electrospinning process is applicable for many applications, and a wide range of nanofibers made of natural polymers, polymer blends, ceramic precursors and metal or metal oxides have been electrospun into different fiber morphologies.

3.1. Electrospinning process

A typical electrospinning system consists of a collector (stationary or rotor drum), syringe, electrical pump and a high voltage power supply. During the electrospinning, a high electrical field is applied between the conductive needle and a conductive drum to draw the nanofibers. A schematic of an electrospinning set up is shown in Figure 3-1.
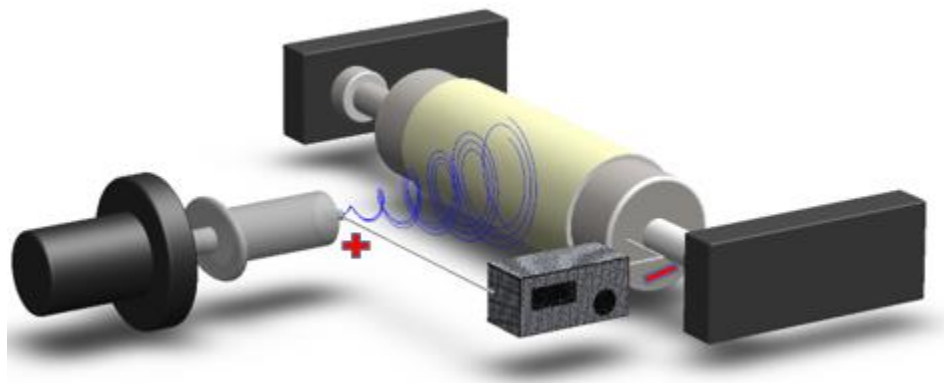
Figure 3-1- Electrospinning process using a rotor drum as a collector.

The basic principle of electrospinning involves forming a conical fluid structure called the Taylor cone at the tip of a metallic spinneret by applying a high voltage between the spinneret and a grounded collector [91]. The voltage induces a repulsive force which works against the surface tension of the solution. Once the repulsive force overcomes the surface tension at a certain voltage [91; 92], the nanofiber jet spun from the needle. The amount of applied voltage plays an important

role in electrospinning process. If the applied field is not sufficiently high, the nanofiber jet will break up into droplets, which is called "electrospraying." The nanofiber jet experiences different types of instability during its travel towards the collector which leads to the fiber jet being collected on the conductive drum [93]. The solvent evaporates while the nanofiber jet travels towards the conductive electrode. The rate of evaporation depends on several factors such as temperature, humidity, the distance between collector-spinneret, flow rate and type of solution. The nanofiber jet, however, can resist and prevents the jet from breaking up resulting in the formation of fibers. The viscosity of the solution is also a critical parameter. In fact, the low viscosity can change the electrospinning process into electrospraying process by formation of droplets instead of nanofibers. Therefore, it is critical to understand the effect of different processing parameters on the structural properties and functionality of nanofibers. In this study, a commercial electrospinning machine (Tongli Tech TL-01) was used to make the PVDF nanofiber. Figure 3-2 shows the setup of the device along with the electrical pump.

The sol-gel process was used to fabricate the PVDF nanofiber. PVDF pellet (Mw=275000), N,N-dimethylformamide (DMF, Sigma 99.5%) and acetone (Sigma, 99.7%) were purchased from Sigma-Aldrich. The PVDF solution was prepared by dissolving PVDF pellets in solvent mixtures of DMF/Acetone. The solution was heated at 70 °C for 1-hour following by 5 hours stirring at room temperature. The homogenous PVDF solution was then added to the 10-ml plastic syringe which was placed in a syringe pump. The syringe was then connected to a special plastic pipe to transfer the solution to the needle. A stainless-steel needle with the inner diameter of 0.6 mm was used for the spinning process.

The syringe, plastic pipe and the needle set up are shown in Figure 3-3. The positive voltage was applied to the needle to form Tylor cone. The various feeding rate of the solution was adjusted to obtain a stable liquid jet. The nanofibers were spawned on a grounded rotating drum collector, which was placed at a distance of 10 cm from the tip of the needle. The drum speed was kept constant at 1000 rpm. Figure 3-4 shows the spinning process using a drum collector.

The spinneret was moving in a horizontal direction at the constant speed to facilitate the large-scale production. The PVDF nanofiber mesh was finally collected from the drum. Figure 3-5 shows the process of peeling off a large scale electrospun PVDF nanofiber mat from the drum collector.
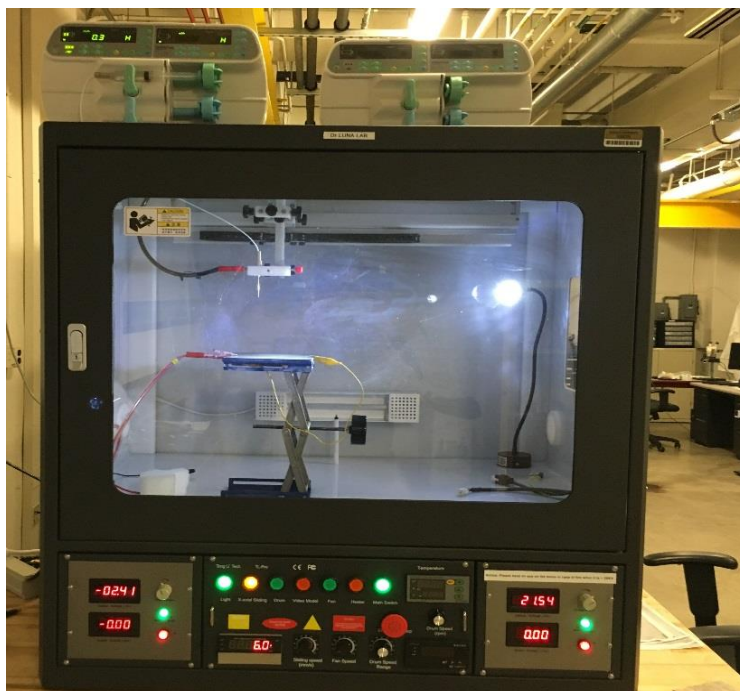
Figure 3-2- The electrospinning setup along with the electrical pump.
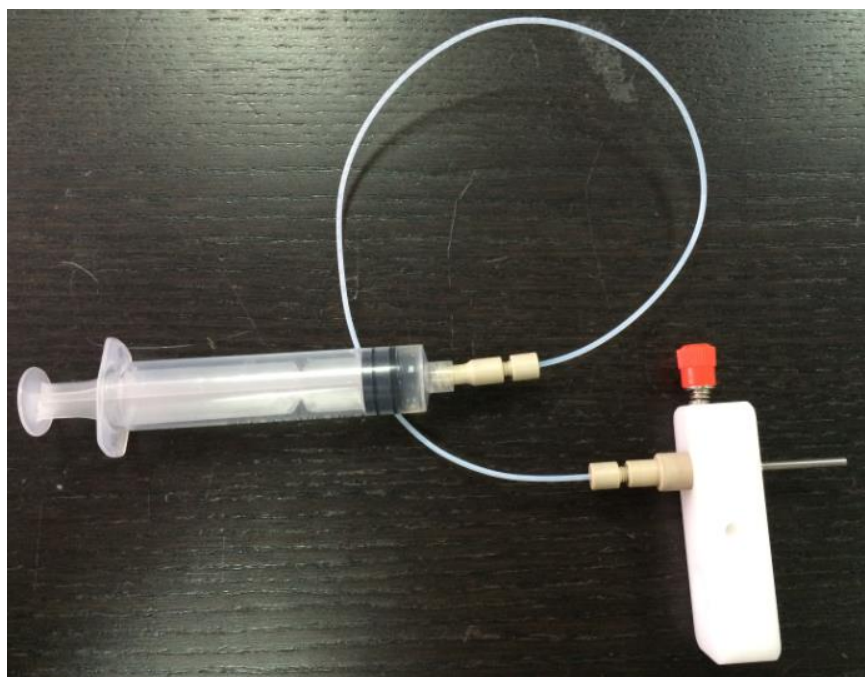
Figure 3-3- The syringe, plastic pipe set up for the electrospinning process
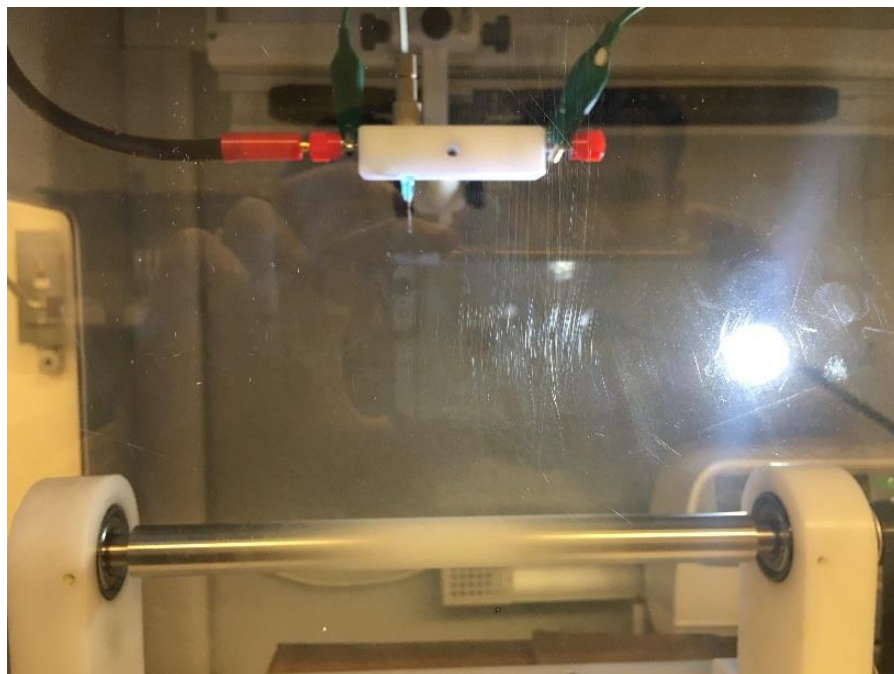
Figure 3-4- The electrospinning process using a drum collector
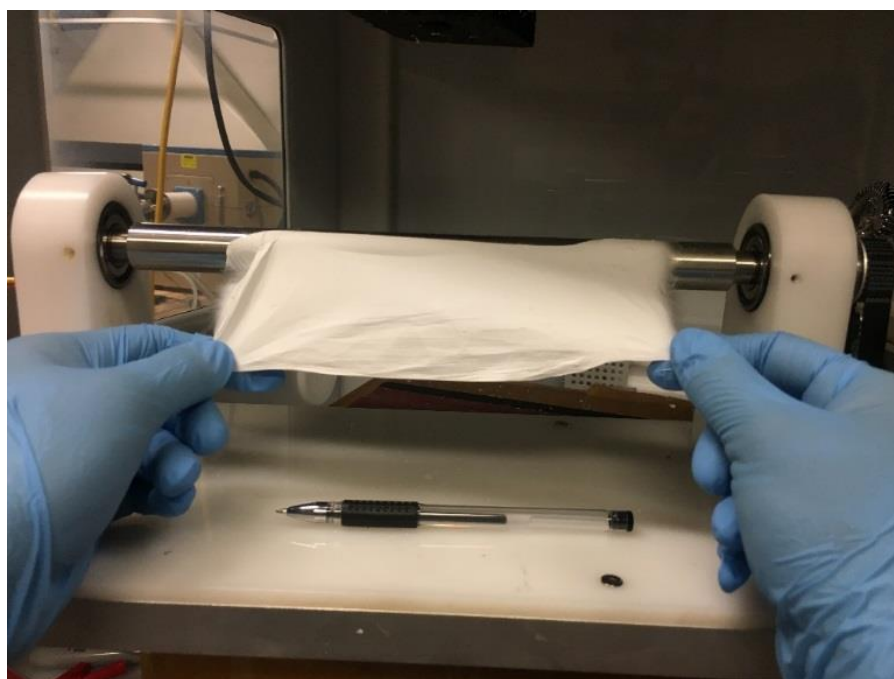
Figure 3-5- Peeling off a PVDF nanofiber from the drum collector.

3.2. Model fitting and validation

Although the electrospinning process appears to be technically straightforward, several processing variables need to be well understood and optimized in order to fabricate nanofibers

with the desired properties such as uniformity, alignment, β-phase and beads-less formation. Up to now, the conventional method to fabricate the electrospun PVDF nanofiber has been used, in which the interdependence of each processing parameter on nanofiber characteristics are overlooked since this method only involves changing one of the electrospinning process parameters while keeping the others fixed at certain values. As results, the conventional methods do not provide a reliable model to predict and optimize the properties of PVDF nanofiber. Therefore, it is important to develop a comprehensive and reliable model to elucidate the effect of the electrospinning processing parameters on the morphology and the β-phase formation of electrospun PVDF nanofiber [94].

In this study, four independent processing variables, namely PVDF concentration, DMF/acetone ratio, flow rate and electrical field, were studied. The defined variables for this experiment and their control levels are shown in Table 3-1. Three responses were considered in this study, including nanofiber size, beads formation and a fraction of the β-phase content. It is important to note that the addition of acetone above 83 vol. % caused clogging at the needle tip resulting in stopping of the electrospinning process. Therefore, the lowest DMF/acetone ratio was limited to 0.2.

A total of 33 set point combinations was randomly chosen according to D-optimal configuration for all four parameters. A second-order polynomial model was then calculated for each response.

Table 3-1- Variables and corresponding limits for fabrication of PVDF nanofiber.

Symbols	Range of variation	
Variables	Min	Max
Concentration (%)	15	30
DMF/acetone (v/v)	0.2	3
Flow rate (ml/h)	0.5	3.8
Electrical field (kV/cm)	0.75	1.36

The model was developed in three consecutive steps. First, a full polynomial model is applied to establish the relationship between the electrospinning process and the responses.

Second, the insignificant terms were removed from the model by conducting an analysis of variance (ANOVA). The accuracy of the model was evaluated at the last step by performing residual analysis [32; 95; 96]. The adequacy of each proposed model was validated by coefficients of multiple determination (R^2), which implies the total deviation of the response variable from the predictive model [32; 34; 97-106]. The analyze of results for full regression models included the adjusted coefficient of multiple determinations (Adj-R^2), and the predicted coefficient of multiple determinations (Pre-R^2), the lack-of-fit, and the model P-value, are given in Table 3-2. The obtained correlation coefficients for fiber size, beads formation and a fraction of β-phase were R^2= 0.95, R^2= 0.92 and R^2= 0.94 respectively. The adequacy of the model was verified by performing a lack-of-fit test (Table 3-2). The desired result is an insignificant lack-of-fit, which is presented by a value greater than 0.05 [107-111]. All the P-values obtained by ANOVA implied that the lack-of-fit is not significant compared to the reference.

The significance of all the four parameters were assessed using ANOVA analysis. All the insignificant terms were removed from the model through the screening process. These high values of correlation coefficient validate the adequacy of the model used to navigate the design space. ANOVA analysis was also performed to further evaluate the significance of the model. The F-values of 21.1, 16.8 and 88.7 were obtained for fiber size, beads formation and a fraction of β-phase respectively, which indicated that the models are significant.

Table 3-2- Results for full regression models.

Responses	Adj-R^2	Pre-R^2	F-value	Lack of fit	Model P-value
Fiber size	0.95	0.89	21.1	0.32	<0.0001
Beads formation	0.92	0.85	16.8	0.46	<0.0001
B-phase content	0.94	0.90	88.7	0.23	<0.0001

3.3. Morphology of PVDF nanofiber

Parameters affecting the morphology and crystallinity of PVDF nanofiber can be classified into two categories namely solution properties and electrospinning process parameters. The PVDF nanofiber size and formation of the beads are the two main characteristics the need to be controlled during the electrospinning process. SEM was used for visual analysis of the PVDF nanofiber morphology. The diameter and size distribution of the fibers were analyzed using ImageJ software.

Figure 3-6 and Figure 3-7 shows the morphology of two electrospun PVDF nanofiber mesh with the same concentration (25%) and different DMF/acetone ratio. The average diameter of nanofiber in sample 1 and sample 2 was around 87 nm and 438 nm, respectively. The SEM images of other two samples with the same PVDF concentration (27.5%) are presented in Figure 3-8. Figure 3-8a shows a beadless PVDF nanofiber while Figure 3-8b exhibits a high number of beads at the same concentration. The concentration of PVDF was reported widely as the most significant factor in determining the percentage of beads in PVDF nanofiber [51; 112], however the substantial difference in nanofiber size and beads formation for the samples with the same concentration of PVDF pellets, implies other electrospinning processes have more effects on morphology of electrospun nanofiber. In order to better present the complicated relations between the parameters and responses, several 3D interaction surface graphs along with the trace plots were obtained from RSM model. Once the model was validated, the effect of each parameter on the response was systematically investigated. The ANOVA analysis was used to assess the effect of individual parameters as well as the interaction of variables on responses. The effect of variation of concentration and DMF/acetone ratio on nanofiber size is shown in Figure 3-9. The higher concentration resulted in higher solution viscosity and stronger intermolecular interactions which led to larger nanofiber size. However, the amount of acetone plays a critical role in controlling the fiber size. For a constant electrical field and flow rate, the higher DMF/acetone ratio led to finer fiber size, as higher acetone content increases the evaporation rate. In order to have a better understanding of each individual constituents' effect on the response, a trace plot was used. A constituent effect curve displays how a model predicts that the response will change as the constituent is decreased or increased from its level in the reference mixture [34]. Figure 3-10 shows the effect of variation of all constituents on PVDF nanofiber size. The slope of the plot indicates the sensitivity of the response in terms of each constituent. The results indicated that the higher electrical field leads to the formation of the fine fibers. In fact, applying the higher voltage might impose a higher charge density on the surface of nanofiber jet. This induces a larger elongation force to the fiber jet which results in a finer nanofiber size. As it can be seen, flow rate curve showed almost a horizontal trend, which implies that the nanofiber size is not very sensitive to this parameter. The formation of beads has been widely reported in the electrospinning process [113-115], and it has been considered as the main drawback of the electrospun fibers [113]. The formation of bead-free nanofibers is favorable in almost all applications of electrospun nanofibers.

The formation of beads in electrospun nanofibers is mostly related to the instability of the jet of polymer solution [116; 117]. In this study, the amounts of beads in the microstructure of the nanofiber were measured quantitatively using ImageJ software. Figure 3-11 shows the variation of the beads formation in PVDF nanofiber as functions of concentration and DMF/acetone ratio. The results indicated that the amounts of beads increase with the decrease of concentration. In general, the lower concentration increased the risk of beads formation in PVDF nanofiber. The low viscous solution favors the formation of beads in PVDF nanofiber due to lack of sufficient polymer entanglement [118]. The results indicated the number of beads was reduced drastically for the solution with the concentration above 25 %. However, several electrospun nanofiber samples with high concentration of PVDF pellets (more than 25%) exhibited a considerable amount of beads, implying that the solution concentration itself doesn't necessarily result in a beads-free nanofiber. The DMF/acetone was to be found very effective in decreasing the number of beads in PVDF nanofiber. However, the increase in DMF/acetone ratio results in nanofiber with increased beads may be attributed to the incomplete solvent evaporation. Indeed, the high volatility of acetone increased the evaporation rate of the solution which causes the jet to dry faster and thus impeding the electrospun jet breaking up into droplets [112]. Also, the addition of acetone reduces the surface tension of the solution so that beaded fibers can be converted into smooth fibers [119]. Hence, when the acetone concentration in the solution increased up to 60%, the number of beads reduced drastically, allowing to achieve a bead-free nanofiber at concentration even lower than 25%.
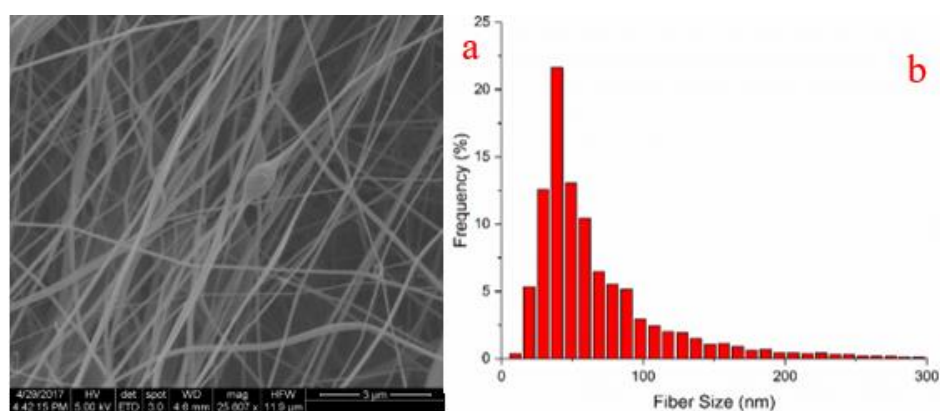
Figure 3-6- PVDF nanofibers at concentration of 25%, DMF/acetone: 3; a) SEM image b) Fiber size distribution.
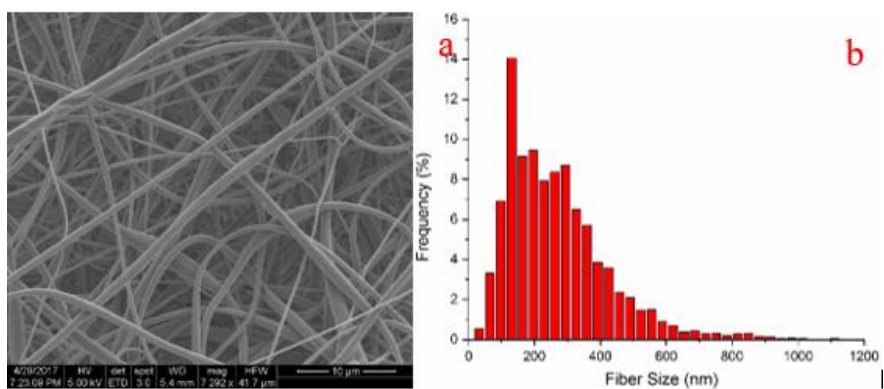
Figure 3-7- PVDF nanofibers at concentration of 25%, DMF/acetone: 1; a) SEM image b) Fiber size distribution.
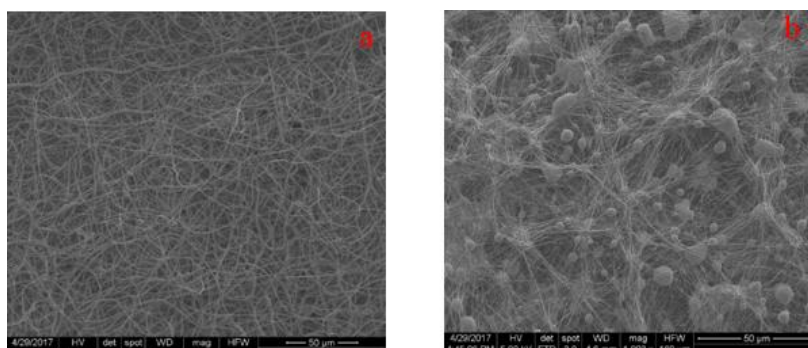
Figure 3-8- SEM images show two different surface morphologies in terms of beads formation for the samples with the same concentration of 27.5%: a) a beadless nanofiber b) PVDF nanofiber with a high number of beads.
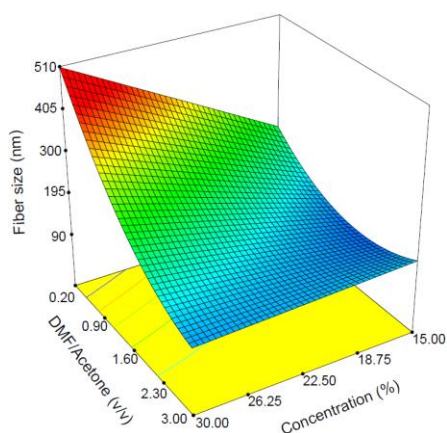
Figure 3-9-3D fiber size plot as a function of concentration and DMF/acetone. The higher concentration resulted in higher solution viscosity and stronger intermolecular interactions which led to larger nanofiber size.
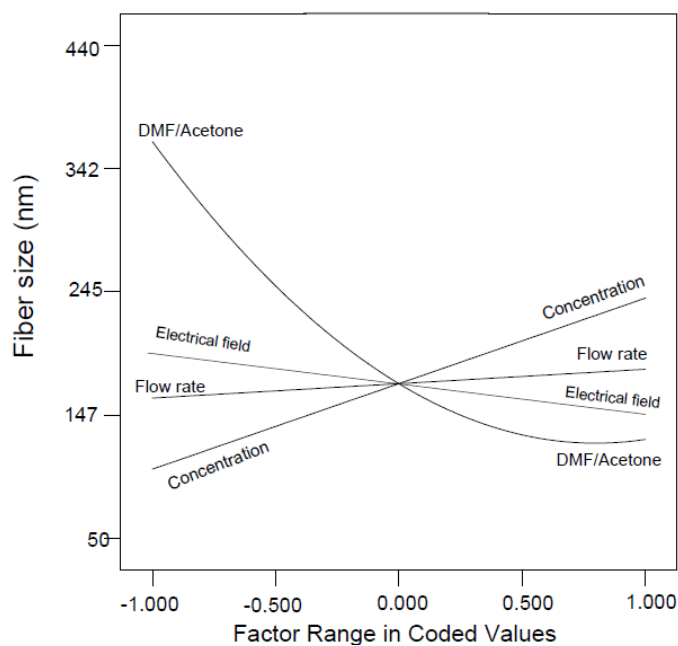
Figure 3-10-Trace plot of PVDF nanofiber size.
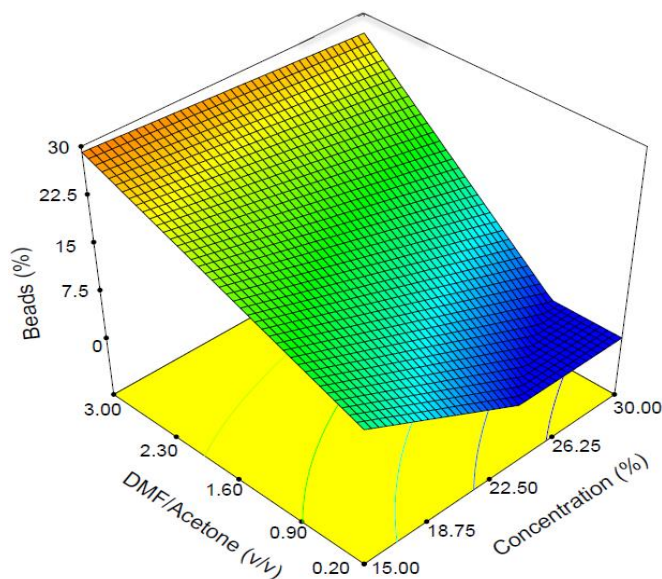
Figure 3-11-3D beads formation plot as a function of concentration and DMF/acetone. The amounts of beads increase with the decrease of concentration.

3.4. β-phase formation

Previous literature indicated that the ferroelectric and piezoelectric properties of PVDF nanofiber are attributed to the fraction of β-phase. FTIR analysis is mostly used to quantify the

electroactive phase content of PVDF. Assuming that FTIR absorption follows the Lambert-Beer law, the relative fraction of the β-phase in a sample containing just α and β PVDF is (Eq.1)[120]:

$$F_\beta = \frac{A_\beta}{(K_\beta/K_\alpha)A_\alpha + A_\beta} \quad (1)$$

where F(β), represents the phase content; A_α and A_β are the absorbance at 766 and 840 cm^{-1}; K_α and K_β are the absorption coefficients at the respective wavenumber, which values are 6.1 $\times$ 104 and 7.7 $\times$ 104 cm^2 mol^{-1}, respectively.

The fraction of β-phase as a function of concentration and DMF/acetone ratio is presented in Figure 3-12. The results indicated that the fraction of β-phase is considerably decreased by reducing the DMF/acetone ratio. It has been reported that low evaporation rates result mainly in the α phase which is thermodynamically more favorable, while intermediate rates in a mixture of α and β and high evaporation rates in the α phase, kinetically more favorable [121]. In fact, adding more acetone increases the evaporation rate of the solution, since it has a lower evaporation temperature, and this leads to the formation of more α phase in PVDF nanofiber samples. The trace plot (Figure 3-13) clearly confirms the significant effect of the acetone content of fraction of the β-phase content. As can be seen, the fraction of β-phase increased by increasing the concentration of PVDF pellets. High concentration of PVDF decreases the evaporation rate of the solution resulting in a formation of a high fraction β-phase content. The simultaneous interaction effect of low concentration (15 %) and high volume of acetone content (83 %) reduce the β-phase content below 50 %. Figure 3-13 shows that the fraction of β-phase can be enhanced by applying higher electrical field. The fraction of β-phase increases with increasing electrical field for all PVDF nanofiber samples. It should be noted that this effect was more pronounced for the samples subjected to higher voltage. At high voltage, the electrospun jet is subjected to the elongation force because of an increased number of charges. In addition, a high electric field is induced between the needle and conductive drum collector at high voltage. This electrical field acts as the polling process which can further enhance the fraction of β-phase in PVDF nanofiber samples [122]. As presented in trace plot, flow rate does not show any significant effect on the β-phase fraction.

3.5.   Numerical optimization

A numerical optimization was conducted to develop a bead-free PVDF nanofiber with the maximum fraction of the β-phase. The global desirability function [123], was used to optimize any combination of one or more goals (Eq.2):

$$D = (d_1^{r_1} \times d_2^{r_2} \times d_3^{r_3} \times ... \times d_n^{r_n})^{1/\sum r_i} = \left[\prod_{i=1}^{n} di^{r_i} \right]^{1/\sum r_i} \qquad (2)$$

where: n is the number of responses included in the optimization, and r_i is the relative importance of each individual functions d_i. Importance (r_i) varies from 1 to 5, respectively from least to most important. Individual desirability functions (d_i) range between 0, for a completely undesired response, and 1, for a fully desired response. For a value of D close to 1, the combination of different criteria is globally optimal, so the response values are near to the target values [34; 35].

In this study, two criteria have been defined to achieve a bead-free PVDF nanofiber with the highest fraction of β-phase. Table 3-3 shows all parameters and responses with their limits range, required for conducting numerical optimization. Figure 3-14 presents a two-response optimization zone, in which the highest β-phase fraction and lowest number of beads were found to reach the highest desirability function.

Two different optimal solutions, with the desirability of the functions ranging from 0.94 to 0.96, were obtained from the multi-objective optimization process. The predicted optimal solution and electrospinning parameters (M_1, M_2) and corresponding response values are shown in Table 3-4.

The morphology of both optimal solutions is presented in Figure 3-15. The SEM picture shows the formation of beadless electrospun PVDF nanofiber for both optimal samples. The fraction of β-phase was determined by FTIR technique as shown in Figure 3-16. The nanofiber sizes of M_1 and M_2 are 265 and 295 nm respectively which are aligned with the defined range for the optimization process. The samples exhibited 75 % and 71 % of the fraction of β-phase content, respectively which satisfy the minimum criteria in the optimization process. Results confirmed that the experimental values are in good agreement with the values predicted by the proposed model.
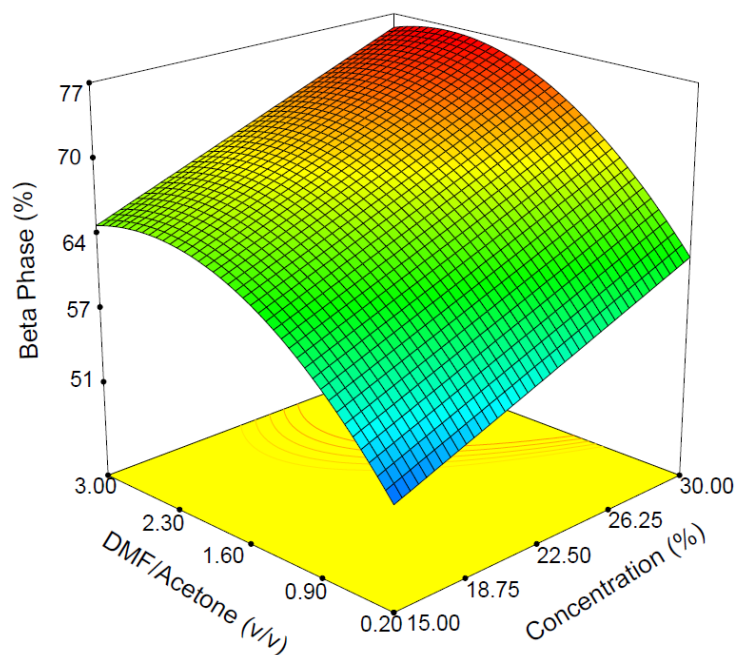
Figure 3-12-3D fraction of β-phase plot as a function of concentration and DMF/acetone. The fraction of β-phase is considerably decreased by reducing the DMF/acetone ratio.
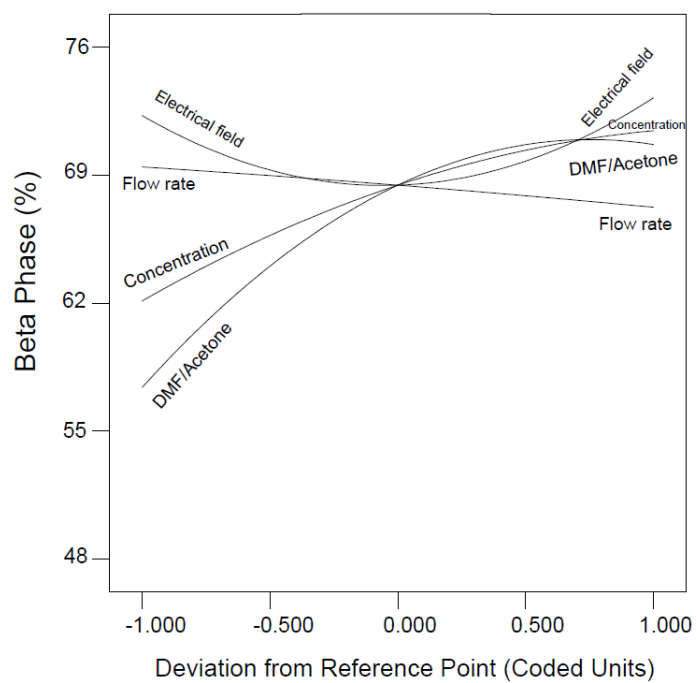
Figure 3-13- Trace plot for a fraction of β-phase in PVDF nanofiber.

Table 3-3- Optimization of individual responses for a bead-free PVDF nanofiber with the highest fraction of β-phase.

Responses and Variables	Lower	Upper	Criteria	
			Goal	Importance
Concentration(%)	15	30	In range	5
DMF/acetone (v/v)	0.2	3	In range	5
Flow rate (ml/h)	0.5	3.8	In range	5
Electrical field (kV/cm)	0.75	1.36	In range	5
Fiber size (nm)	58	300	In range	5
Beads (%)	0.1	2	Minimize	5
B-phase (%)	0.48	0.76	Maximize	5

Table 3-4- Optimum parameters for the proposed criteria.

Constituents and responses	M1	M2
Concentration (%)	27.5	26
DMF/acetone (v/v)	1.49	1.25
Flow rate (ml/h)	2	1.5
Electrical field (kV/cm)	1.36	1.36
Fiber size (nm)	265	295
Beads (%)	0.09	0.09
β-phase (%)	75	71
Desirability	0.98	0.96
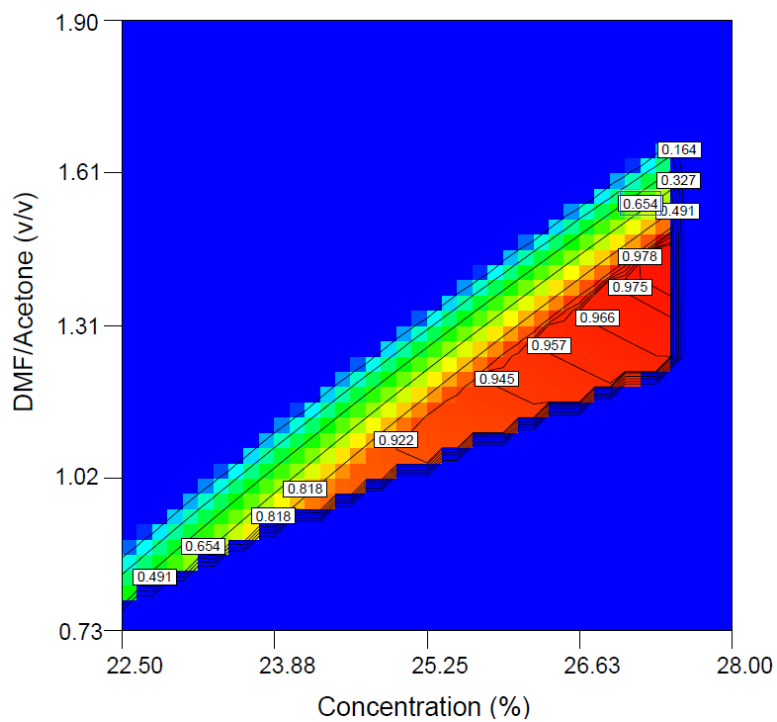
Figure 3-14- Response surface plots of the Derringer's desirability function in correlation with a variation of concertation and DMF/acetone ratio. The red zone represents the optimized solution obtained by RSM model.
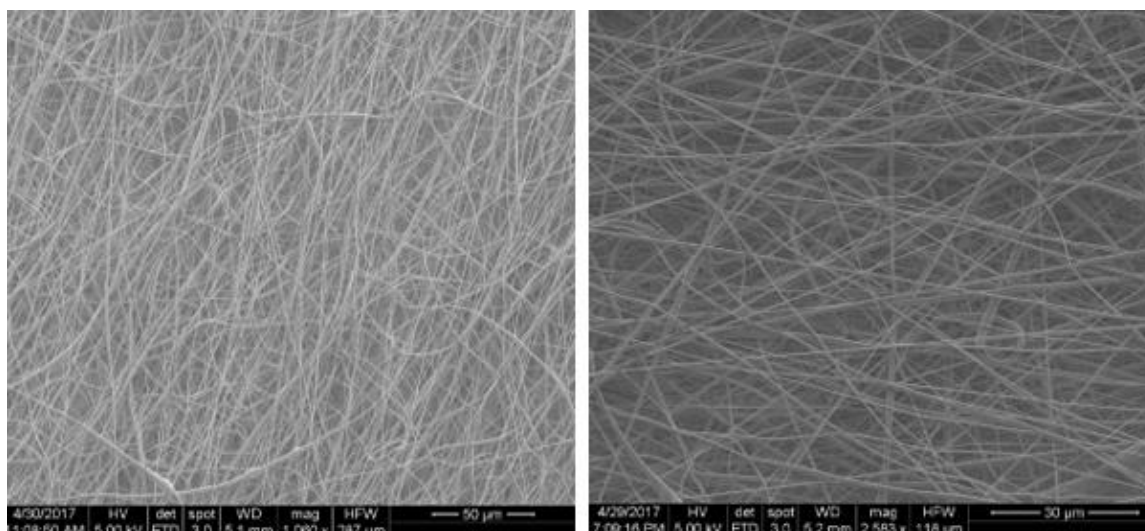
Figure 3-15- The SEM images of PVDF nanofiber samples optimized by the multi-objective optimization process.
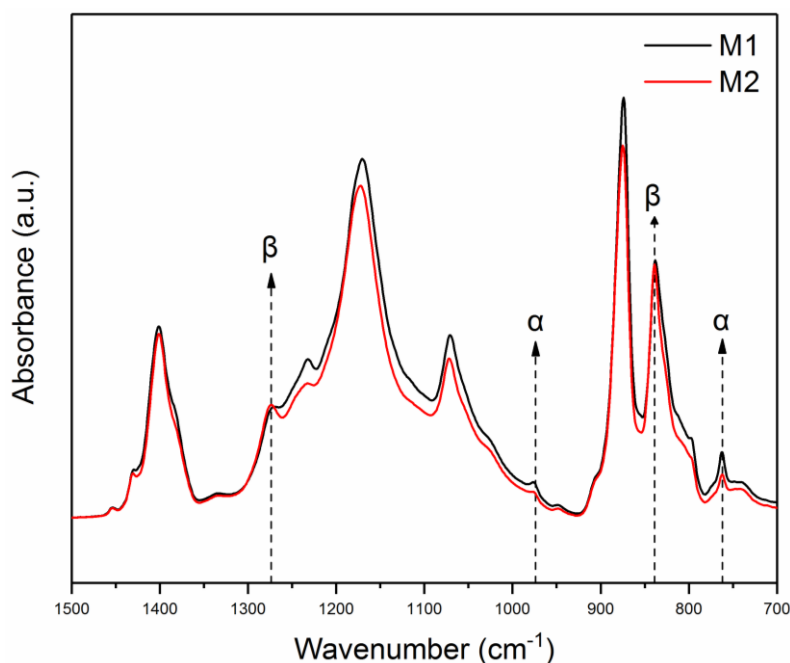
Figure 3-16- The FTIR curve of PVDF nanofiber samples optimized by the multi-objective optimization process. The absorbance peak at 766 and 840 cm^{-1} are the main peaks which represent the α and β phase of PVDF, respectively.

3.6.   Enhancement of β-phase content using core-shell system

To further enhance the piezoelectric properties of PVDF nanofiber, a core-shell structure was developed to improve the β-phase fraction as well as transferring the static charges. Figure 3-17 shows the schematic set-up for core-shell electrospun PVDF nanofiber.

The graphene oxide (GO) was selected as an interior core which is considered as an ideal nanofiller for improving the mechanical properties of PVDF. GO acts as the nucleation agent to promote the formation of β-phase in PVDF. GO can also enhance the dielectric permittivity and ferroelectric properties of neat PVDF [124].

Moreover, adding nanofiller is considered an inexpensive approach compared to the post-treatment approach as it doesn't require of sophisticated devices and complicated process. The core consists of electrospun PVDF-GO, and the shell consists the neat electrospun PVDF nanofiber. The GO was synthesized using the modified Hummers method [125]. First, a solution of 54 mL of H_2SO_4 and 6mL of H_3PO_4 (9:1 ratio) was prepared. Afterwards, 0.5 g of pristine graphene was added to the solution while stirring. The stirring continued approximately 8 hours until a dark green solution was achieved.
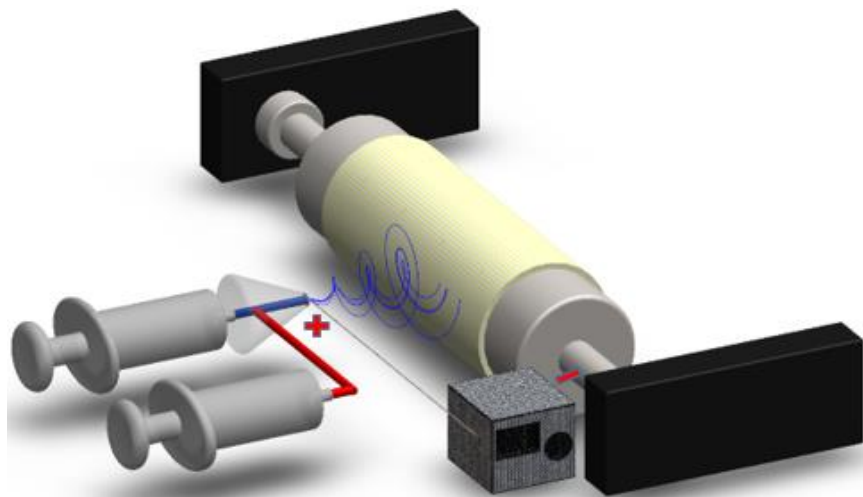
Figure 3-17- A core-shell electrospinning set up.

Then, 1.5 mL of H_2O_2 was added slowly using a syringe pump. 20 mL of HCl and 60 mL of deionized water was then added to the reaction. The flask was swirled, and a Falcon/Eppendorf tubes were used to centrifuge for 10 minutes. In this step, the supernatant for disposal was taken out and washed with additional HCl and deionized water. The material was suspended and centrifuged again. This step was repeated 7 times. Lastly, after the final supernatant was disposed of, the GO was dried in the oven at 90 °C for 2 days. The solution of PVDF and PVDF-GO was prepared using the same procedure explained in section 3.1. The ultrasonication probe technique was used to produce the stable dispersions of the GO particle in PVDF solution. Figure 3-18 shows the PVDF and PVDF-GO solution using the sol-gel process.

Figure 3-18- the PVDF solution (left) and PVDF-GO solution(right)

Figure 3-19 shows a schematic of the core-shell structure of electrospun GO-PVDF nanofiber composite. By the fabrication processes described in section 3.2-3.6, one can identify the optimized PVDF nanofiber with highest piezoelectric properties. Sample M_1 (Table 3-4) was

selected as a reference for this part of an experimental study to compare with GO-PVDF nanofiber composite. Afterward, the GO doping of the PVDF is performed to fabricate the core. The GO was synthesized using modified Hummers' method [125]. The GO powder was dispersed in DMF solvent and ultrasonicated for 30 min at room temperature. PVDF pellet was separately dissolved in DMF with the same procedure as explained in section 3.2. The GO suspension was then added the PVDF solutions, and the mixture was stirred for an additional 3 hours. Different contents of GO (0.05 wt%, 0.01 wt%, 0.02 wt% and 0.05 wt%) were added to PVDF. Figure 3-20 shows the core-shell set up during the electrospinning process of PVDF-GO solution. The electrospinning process and set up was performed similarly to that described in section 3.2. It has to be mentioned that the flow rate for both solutions (interior core and exterior shell) was kept constant at 1ml/h. The electrospinning process was optimized to obtain a stable Tyler's cone for both solutions.

Table 3-5 shows the sample recipe for spin coated PVDF and electrospinning PVDF-GO samples. A spin coating PVDF sample was prepared by using a Laurell spin coater to assess the efficiency of electrospinning to promote the formation of β-phase. Several methods were used to characterize the electrospun PVDF nanofiber. The core-shell structure of PVDF-GO electrospun nanofibers was observed using TEM.

Table 3-5- Spin coater PVDF and electrospinning PVDF-GO samples.

Sample code	GO wt.%	PVDF concentration wt.%	DMF/Acetone (v/v)
Spin-PVDF	0	27.5	1.49
ES-PVDF	0	27.5	1.49
GO-0.05	0.05	27.5	1.49
GO-0.1	0.1	27.5	1.49
GO-0.2	0.2	27.5	1.49
GO-0.5	0.5	27.5	1.49

Figure 3-21 shows the TEM images of PVDF-GO electrospun nanofibers. As can be seen, the contrast in the TEM images differentiates the core structure of the nanofibers from shell structure.
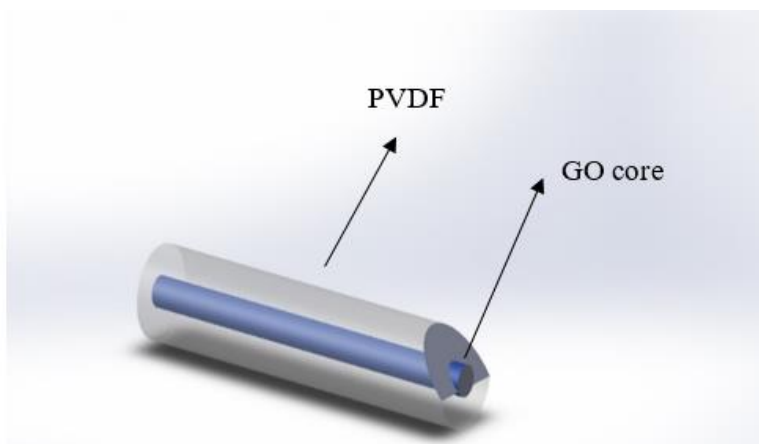
Figure 3-19- Core-shell structure of electrospun GO-PVDF nanofiber composite.
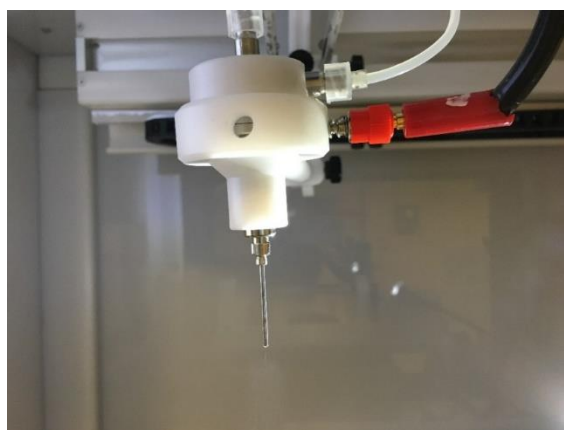
Figure 3-20-The core-shell set up during the electrospinning process of PVDF-GO solution.
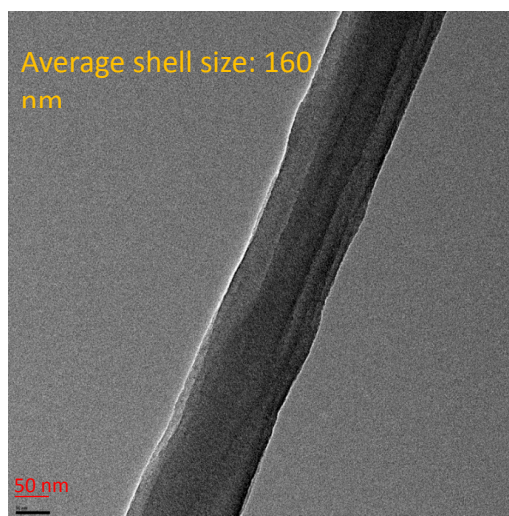
Figure 3-21- TEM images of core-shell PVDF-GO electrospun nanofibers.

Figure 3-22 shows the XRD results for electrospun PVDF; spin coated PVDF and electrospun GO–PVDF nanofiber composite. As shown, only one strong peak can be observed at 2θ of 20.6° for all the electrospun samples which are corresponding to (110) of the β-phase. In general, the higher content of GO resulted in higher relative peak intensity. However, the GO-0.2 % and GO-0.5% exhibited almost the same relative intensity peak. A diffraction peak for the spin-coater sample is observed at (2θ): 18.4° which is assigned to (020) crystal plane reflections of α phase form chain. However, this peak is disappeared for other samples implying the transition from α phase to β phase in electrospun GO-PVDF nanofiber composite. Figure 3-23 shows the FTIR spectra of electrospun GO–PVDF composites, electrospun PVDF, and spin coating PVDF composite. As explained in section 3.5, the absorbance peak at 766 and 840 cm^{-1} are assigned to α and β peaks, respectively.
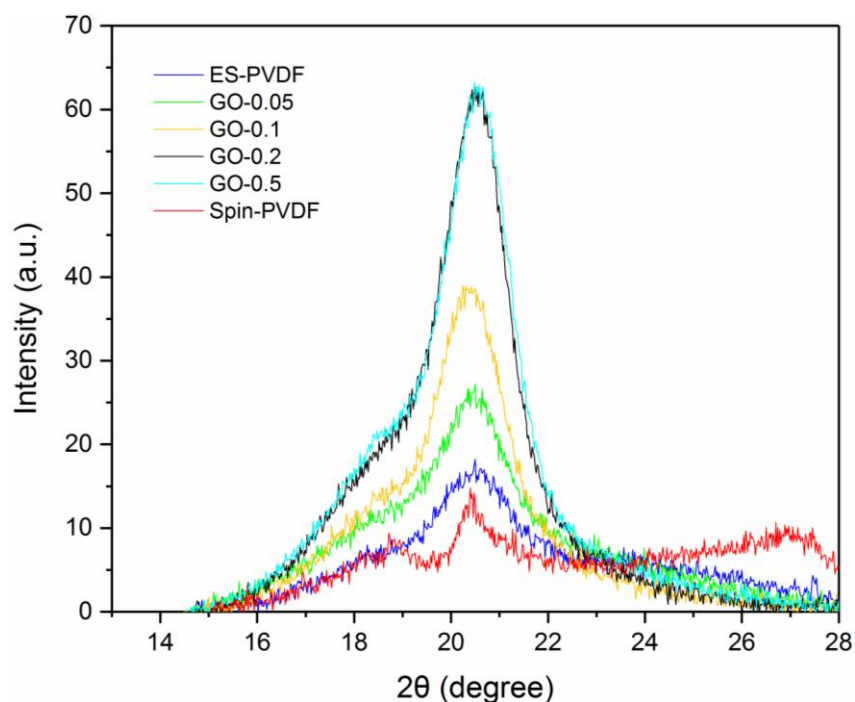
Figure 3-22- XRD patterns of electrospun GO–PVDF composites, electrospun PVDF, and spin coating PVDF composite. A peak can be observed at 2θ of 20.6° for all the electrospun samples which are corresponding to (110) of the β-phase.
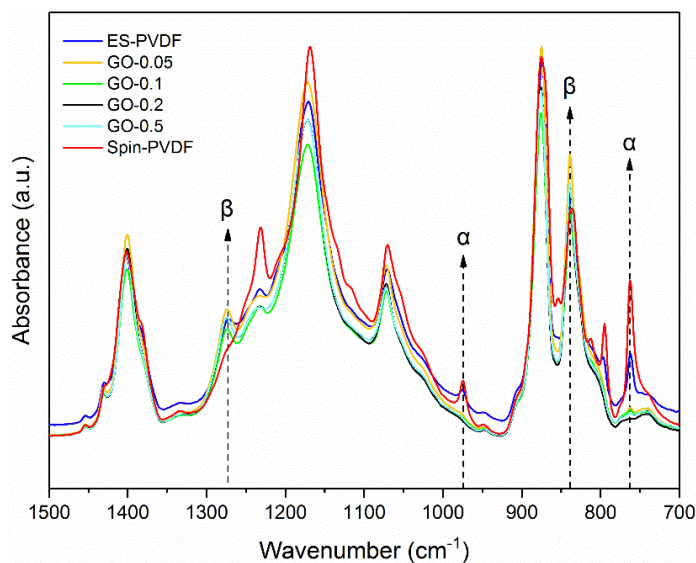
Figure 3-23- FT-IR spectra of electrospun GO–PVDF composites, electrospun PVDF, and spin coating PVDF composite. The absorbance peak at 766 and 840 cm−1 are the main peaks which represent the α and β phase of PVDF, respectively.

Each peak is shown separately in Figure 3-24 for better visualization. As can be seen, the major α peak has completely disappeared for GO-PVDF samples while it is apparent for both electrospun PVDF and spin coated PVDF. However, electrospun PVDF sample exhibited a lower relative intensity of α peak, indicating that the electrospinning process can promote the formation of β-phase. A clear shift in absorption band can be observed in Figure 3-24 which indicates the enhancement of β-phase in GO-PVDF composite. Also, the electrospun PVDF exhibited β-phase formation while spin coated sample produced the lowest amount of β-phase (53 %). The FTIR results were consistent with XRD analysis. The FTIR data was also used to quantify the electroactive phase content of PVDF using Eq. 1. The fraction of β-phase for electrospun GO–PVDF composites, electrospun PVDF, and spin coated PVDF composite is presented in Figure 3-25. As shown, the incorporation of GO enhances the β-phase content by providing a large surface area which increases the number of heterogeneous nucleation sites in the PVDF matrix. The β-phase content of electrospun PVDF/GO composites was considerably enhanced, as a comparison with that of the neat electrospun PVDF and spin coated PVDF. The β-phase content can reach up to 92 % for GO- 0.2 sample which is 23% and 73 % higher than the neat electrospun PVDF and spin coated PVDF, respectively. A considerable increase in β-phase content indicates the effectiveness of the core-shell structure in improving the phase transformation of α-phase to β-phase, even at a low content of GO. As shown, the incorporation of GO enhances the β-phase

content by providing a large surface area which increases the number of heterogeneous nucleation sites in the PVDF matrix. This might be because of the interaction between the π-bond in GO with the fluorine atoms and hydrogen atoms on adjacent carbon atoms in PVDF polymer chains. Therefore, all fluorine atoms are aligned on one side while the hydrogen atoms are aligned other side of the polymer chain of PVDF due to this interaction. The alignment of atoms at two sides of the polymer chain not only induces the beta phase formation but also results in a formation of a net polarized dipole moment along the core-shell structure of PVDG-GO nanofiber. The higher number of dipoles will impart the better piezoelectric and ferroelectric properties to PVDF-GO nanofiber composite. However, it seems that the increasing the dosage up to 0.5 wt% leads to a decrease in β-phase content. This implies that the 0.2 wt.% of GO is enough to nucleate the most of the PVDF polymer chain into the polar phase. Also, the fraction of β-phase in electrospun neat PVDF was found to be 75 % which has increased up to 41 % as compared to the one in the spin-coated sample. In fact, the PVDF nanofiber experiences an intense stretching force as collected on the drum which may lead to similar effect to that of the mechanical stretching process. Also, applying high electrical field during the electrospinning processes helps to orient the polar dipoles in PVDF structure. This process can be analogs to the electrical poling process. Therefore, it can be concluded that the electrospinning process promotes the formation of β-phase without any need for post-treatment processes including electric poling and mechanical stretching.
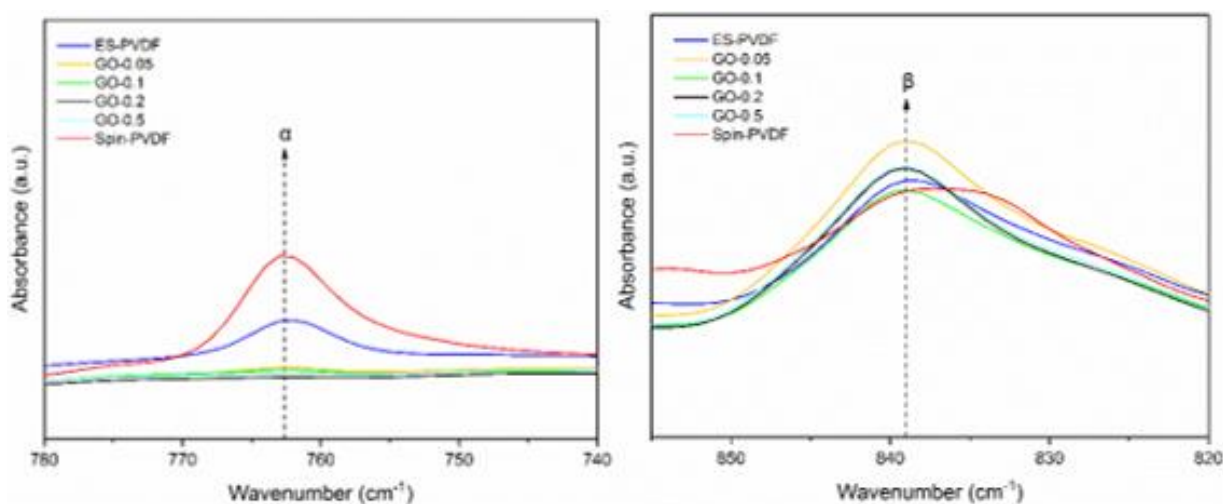
Figure 3-24- FT-IR wavenumber assigned to different phases of PVDF: left (**α**), right (β-phase).
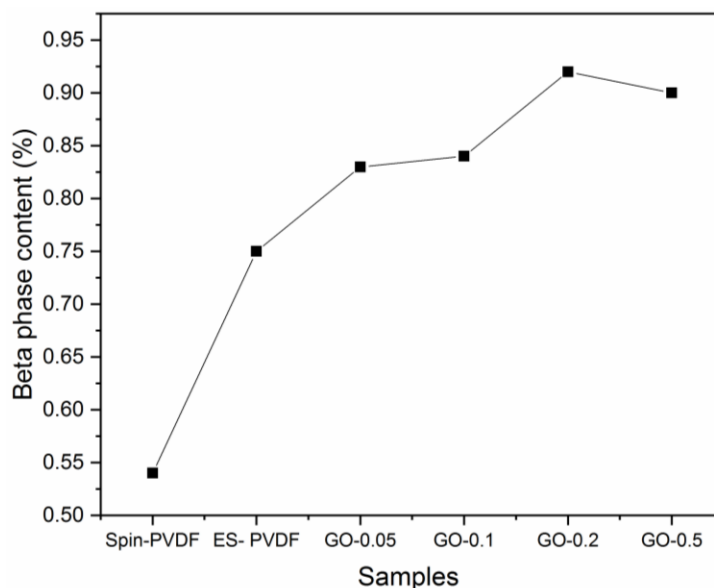
Figure 3-25- The fraction of β-phase for electrospun PVDF-GO composites, electrospun PVDF, and spin coated PVDF composite.

3.7. Piezoelectric coefficient measurement using piezoelectric force microscopy

This section aimed to determine the piezoelectric behavior of the PVDF and PVDF-GO samples. The piezoelectric force microscopy technique (PFM) analysis was also conducted to further investigate the effect of core-shell structure on the piezoelectric and ferroelectric properties of the PVDF-GO nanofiber composites. In particular, the experimental test was conducted to determine the piezoelectric coefficient (d_{33}) of the PVDF samples using PFM. In general, the surface of the nanofiber film was quite corrugated which make the PFM analysis difficult. The PFM measurement is very sensitive to the surface properties as the ideal situation for the measurement is the sample with a smooth surface. The samples were prepared with multiple thin layers of nanofiber mats in a way that crystalline lamellae are arranged on the surface with polymer chains oriented along the substrate. In this case, molecular dipoles are oriented vertically. Considering using electrospinning process, the applied electrical field was applied in such a way that the dipoles are aligned along the substrate. For the next step, the samples were deposited directly on the conductive substrates. A circular thin conductive steel plate was used as the electrodes to collect the fibers. The configuration of the experimental set up is shown in Figure 3-26. Two samples were considered for these series of the experiments which includes the optimized PVDF M_2 sample (section 3.5) and the GO-0.2 %.
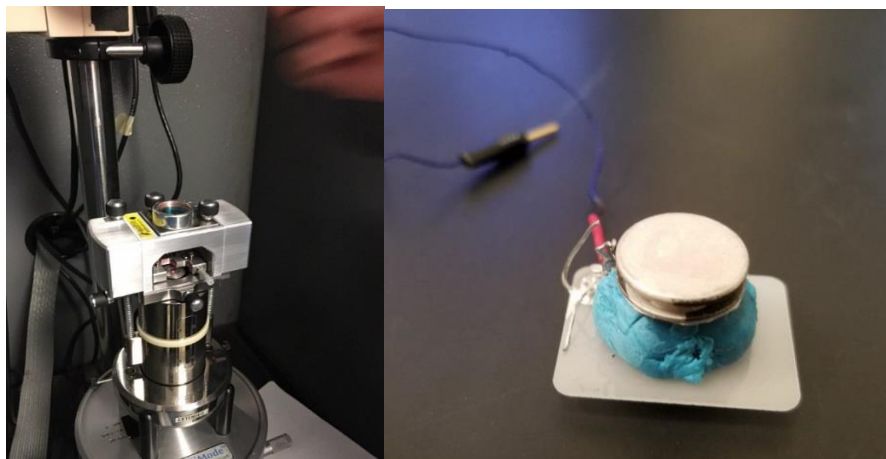
Figure 3-26- Sample preparation for the AFM analysis on a conductive substrate using a conductive paste

A contact mode was used to study the topography of the PVDF nanofiber sample. The AFM images of the nanofiber are shown in Figure 3-27. As shown, the morphology of the nanofiber can be observed which confirms the obtained morphology of the nanofiber using SEM.
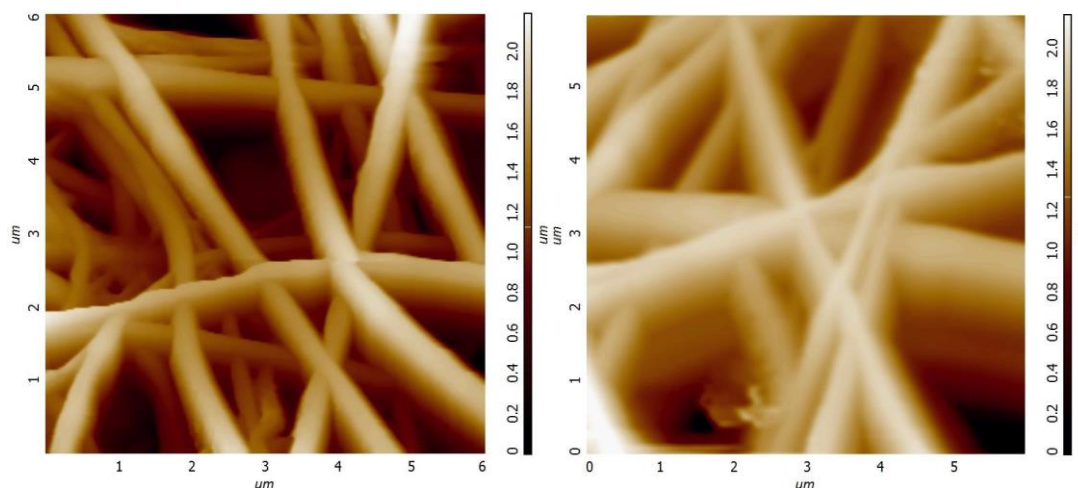
Figure 3-27-Morphology of the PVDF nanofiber using AFM method

The PFM signal was captured using a lock-in amplifier and a conductive tip (NSG01/Pt cantilevers). The PFM analysis was conducted to measure the piezoelectric response of the nanofiber piezoelectric sample. It has to be noted that the lack of bond between the sample and the bottom substrate has caused several failures to detect the piezoelectric signal. In fact, PFM measurement requires the sample to be attached well to the electrode under the sample, while AFM tip acts as a second electrode from above. When they are not in direct contact with the electrode like in these two samples, PFM response cannot be detected because the electrostatic interaction between the tip and the substrate is much stronger. In order to address this problem, a

layer of conductive silver paste was used as a bottom electrode to provide enough bonding between the PVDF sample and the bottom electrode.

The PFM response of the PVDF nanofiber samples was recorded by fixing the conductive tips location on a certain point and applying a dc voltage from -10 V to 10 V. The PFM response indicates the changes in the signal when the DC voltage applied between the conductive tip and the bottom electrode. First, the DC voltage is increased to +10V; then it starts to decrease linearly to -10V and then it is increased back to +10V. An electric excitation of 3V at 10 kHz was applied to the tip during the measurement.

The PFM analysis is conducted based on the measurement of the piezoelectric samples deformation induced by applying an electrical field. The piezoresponse of the sample is captured using a lock-in by monitoring the vertical vibration of the conductive cantilever beam. In addition, PFM can be used for investigating the ferroelectric properties of the samples. In fact, the analysis of ferroelectric properties is based on this fact that the ferroelectric materials are necessarily piezoelectric. The conductive cantilever beam can detect the vertical deformation of the samples which is corresponded to the out of plane displacement due to the d_{33} coefficient.

In order to better understand the piezoelectric behavior of the samples, the hysteresis piezoelectric response of each sample was recorded and analyzed using the PFM technique. The PFM technique involved the analyzing the surface of the PVDF nanofiber to determine the polarization domain and the ferroelectric behavior. The piezoresponse of the PVDF nanofiber sample was determined by measuring the strain and polarization dependence of the bias applied voltage. Figure 3-28 shows the hysteresis piezoelectric response as a function of the applied voltage for the PVDF nanofiber sample. As shown, two main responses (amplitude and phase) are plotted against the applied voltage. In this curve, the amplitude represents the magnitude of the electromechanical coupling, and the phase provides the information about the polarization dipoles and their orientation. When the applied voltage increases from -10 V to + 10V, the polarization changes abruptly at a certain point which is the coercive field. This transition implies that most of the dipoles in PVDF nanofiber are oriented along the electrical field. When the electrical field is reserved, the amount of polarization is reduced, and again at the negative coercive field, a polarization transition happens in which the polarization tends to decrease. As can be seen in Figure 3-28, the PVDF sample shows the piezoelectric response (butterfly curve) which implies the piezoelectric and ferroelectric behavior. Also, the phase diagram indicates that the polarization

domains has been switched around 180 degrees, while the dc voltage swept from -10 V to 10 V. The abrupt transitions in the phase curve was occurred at voltage around 2.5 V. In fact, at this coercive field, the phase changes by 180°, implying that the polarization domains are switched by the applied electric field. This results not only confirm the piezoresponse but also indicate the ferroelectric properties of the PVDF nanofiber sample. The d_{33} coefficient of the PVDF nanofiber was determined to be 32 pm/V based on the butterfly curve. Figure 3-29 presents the amplitude butterfly curve and phase hysteresis loop for PVDF-GO-0.2%. The results indicate the phase change transition at a voltage around 2.5 V which confirms the polarization of the dipoles under the electrical field and piezoresponse of the nanofiber. The noisy data might be due to the slipping the conductive tips over the nanofibers which cause the instability in recording the data. As shown, the core-shell structured PVDF-GO nanofiber exhibited a higher piezoelectric response compare to PVDF by exhibiting higher amplitude. The d_{33} piezoelectric coefficient of PVDF-GO was found to be 61 pm/V which is almost two times higher than PVDF sample. The results are in a good agreement with the previous results including XRD, FTIR and confirms the formation of higher beta phase in PVDF-GO nanofiber composite. The enhancement of the piezoelectric coefficient can be attributed to the higher beta phase dipole which can induce a stronger displacement in the sample as a result of the applied electrical field. The results clearly prove that the core-shell structure of PVDF-GO is beneficial to enhance the piezoelectric behavior of the PVDF. In addition, the results confirm the piezoelectric and ferroelectric properties of both PVDF and PVDF-GO sample which implies that the electrospinning method is very effective to promote the β-phase formation in PVDF nanofiber without any need for the post-treatment process. The enhancement of the piezoelectric coefficient can be attributed to the higher beta phase dipole which can induce a stronger displacement in the sample as a result of the applied electrical field. Also, the results clearly prove that the addition of GO is beneficial to enhance the piezoelectric behavior of the PVDF. In addition, the results confirm the piezoelectric and ferroelectric properties of both PVDF and PVDF-GO sample which implies that the electrospinning method is very effective to promote the β-phase formation in PVDF nanofiber without any need for the post-treatment process.
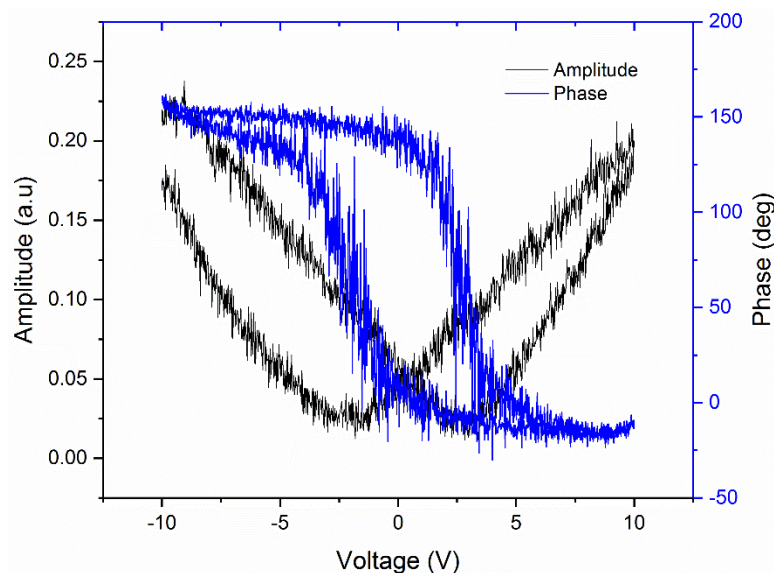
Figure 3-28- The PFM Hysteretic curve of phase and amplitude of the PVDF.
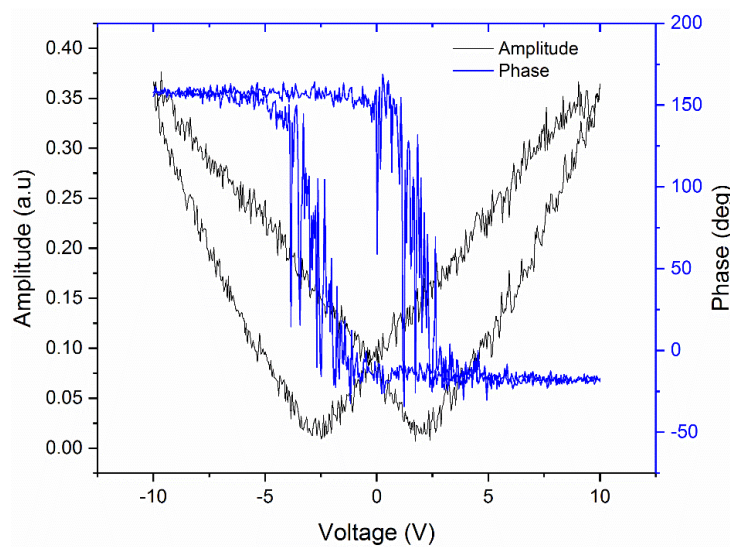
Figure 3-29- The PFM Hysteretic curve of phase and amplitude of the PVDF-GO.

Table 3-6 presents the d_{33} coefficent of the most common types of piezoelectric materials including PZT, ZnO and PVDF along with the obtained d_{33} coefficent results from this research work. As can be seen, the PVDF-GO exhibits the highest d_{33} coefficent among all the PVDF samples.

Table 3-6-The piezoelectric coefficient of piezoelectric materials along with this work results

Materials	d_{33} (pm/V)	Sample	Processing method
PVDF (this work)	32	Nanofiber	Electrospinning
PVDF-GO (this work)	61	Nanofiber	Electrospinning
PVDF [41]	17.4	Thin film	Spin coating
PVDF [42]	30	Nanofiber	Electrospinning
PZT [43]	330	Thin film	Molecular-beam epitaxy
PZT [44]	380	Nanofiber	Electrospinning
ZnO [45]	9.2	Nanowire	Hydrothermal
ZnO [46]	26.7	Nanobelt	Vapor transport deposition
ZnO [47]	6.4	Thin film	Pulsed laser deposition

CHAPTER 4.   DEVICE FABRICATION AND APPLICATIONS

4.1.   Fabrication of flexible device

The interdigitated electrode device (IDE) has been widely used for fabrication of sensors and energy harvester [126]. The electrode pattern in IDE device provides a tool for utilizing the piezoelectric d_{33} mode, which leads to higher power output [73]. Moreover, the electrode pattern on IDE-based can be optimized in such a way to match the frequency of the mechanical vibration [88]. In this thesis, an IDE-device is fabricated using lithography process and Inkjet printing method.

Device fabrication using lithography process is based on conventional lift-off procedure as shown in Figure 4-1. It should be mentioned that the whole process was performed in the clean room. The Kapton and PET were used as substrates to make the flexible device.
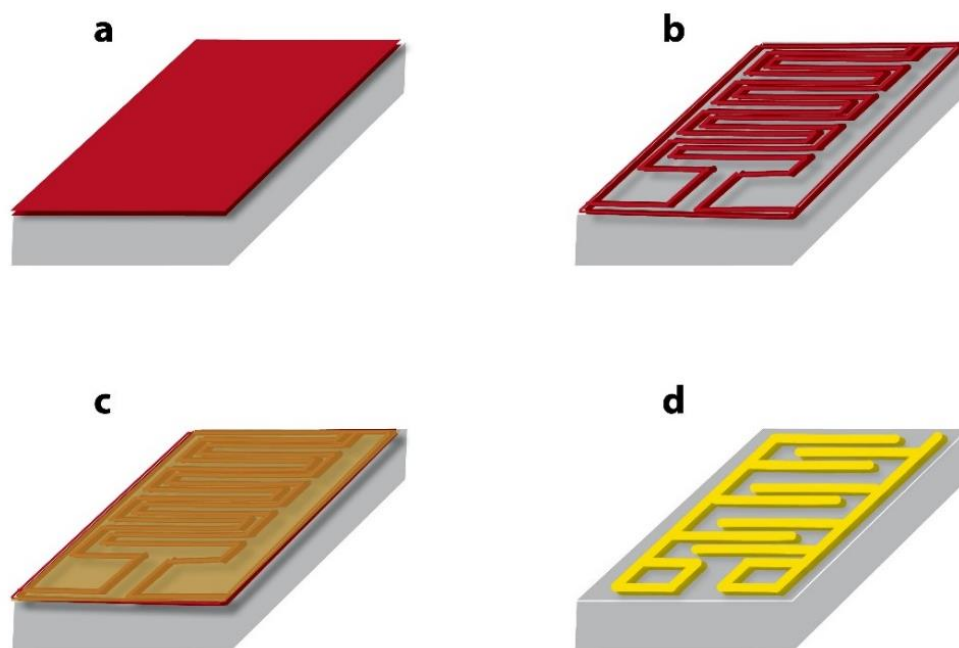
Figure 4-1-The fabrication process of interdigitated electrode device; a) The PR spin coating b) Mask alignment c) Deposition of Ti/gold d) Lift-off.

The fabrication process of the flexible device using lithography method involved several steps. The flexible substrate was first chemically cleaned for the removal of any residual contamination matter from the surface of the substrate. The cleaning process involves soaking the

substrate in toluene, acetone, isopropanol and for 5 minutes each and rinsed with DI water at the end. The substrate was then dried with nitrogen gas. A photoresist (PR) material was spun on the flexible substrate using a spin coater in three consecutive steps: 1) 1s ramp to 500 rpm, dwell 10 s; 2) 2s ramp to 2000 rpm, dwell 40 s; 3) 2s ramp down to 0 rpm. The substrate was then baked at 90 ℃ for ten minutes. The mask alignment systems allowed accurate alignment of substrates with a mask and exposed them to ultraviolet radiation to transfer the pattern of the mask to the substrate for further processing to produce an interdigitated device. The e-beam evaporation was used to deposit a 10-nm chromium film layer as an adhesion layer followed by deposition of a 90 nm of the gold layer as an electrode. Figure 4-2 illustrates the IDE after e-beam evaporation process and the final deposited gold layer on it as the conductive electrode. The PR was then removed by soaking the samples in acetone bath under the fume hood for 14 hours. The PR was removed successfully, and the IDE electrode pattern was formed on the flexible substrate. A photo of the final interdigitated electrode is illustrated in Figure 4-3. After that, the lift-off process defines the electrode area, and electrospinning was performed to deposit PVDF nanofibers. Finally, a PDMS layer was spun on the device for protection and reducing the noise. The lithography method is a very accurate method to produce the high-quality IDE device. However, the lithography method involves several steps such as mask alignment, etching, and lift-off process which are mainly done in the clean room. Therefore, the lithography is an expensive and time-consuming process. Moreover, the expensive and complicated process of lift-off lithography method is not suitable for large-scale applications which mostly is required for civil engineering applications. Hence, the inkjet printing method as a cost-effective and easy process was also considered in this study to fabricate the IDE device. The inkjet printing has been used recently to print the flexible devices such as MEMS device [127; 128], the light guide plate of a display [129] and flexible chemical sensor [130; 131]. There are two types of an inkjet printer including the thermal bubble and piezoelectric-based printer. The thermal bubble printer uses a resistor in the head. By passing the electrical current, the resistor will heat up. The resistor then gives off the heat to vaporize the conductive ink and make gas bubbles. The latter can push out the ink of the nozzle in the form of the droplets [132]. The piezoelectric printer uses a crystal piezoelectric head which is excited by an electrical signal. The applied voltage causes the piezoelectric to deform and finally push the ink out of the reservoir as droplets. Both printers were used in a verity of the applications, but It has

been reported that the piezoelectric printer has better performance since it doesn't change the properties of the conductive ink [133].
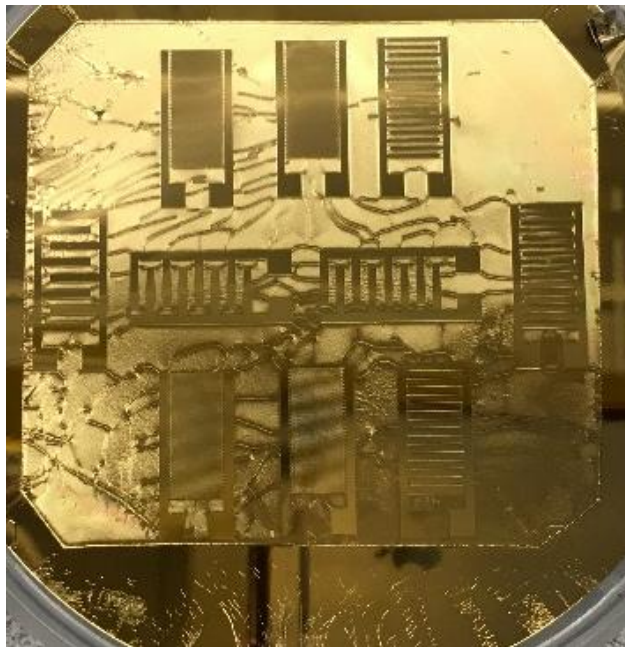
Figure 4-2- The IDE device after e-beam evaporation process. A 10 nm chromium film layer was deposited as an adhesion layer followed by deposition of a 90 nm of the gold layer as an electrode.
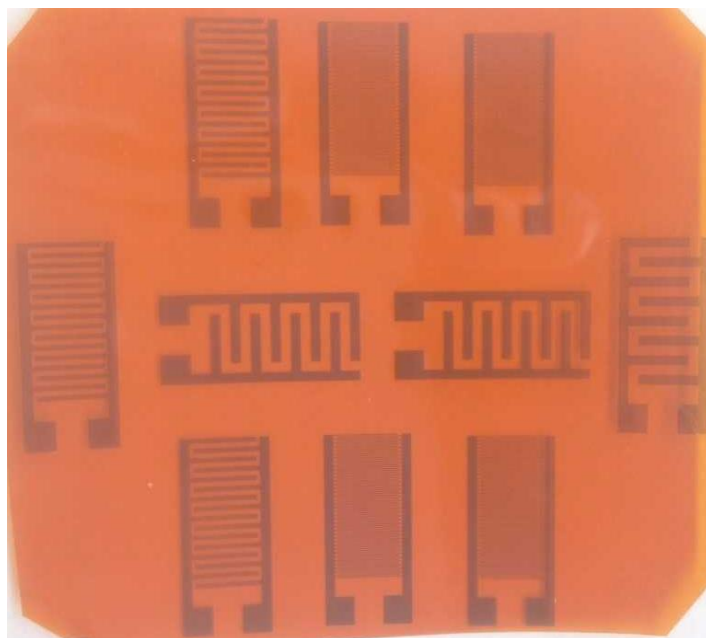
Figure 4-3- A flexible interdigitated electrode using lithography method.

In this study, a piezoelectric -based Dimatix inkjet printer (DMP-2850) was used to deposit the silver electrode on the flexible substrate (Figure 4-4). This printer allows the deposition of the

silver ink on the flexible substrate using a piezo inkjet cartridge. The properties of the ink play an important role during the printing process. The viscosity of the ink needs to adjust to being in certain range (25-30 cP). In this study, a commercial silver ink (Centrix JS-B25HV) was used to deposit the conductive electrode on a PET substrate. The pattern was drawn and edited using the program of the printer. The experiments involved some trial deposition at the beginning to obtain the appropriate resolution and thickness of the conductive layer. This process was controlled by using the waveform editor which alter the electrical pulse properties to optimize the ink droplets.

The PET substrate was used in this study to fabricate the flexible PVDF device. The PET substrate was cleaned by soaking the substrate in toluene, acetone, isopropanol and for 5 minutes each and rinsed with DI water at the end.

Figure 4-4- Dimatix material printer (DMP-2850) with a piezo inkjet cartridge.

After optimizing the parameters of the waveform by executing the trial printing. The piezoelectric head was excited so that the deflection of the piezo head induces a pressure to expel the ink out of the nozzle. The multiple patterns were printed at the same time. The resolution of the printed pattern depends on several parameters such as ink properties, substrate, and the droplet size. The inkjet printing software allowed to deposit the multiple electrode patterns on the substrate.

Figure 4-5 shows the inkjet process from the top view and front view. This printer can create and define patterns over an area of about 200 x 300 mm and handle substrates up to 25 mm thick with an adjustable Z height.

Figure 4-6 shows the IDE pattern using the silver ink as an electrode. The IDE pattern then adhered on the drum collector during the electrospinning process. This allows the electrospun PVDF nanofiber to be deposited directly on the silver electrode.
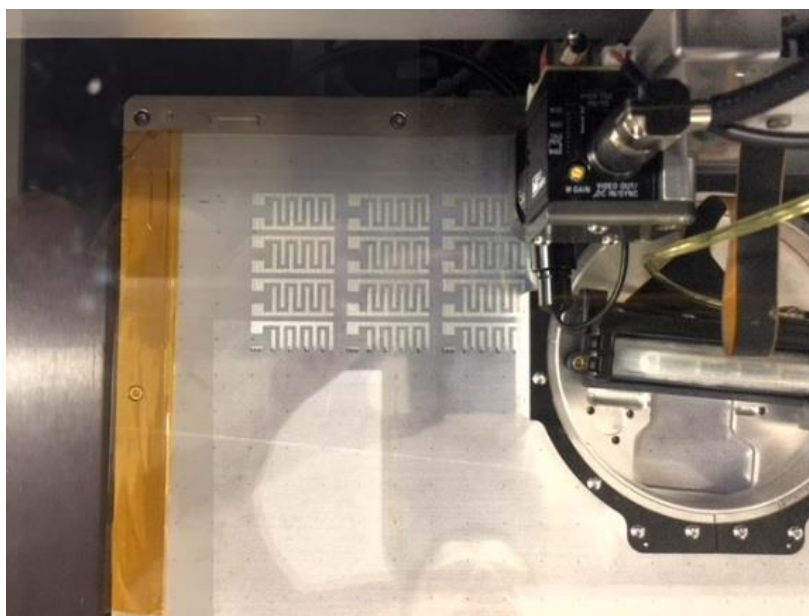
Figure 4-5- The inkjet printer process from above (left) and front view (right)

In order to enhance the durability of the PVDF device, the IDE along with the electrospun PVDF nanofiber was covered by a PDMS layer. The wires were then connected using the silver epoxy. The final piezoelectric device is shown in Figure 4-7.

Figure 4-6- The pattern of IDE electrode using the inkjet printing process.
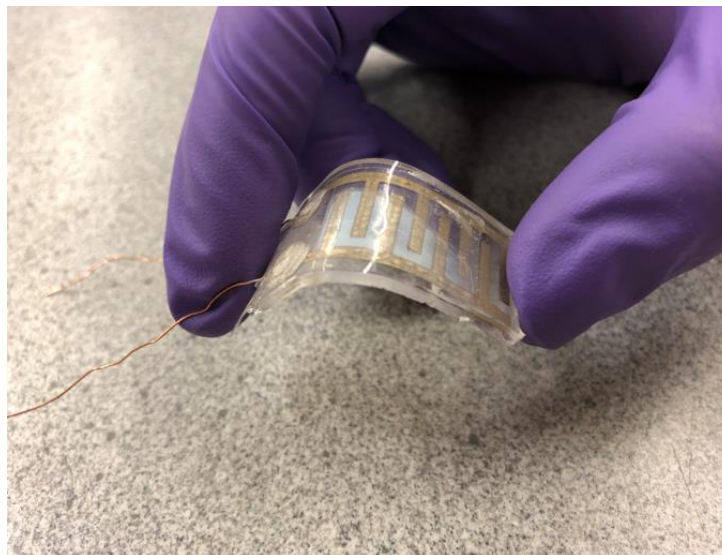
Figure 4-7- The piezoelectric IDE device encapsulated in PDMS.

The simultaneous using of PDMS and PET substrate not only enhance the flexibility of the PVDF device but also make the device to be fully transparent. Also, the inkjet printing involves fast and inexpensive process electrode compared to the lift-off lithography process. This method allows depositing multiple patterns at the same time (Figure 4-8).

Figure 4-8- Multiple piezoelectric PVDF devices made by inkjet printing process

Other than the interdigitated device an ordinary PVDF device was fabricated in which the electrospun PVDF mat was sandwiched between two conductive electrodes. The thermal evaporation method has also been used in several applications to for deposition [134-136].

The thermal evaporation was used to deposit the electrode on the flexible substrate. The electrospun PVDF was then transferred to the electrode. A 100-nm silver was then deposited on both side of the flexible substrate by vacuum evaporation through a shadow mask at the rate of 1 Å/s under the vacuum of $< 7 \times 10^{-4}$ Pa. Similar to the previous methods, the whole sensor was then packaged using PDMS for further protection. Figure 4-9 shows the thermal evaporator to deposit the silver electrode on both sides of the PVDF and the flexible substrate.

Figure 4-9-Thermal evaporator to deposit the conductive electrode on the samples.

In summary, the resolution of the printed pattern using inkjet printer is not as good as that obtained by thermal deposition and lift-off lithography. The control of the thickness of the conductive layer was also found to be very difficult during the printing process and was not as accurate as other methods. However, the inkjet printing process is very cheap, fast, and efficient to deposit the conductive electrode over a large area. Hence, this method is recommended for large-scale application. The advantage of the thermal evaporation method over the inkjet and lithography process was that the thermal evaporation could be used to deposit the electrode directly on the PVDF material, while the inkjet printing and lithography can be used only to deposit the electrode on a flexible substrate.

4.2.   Energy harvesting application

The piezoelectric energy harvester converts the mechanical energy to electrical which can be used as a sustainable source for different electronic devices such as sensors. In general, a

piezoelectric energy harvester consists three main parts: a generator to converts mechanical energy into electrical energy, a booster to amplify the generated voltage, and a storage part to store the energy. This chapter aims to study the feasibility of the developed PVDF device for converting the mechanical energy into electrical energy. The piezoelectric energy harvester in civil engineering can be used as sustainable energy source to power the small electronic devices such as wireless sensor network. In fact, the mechanical vibration can be used as a free source to power the wireless sensor which leads to a reduction in the maintenance costs for battery replacement and also the chemical waste of conventional batteries.

When the PVDF piezoelectric device is bent, compressive stress is applied on the nanogenerator. This stress will generate a piezoelectric potential due to the direct piezoelectric effect. In order to balance the piezoelectric potential, the free electron moves from low potential to high potential side and accumulate at the surface of the electrodes. When the pressure is removed, the free electron will move back and a voltage signal pulse associated with an opposite pulse voltage output. In order to study the energy harvesting ability of our device, the voltage signal output of nanogenerator was recorded in two steps. At first step, the nanogenerator was not subjected to the load (Figure 4-10), and the output voltage shows zero voltage output (Figure 4-10). At the second step, the nanogenerator was subjected to a compression force, and the positive and negative signal output was observed as shown in Figure 4-11.

The positive sign was attributed to the compressive stress which causes the PVDF nanofiber membrane to deform, while the negative sign derived from the remove of the compressive force and subsequently induced strain. Therefore, by applying and removing the load in each cycle, the positive and negative voltage signals were observed. It is important to mention that no external load resistor was used in this study.

An energy harvesting performance set-up was also developed in the SMART lab to assess the efficiency of the nanogenerator voltage output at the different frequencies. The PVDF nanofiber membrane was firmly clamped between two plates to simulate the cantilever beam behavior. In order to evaluate their strain-sensing performance, an electromechanical generator excited from 20 Hz to 100 Hz by a function generator which apply periodic force on the cantilever beam. Figure 4-12 shows the energy harvester set up to evaluate the energy harvesting performance of the PVDF nanogenerator in both inactive and active condition. An oscilloscope was also used to record the voltage output of the piezoelectric device.
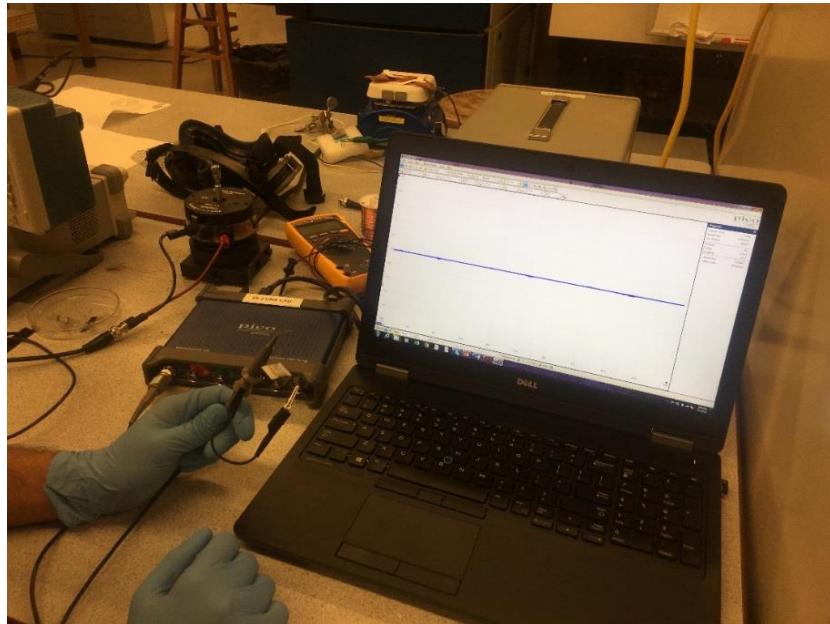
Figure 4-10- Unloaded nanogenerator and no signal output.
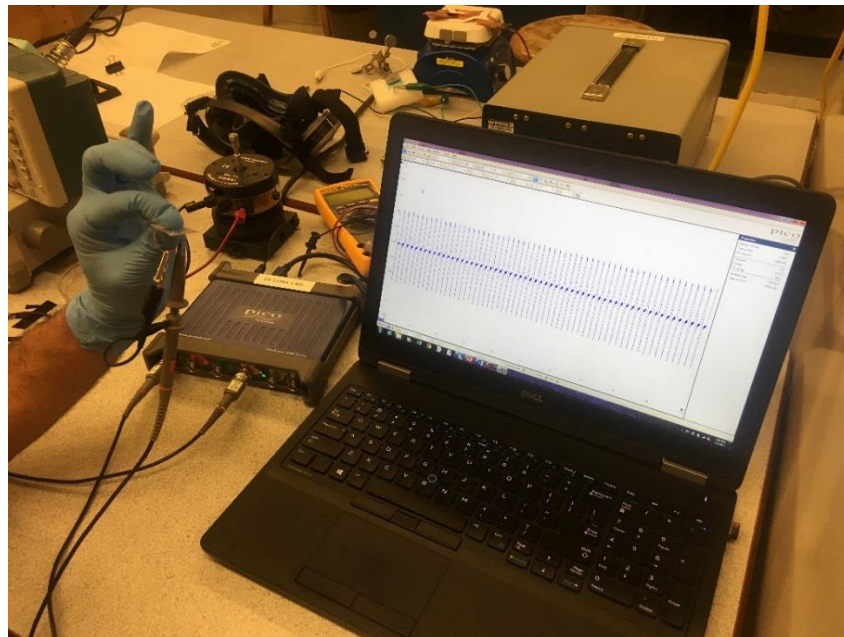
Figure 4-11- The nanogenerator under load and the signal output.

The main problem in energy harvesting in civil infrastructure is the mismatch between the intrinsic frequencies of harvesters and the resonant frequencies of the civil infrastructure. It is very difficult to match the resonant frequencies of the energy harvesters to match the mechanical

vibration frequencies due to the high stiffness and brittleness of piezoelectric patches [137]. Generally, the ambient vibration frequencies in civil infrastructure which are usually several Hz (lower than 30 Hz). Moreover, even if the resonant frequency can be tuned as low as required, the limitation of small strain allowed in piezoelectric patches will lead to a low energy output power [137]. Figure 4-13 shows a typical voltage output of nanofiber device with an active area of 2.25 cm^2 at the frequency of 30 Hz. As can be seen, the PVDF nanogenerators exhibit a maximum peak output voltage of 450 mV at the frequency of 30 Hz.
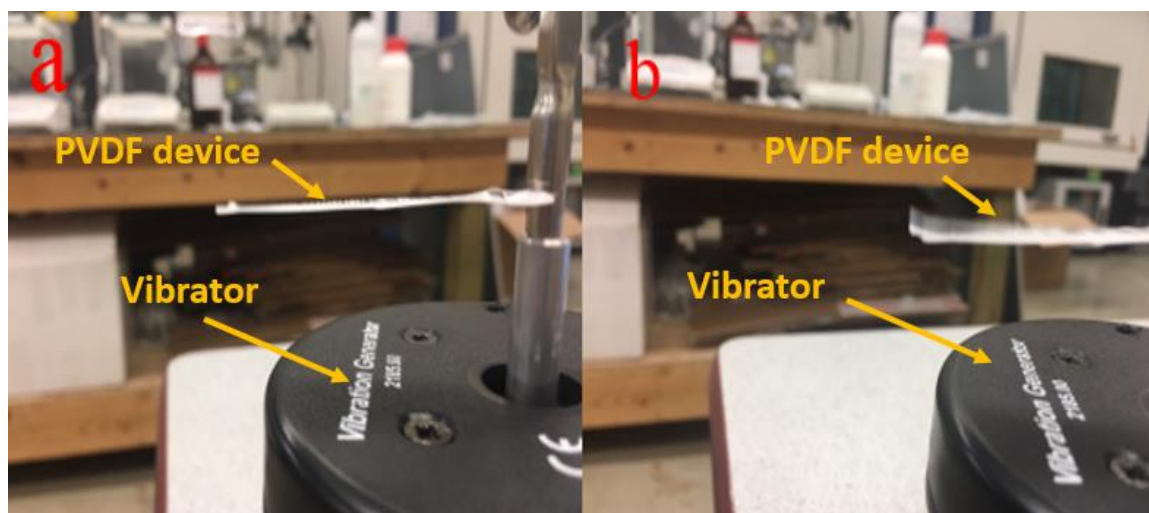
Figure 4-12- An energy harvester set up to evaluate the energy harvesting performance of the PVDF nanogenerator in (a) inactive (a) and (b) active condition.
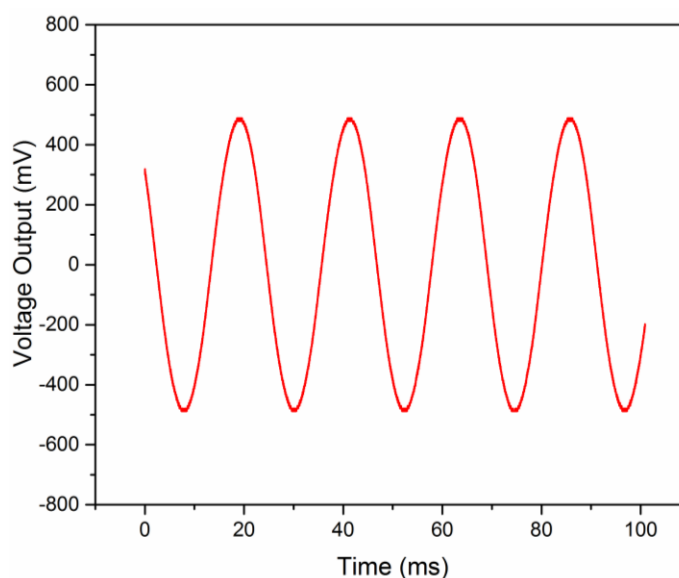
Figure 4-13-Voltage output measurement by oscilloscope at the frequency of 30 Hz.

4.3.   **The effect of different mechanical vibration parameters on the voltage output**

In general, the amplitude and the frequency are two important parameters of the AC signal wave which characterize the properties of AC signal. The frequency of AC signal is the rate of changing direction and is determined based on the number of forwards/ backward cycles per second, while the amplitude is defined as the maximum voltage achieved by the AC signal. The applied mechanical vibration generates the AC waveform which can excite the piezoelectric device to generate power. In fact, the properties of AC excitation signal will affect the performance of the piezoelectric device and, as a result, the voltage output. Therefore, the study of the AC signal's parameters is of great importance. With this in mind, this section aimed to study the effect of the frequency and amplitude of the AC signal on the voltage output of the PVDF nanofiber piezoelectric device. The device was made using the lift-off lithography process (as discussed in section 4.2). The samples were encapsulated by a PDMS protective layer.

The frequency range was varied from 20 Hz up to 100 Hz, while the mechanical vibration set-up was excited with an AC signal with varying amplitude. The amplitude voltage is reported as "peak to peak" (Vpp) which indicates the difference between the maximum positive and the maximum negative amplitudes of a waveform. The AC signal was generated with amplitude from 3 Vpp to 20 Vpp. Figure 4-14 shows the variation of the voltage output with different frequency at the fixed amplitude of 5 Vpp on the voltage output of the piezoelectric device. As can be seen, the frequency variation exhibited a significant effect on the voltage output. The frequency of the signal was increased up to 100 Hz in 5 Hz increments, while the voltage output was recorded at each step using an oscilloscope.

The results indicate that the obtained voltage output at the frequency of 20 Hz is 109 mV. As can be seen, the voltage output of the PVDF device is enhanced when the frequency increased. The highest voltage peak was obtained at the frequency of 45 Hz. As shown, the voltage output became 200 mV when the frequency was increased up to 45 Hz.
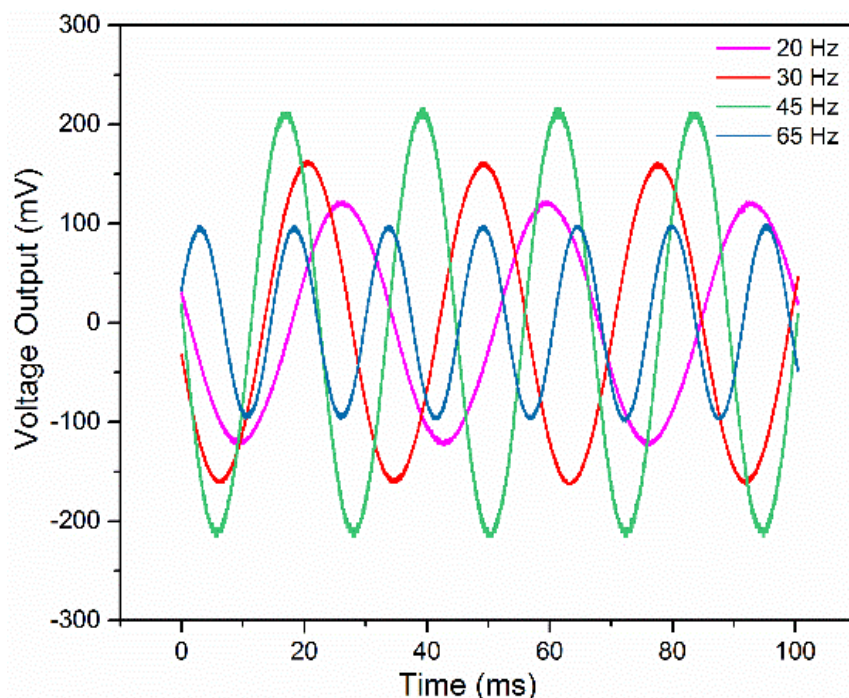
Figure 4-14- The voltage output at AC signal with amplitude of 5 Vpp versus the frequency ranges

This experiment was repeated to determine the effect of the frequency variation on the voltage output at a higher amplitude. The amplitude of the signal as increased to 20 Vpp. Figure 4-15 presents the voltage output of the piezoelectric device as a function of the frequency at fixed 20 Vpp amplitude. In general, the variation of the frequency with the AC amplitude of 20 Vpp exhibited the same trend as the AC amplitude of 5 Vpp. However, as can be seen, the effect of the frequency variation on the voltage output is more pronounced when the AC signal is applied with higher amplitude. For example, the highest peak of the voltage output is 850 mV with the AC amplitude of 20 Vpp, which is almost 7 times higher than the voltage output of the device with the AC amplitude of 5 Vpp.

According to the results, the optimized frequency range for the device was found to be 45 Hz. However, the voltage output starts to decrease with further increase of the frequency. Figure 4-16 presents the maximum obtained voltage output as a function of frequency at both amplitudes of 5 Vpp and 20 Vpp. As can be seen, the variation of the amplitude has a great influence on the voltage output of the piezoelectric device. Both curves show the maximum voltage output at 45 Hz regardless of the amplitude range.
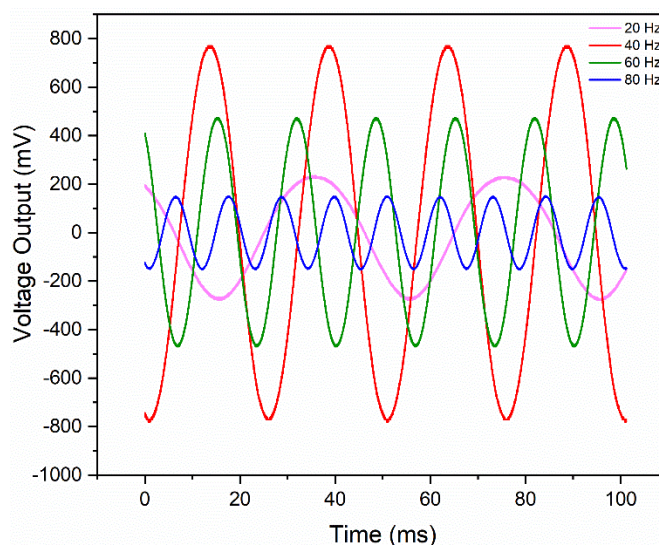
Figure 4-15- The voltage output at AC signal with an amplitude of 20 Vpp versus the frequency ranges.

The results indicated that the voltage output starts to decay at a higher frequency which can be due to the insufficient time for the PVDF nanofiber to be recovered from the induced strain. The results imply the efficiency of the developed piezoelectric device for low-frequency cases.

To analyze the effect of the amplitude the frequency of the AC signal was fixed at 45 Hz, and the amplitude varied from 3 Vpp to 20 Vpp. Figure 4-17 shows the variation of the voltage output of the piezoelectric device for the amplitude of 5 Vpp, 10 Vpp, 15 Vpp and 20 Vpp.
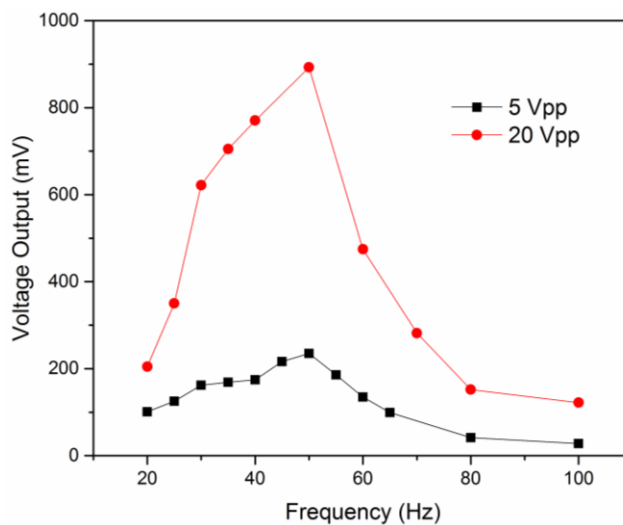
Figure 4-16-The maximum voltage output at AC signal with different amplitude
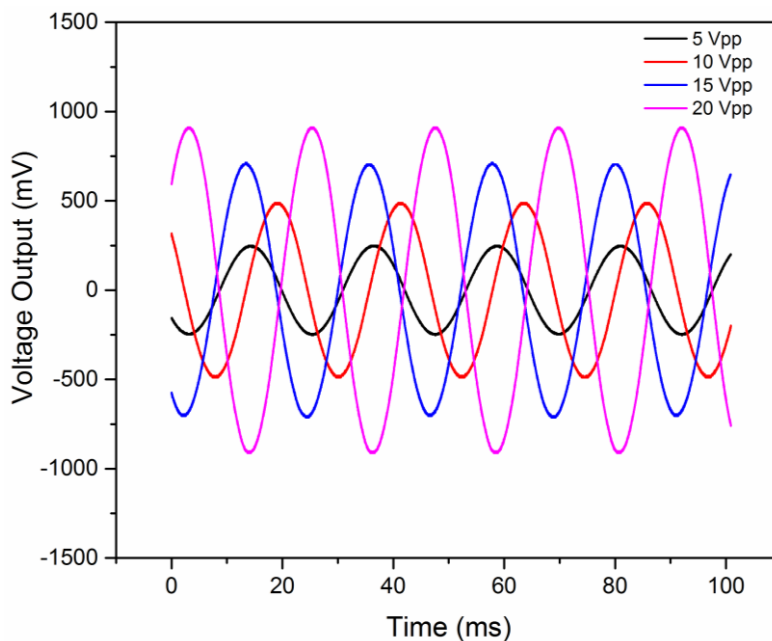
Figure 4-17- The maximum voltage output at AC signal with a different amplitude at the fixed frequency of 45 Hz.

The highest peak of the voltage output was plotted versus the amplitude in Figure 4-18. As shown, a perfect linear relation can be observed between the amplitude and the voltage output.
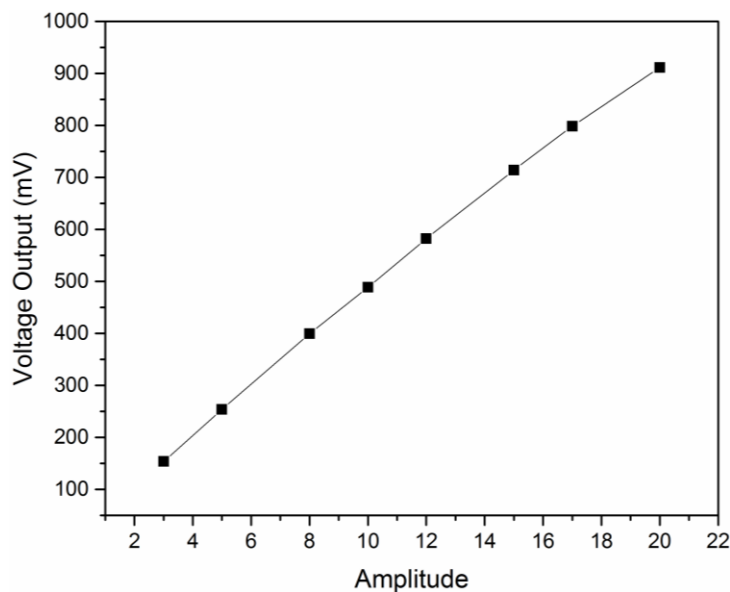
Figure 4-18- The maximum voltage output at AC signal with different amplitude at the fixed frequency of 45 Hz

The voltage output is increasing with increasing the amplitude. One possible for this results is that the higher amplitude AC signal induces higher strain on PVDF samples which leads to higher charge separation and voltage output according to the following equation:

$$V_{output} = d_{33}EsT/\varepsilon^T \qquad\qquad (4\text{-}1)$$

Where ε^T is permittivity under a constant strain, d_{33} is the piezoelectric coefficient, s is the amount of induced strain, E is Young's modulus and, T is the thickness of the film.

Since Young's modulus, thickness and voltage coefficient are the same for the piezoelectric device in this experiment. Therefore the strain can be considered as the only parameter which can affect the voltage output. In fact, the amount of induced strain can be considered as the main source of the available mechanical energy which can be fed into the piezoelectric device to be converted to the electrical energy. The results clearly suggested that both frequency and amplitude can affect the voltage output of the piezoelectric device. Therefore, an interaction effect of these two parameters has been analyzed to have a better understanding the effect. Figure 4-19 shows the two-dimensional counter plot which shows the interaction effect of the amplitude and frequency of the AC signal on the voltage output. The highest voltage output can be obtained by highest amplitude and the frequency range between 30-45 Hz. This range of frequency has been reported as a typical frequency of the bridges [138]. The obtained voltage output generated in a low-frequency range might be beneficial in harvesting electrical energy from the existing mechanical vibration in civil infrastructure. The obtained voltage output proved the feasibility of the electrospun PVDF nanofiber to convert the mechanical vibration to the electricity without any post-treatment processed. The results can assist in adopting the electrospun nanofiber device in energy harvesting application in infrastructure such as bridge deck and highway pavement.
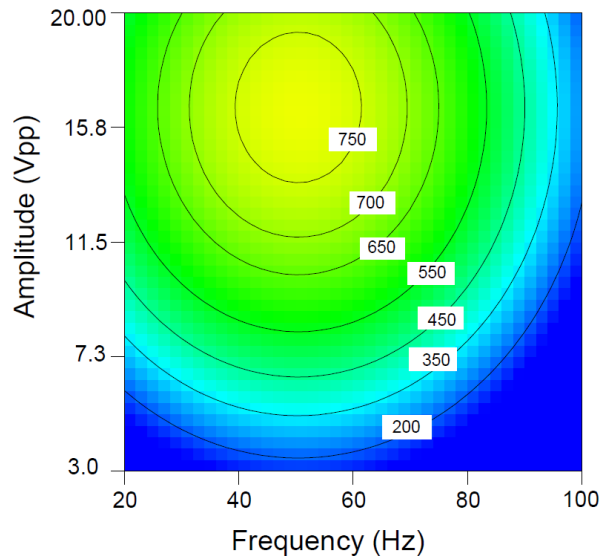
Figure 4-19- The maximum voltage output at AC signal with a different amplitude at the fixed frequency of 45 Hz.

4.4.   Sensing applications

The piezoelectric devices have proved the capability of sensing in a variety of applications such as detecting cracks, corrosion, gas sensing, strain sensing, etc [139-142]. The passive sensing process does not depend on the external power source while the active sensing requires an external source of power to operate. This section aims to investigate the feasibility of using electrospun PVDF nanofiber in both passive and active sensing state. The pitch-catch approach was considered for the active sensing approach. Acoustic emission monitoring was also considered as a passive method which can detect the defects and cracks in structures by capturing the acoustic waves generated due to crack opening and propagation.

4.5.   Pitch-catch application

The active sensing is the most common type of health monitoring systems to assess the condition of the structures by providing the real-time information about the properties, deterioration, strain, etc. The pitch-catch is one of the most efficient active sensing methods which has recently gained more attention in a variety of the engineering field [143-145].

In this approach, a piezoelectric transducer acts an actuator to propagates the Lamb waves while another piezoelectric device works as a sensor to detect the signal. The transducer is excited using a function generator to produce the Lamb wave. The transmitted signal is amplified using an AC signal amplifier. The received voltage by the piezoelectric sensor is also recorded by using an oscilloscope. The schematic of the pitch-catch system is shown in Figure 4-20.

The sensors can be used either as a bonded patch or embedded sensor. The initial received signal can be recorded as a base-line signal which can be continuously compared with the later revived signal to assess the properties of the structures. In fact, the received signal will be changed due to any change in the host structures which can be related to the properties and physical change of the structures. This section aims to study the feasibility of using the developed electrospun PVDF device as a receiver in a pitch-catch system to detect the Lamb wave. The second part of this section involves studying the several parameters such as the transmitted signal amplitude, frequency and the distance on the received signal by PVDF device. A pitch-catch system was set up in the lab to assess the efficiency of the flexible PVDF device for sensing application (Figure 4-21). Both transducer and piezoelectric sensor were attached to a wooden surface work table using a two-component adhesive, 3M's DP 460 Epoxy. A sinusoidal wave was generated by a function waveform generator and amplified by an amplifier to provide a lamb wave for sensing process.
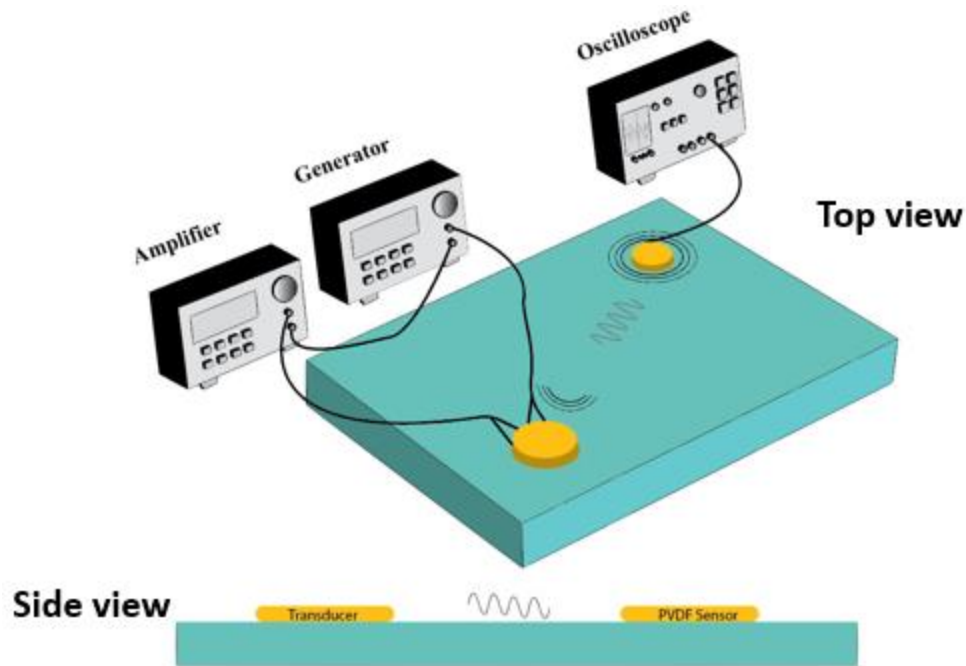
Figure 4-20- The schematic of the pitch-catch system

The waves are supposed to be received and detected by electrospun PVDF sensor. A digital oscilloscope was used to record the harmonic response of the PVDF sensors. In a pitch-catch setup, Lamb waves are generated by a piezoelectric actuator and received by a sensor at a certain distance. In fact, any defects or cracks results in a scattering of the Lamb wave which can be detected by the sensor. The sensor then receives the scattered waves, and the output voltage (amplitude) can be recorded. In order to quantify the damage, the scattered waveform is compared to the baseline state.

In order to evaluate the feasibility of PVDF sensor to receive the Lamb wave, a continuous 160 Vpp sinusoidal signal was generated by a function generator and amplified using an amplifier. The frequency of the transmitted signal was fixed at 2 kHz.

Figure 4-22 shows the transmitted signal along with the representative voltage-time plot as measured by electrospun PVDF device. It can be seen that the sensor successfully detected the propagated Lamb wave. The space between the actuator and sensor was kept constant at 15 cm. The maximum peak of 0.6 V can be detected by PVDF sensor.
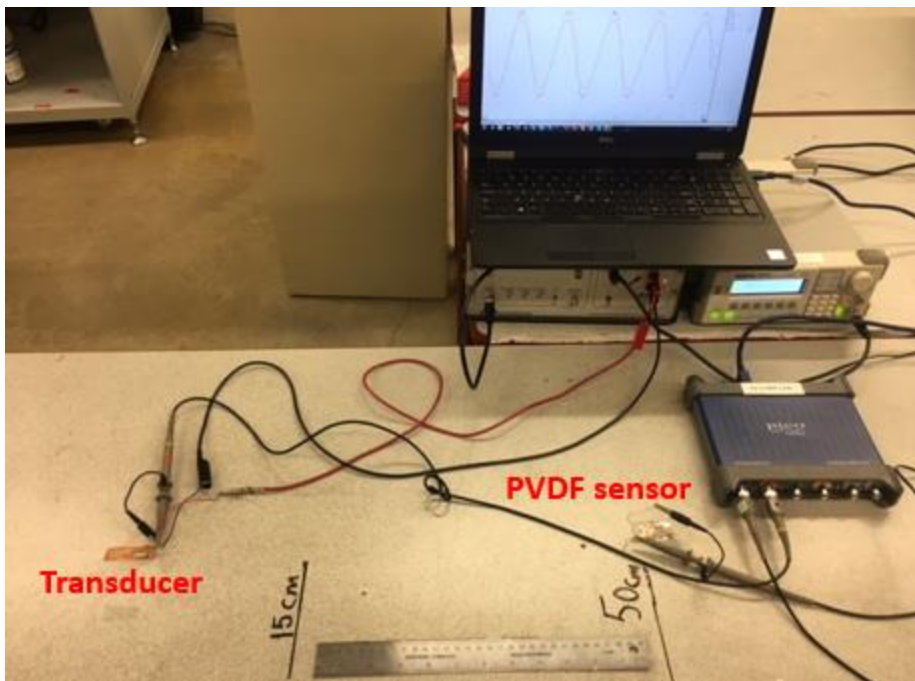
Figure 4-21- The experimental set up for evaluating the PVDF device for sensing applications.
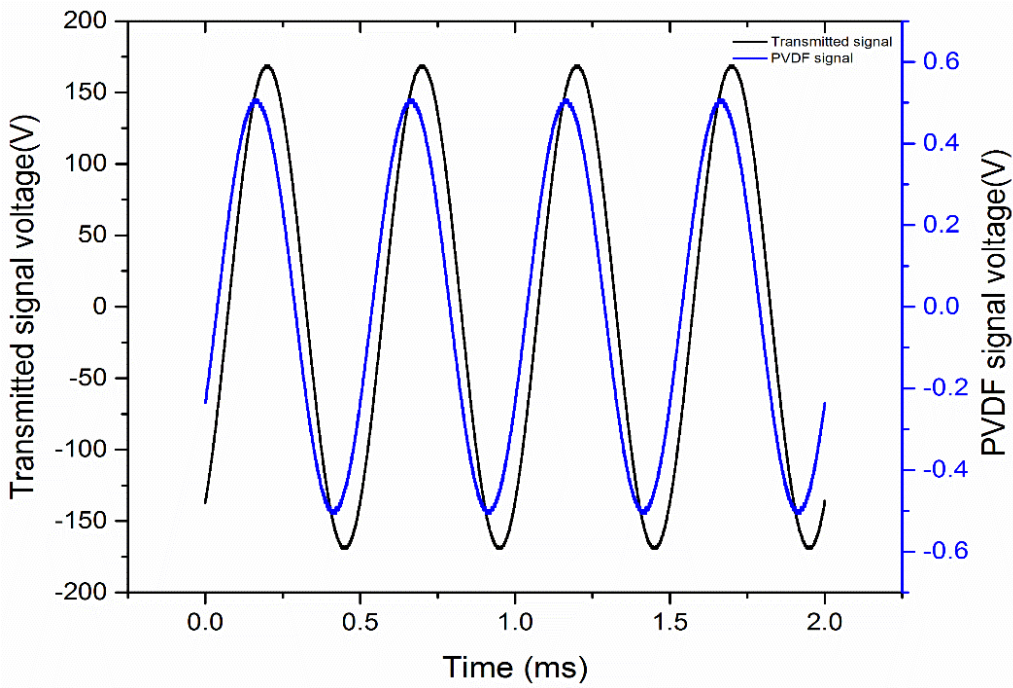
Figure 4-22- The generated Lamb wave and the received signal by PVDF sensor. The PVDF sensor successfully measured the propagated Lamb wave.

For the next experiment, a two-cycle 160 Vpp sinusoidal signal was generated and amplified using an amplifier. The frequency of the signal was fixed at 2 kHz. This signal was

pulsed every 10 ms to actuate the piezoelectric transducer for generating the Lamb wave. This experiment was conducted to evaluate the efficiency of PVDF sensor in detecting the multiple responses assigned to the same signal step. Also, a time delay in generated pulse was considered to make sure the previous Lamb wave is already attenuated so that it doesn't interfere the next cycle of the pulse signal. The PVDF sensor was connected to an oscilloscope for data acquisition. As can be seen in Figure 4-23, the PVDF sensor was found to be effective in detecting the pulse signal of generated Lamb wave.
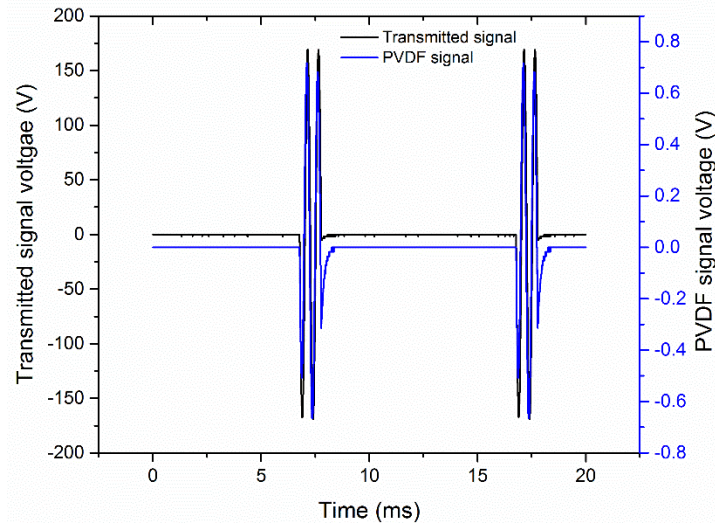
Figure 4-23- The generated pulse Lamb wave and the received signal by PVDF sensor.

The efficiency of the PVDF sensor to detect the signal type other than sinusoidal wave was also studied. In this scope, two different types of the Lamb wave including the square, and ramp were generated using the PZT transducers. Figure 4-24 and Figure 4-25 shows the transmitted signal along with the received signal voltage-time plot as measured by electrospun PVDF device. The transmitted signal with the amplitude of 160 Vpp at the frequency of 2 kHz was produced. As can be seen, the PVDF device can detect the square and ramp types of the transmitted signal. Up to now, the transmitted signal was actuated with a fixed amplitude and frequency. However, the properties of the transmitted signal might affect the received signal and the efficiency of the PVDF sensor to detect the signal. Therefore, a series of experiments were executed to evaluate the effect of several parameters of the transmitted signal such as amplitude and frequency on the received signal.
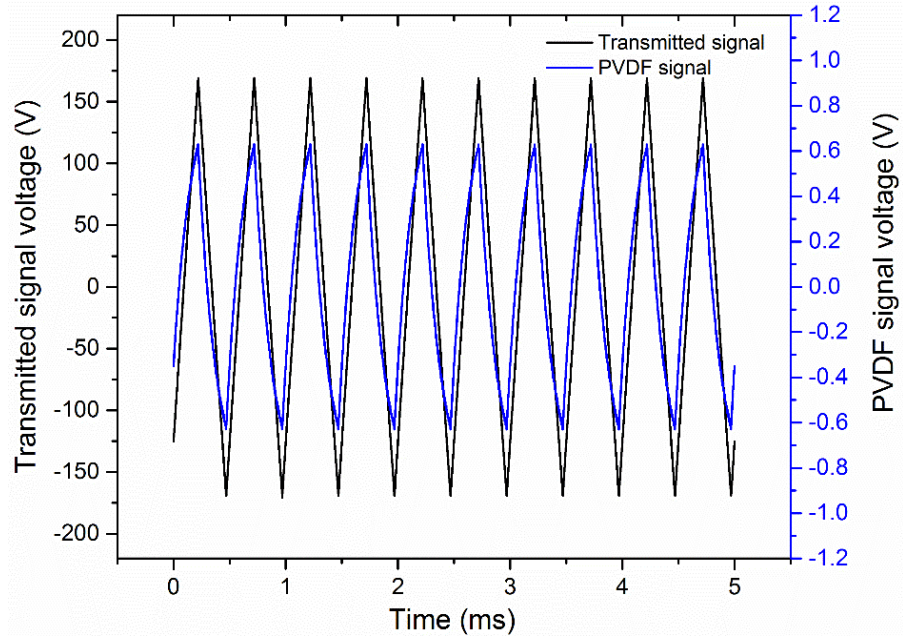
Figure 4-24- The transmitted ramp Lamb wave at the frequency of 2 kHz (160 Vpp) and the received signal by PVDF sensor.
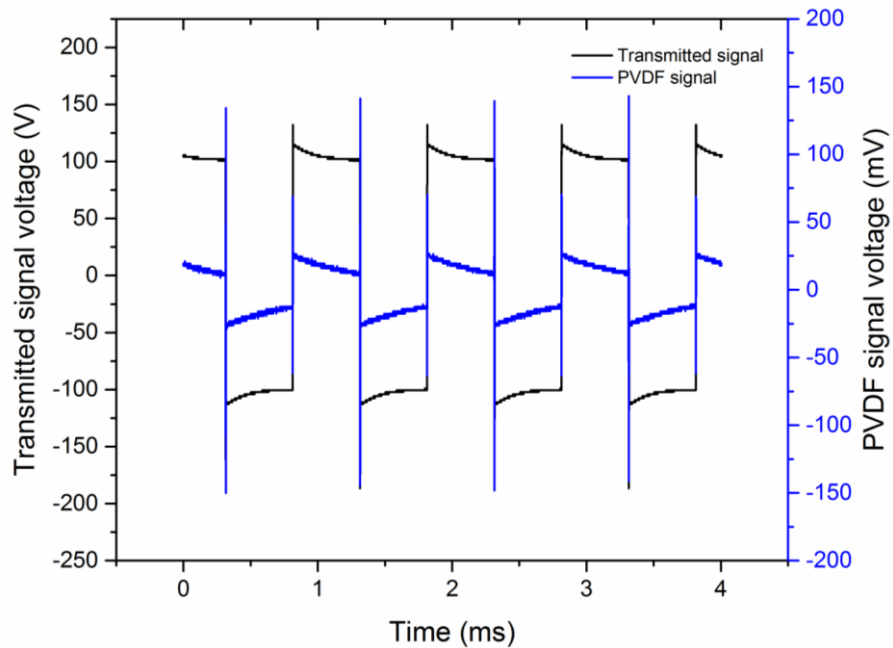
Figure 4-25- The transmitted square Lamb wave at the frequency of 2 kHz (160 Vpp) and the received signal by PVDF.

In addition, the effect of the transmitter-receiver distance was considered to determine the degree of the transmitted signal's attenuation. The sinusoidal Lamb wave signal was used for all the series of the experiments in this section. The outcome of this experiments can assist in

determining the most effective parameters for enhancing the efficiency of the PVDF sensor. Also, the experiments can assess the efficiency of the PVDF sensor in a variety of sensing condition. For example, the variation of the transmitted signal's frequency and amplitude can simulate different sensing conditions. The frequency of the transmitted signal varied from a very low frequency (<100 Hz), to the high range frequency (>100 kHz). Also, the amplitude of the transmitted signal varied from 40 Vpp to 200 Vpp. The effect of the amplitude and frequency of the transmitted signal was evaluated at three different distances of 15 cm, 50 cm, and 100 cm.

In order to compare the efficiency of the PVDF sensor at different active sensing situation, a relative parameter is defined as follow:

$$R/T(\%) = \frac{\text{The amplitude of the transmitted signal}}{\text{The amplitude of the recieved signal}} \qquad (4-2)$$

In fact, the R/T can be an indication of the efficiency of the PVDF sensor in detecting the generated signal by the transducer.

The analysis of the parameters on the PVDF sensor efficiency was conducted in different steps. At the first step, the effect of transmitted signal's amplitude on the received signal and R/T was assessed. In this experiment, the transducer was attached to the surface using the same procedure as previously explained in this section. The PVDF sensor was placed at three different distances away from the transducers including 15 cm, 50 cm, and 100 cm. The amplitude of the transmitted signal varied from 40 Vpp to 200 Vpp, while the frequency of the transmitted signal was fixed at 2 kHz.

Figure 4-26 shows the variation of the R/T and the PVDF sensor voltage over the range of the amplitude of the transmitted signal. The peak voltage of the PVDF sensor was recorded at 100 cm away from the transducer. As can be seen, the increase in the amplitude of the transmitted signal leads to an increase in the voltage of the PVDF sensor. Although the value of the received signal is influenced by the amplitude, no significant change can be observed in R/T value by changing the amplitude.

The efficiency of PVDF sensor was also assessed to detect the Lamb wave at different distances. In this scope, the distance between the sensor and actuator was varied by adjusting the position of electrospun PVDF sensor from the transducer. The effect of the transmitted signal amplitude on R/T value at 15 cm, 50 cm, and 100 cm is shown in Figure 4-27. As can be seen,

almost the same value of R/T was obtained over the wide range of amplitude at all distances. The results indicated that the efficiency of the PVDF sensor in detecting the signal is not sensitive to the amplitude of the transmitted signal.
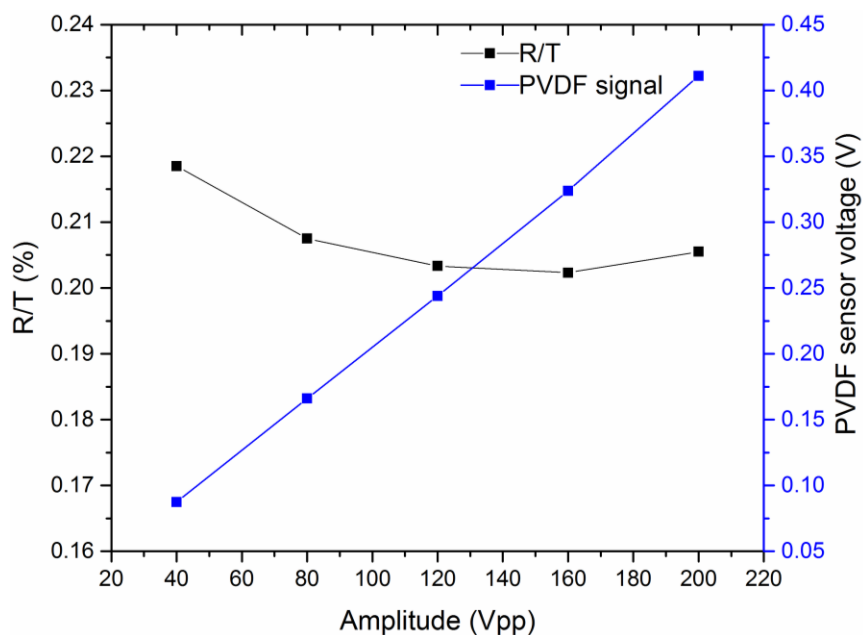
Figure 4-26- The variation of the R/T and the PVDF sensor voltage over the range of the amplitude of the transmitted signal at 100 cm.
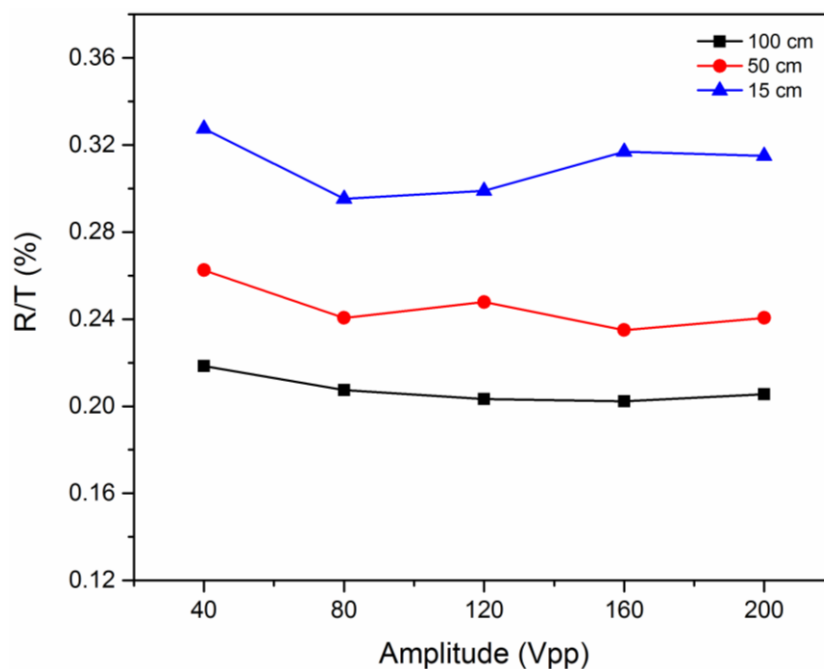
Figure 4-27- The effect of the transmitted signal amplitude on R/T value at 15 cm, 50 cm, and 100 cm.

Figure 4-28 shows the variation of the PVDF signal voltage over the three distances of 15 cm, 50 cm, and 100 cm as a function of the transmitted signal's amplitude. For each amplitude, the maximum voltage peak voltage by PVDF sensor was recorded. The results indicate that the received signal voltage by PVDF increased by increasing the amplitude regardless of the distance between the transducers and the PVDF sensor. When the amplitude increased from 40 Vpp to 200 Vpp, the voltage peak of the PVDF sensor increased by 3.8 times at 15 cm away from the transducer, while the rate of the increase in PVDF signal voltage was 3.6 and 3.7 times at 50 cm and 100 cm distance, respectively. The results indicate that the effect of the transmitted signal's amplitude on the received signal by PVDF device is less pronounced at the longer distance. The attenuation of the amplitude of the transmitted signal over the distance can also be observed at a certain amplitude in Figure 4-28. At each distance, the highest voltage peak was recorded at the amplitude of 200 Vpp. For example, the highest voltage peak of the PVDF sensor at the distance of 100 cm was 0.41 V which is almost 14 % and 34 % lower than the maximum voltage peak at the distance of 50 cm and 15 cm, respectively. However, the lowest voltage peak at the distance of 100 cm was 0.087 V which is 17 % and 33 % lower than the obtained voltage peak at the distance of 50 cm and 15 cm, respectively. The results imply that the transmitted signal's amplitude has an insignificant effect on the attenuation rate of the transmitted signal over the distance. Figure 4-29 summarizes the obtained R/T values over the three distances of 15 cm, 50 cm, and 100 cm as a function of the transmitted signal's amplitude. As shown, the R/T values drop as the distance increased. When the signal is transmitted at the lowest amplitude (40 Vpp), the highest R/T value at the distance of 100 cm was 0.21 which is 16 % and 33 % lower than the R/T ratio at the distance of 50 and 15 cm, respectively. In this case, the drop rate in R/T is 0.3% per cm. However, the signal is transmitted at the lowest amplitude (200 Vpp), the R/T value was dropped by 16 % and 33 % which gives almost the same value of drop rate (0.3% per cm). These results indicate that the amplitude of the transmitted signal does not affect the R/T value. It means that the efficiency of the PVDF sensor in detecting the Lamb wave signal is not affected by the amplitude of the transmitted signal. This effect can be clearly seen in Figure 4-27, where the results exhibit almost the same range of R/T value at a certain signal amplitude, regardless of the distance between the PVDF sensor and the transducer. At a certain distance, the standard deviation of the R/T value for all the signal amplitude was calculated to assess the effect of the amplitude's signal on the efficiency of the PVDF sensor. The standard deviation of R/T value at 100 cm was found to be

0.0065 which is 38 % and 52 % lower than the standard deviation at the distance of 50 cm and 15 cm, respectively. The results clearly indicate that the effect of the transmitted signal's amplitude on the efficiency of the PVDF device is less pronounced at the higher distance away from the transducer. The results are in agreement with the results of the PVDF signal voltage over the distance.
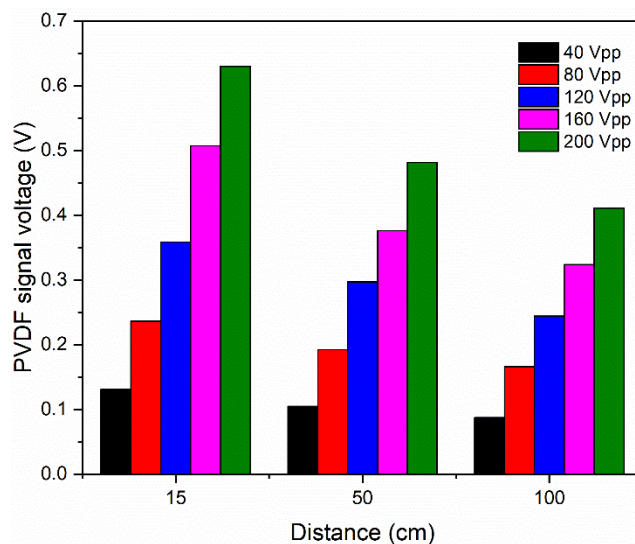
Figure 4-28- variation of PVDF signal voltage over the three distances of 15 cm, 50 cm, and 100 cm as function of the transmitted signal's amplitude
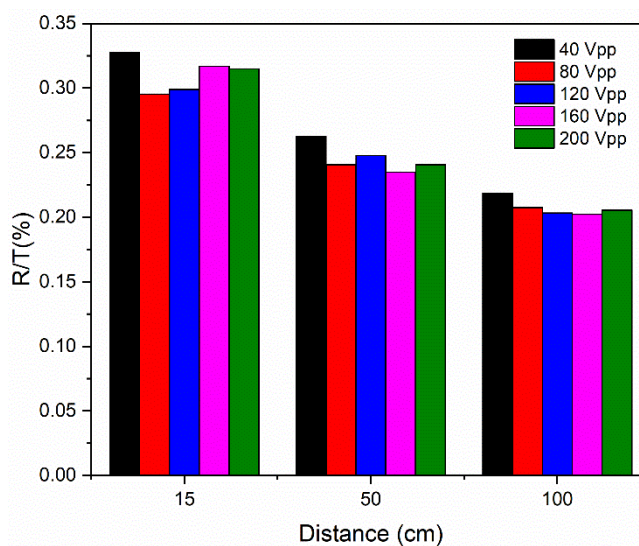
Figure 4-29- variation of R/T over the three distances of 15 cm, 50 cm, and 100 cm as function of the transmitted signal's amplitude

According to the obtained results, one can conclude that the amplitude of the transmitted signal doesn't affect the efficiency of the PVDF sensor in detecting the transmitted signal, while the efficiency of the PVDF sensor to detect the transmitted signal is highly affected by the distance between the transducer and receiver.

The second part of the experiment involves evaluating the efficiency of PVDF sensor for detecting the signal for the wide range of frequency. In this scope, the amplitude of the transmitted signal was fixed at 160 Vpp, while the frequency varied from 5 Hz to 500 kHz. The received voltage by PVDF was recorded at three distances of 15 cm, 50 cm and 100 cm away from the transducer. Figure 4-30 shows the PVDF signal voltage and the R/T value at 15 cm away from the transducer over a wide frequency range. As can be seen, both PVDF voltage signal and R/T curves follow almost the same trend. As the frequency is increased up to 1 kHz, R/T value is shown to increase sharply. The same level of R/T value was obtained in the frequency range of 1-100 kHz, while an abrupt decrease in R/T value can be observed for the frequency over 100 kHz. The effect can be better seen in the 3D curve of R/T as a function of the amplitude and frequency in Figure 4-31. When the PVDF sensor was placed at 15 cm away from the transducer, the lowest R/T value was 0.022 for at the frequency of 50 Hz. This value was 93 % lower than the maximum R/T value at the frequency of 100 kHz. The difference between the maximum and minimum of R/T was 93 % and 95 % for the distance of 50 and 100 cm, respectively. The results indicate almost the same rate of the increase in R/T value regardless of the distance between the transducer and the PVDF device.

Figure 4-32 shows the variation of R/T value over the frequency range as a function of the distance. As shown as the distance increases the R/T value drops, regardless of the frequency range. At the frequency of 50 Hz, the R/T value was 0.012 at 100 cm away from the transducer which is 16% and 45 % lower than the R/T ratio at the distance of 50 and 15 cm, respectively. However, the frequency of 100 kHz, the R/T value was 0.22 transducer which is 15 % and 21 % lower than the R/T ratio at the distance of 50 and 15 cm, respectively. Therefore, the effect of the distance on the efficiency of the sensor is more pronounced the low-frequency range. The results indicate that the PVDF device is less efficient in detecting the transmitted signal either at a low-frequency range (<1 kHz) or the higher range of frequency (> 100 kHz). One can note that an optimized range of the frequency needs to be determined to maximize the efficiency of the PVDF device in detecting the transmitted signal.
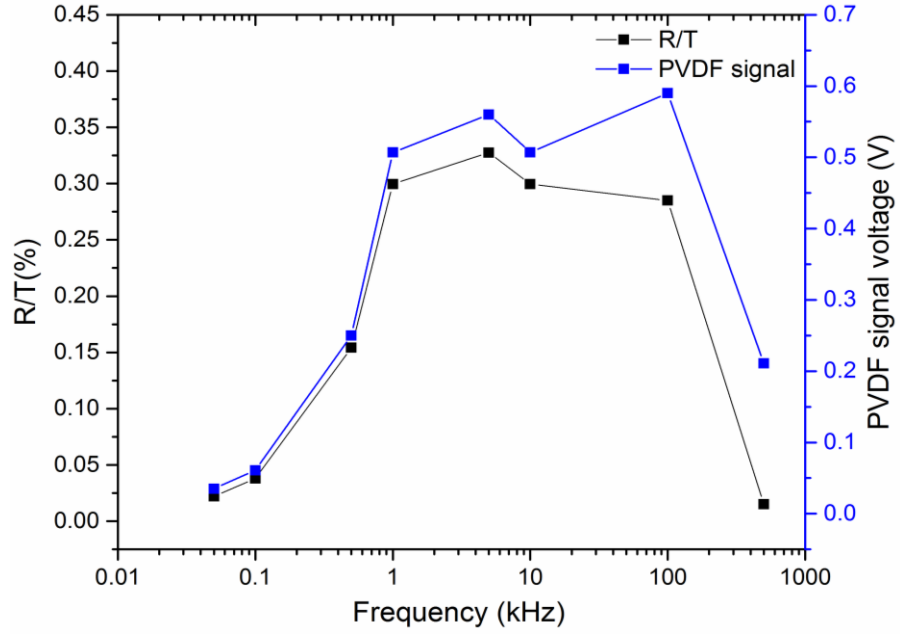
Figure 4-30-The PVDF signal voltage and the R/T value over the frequency range.
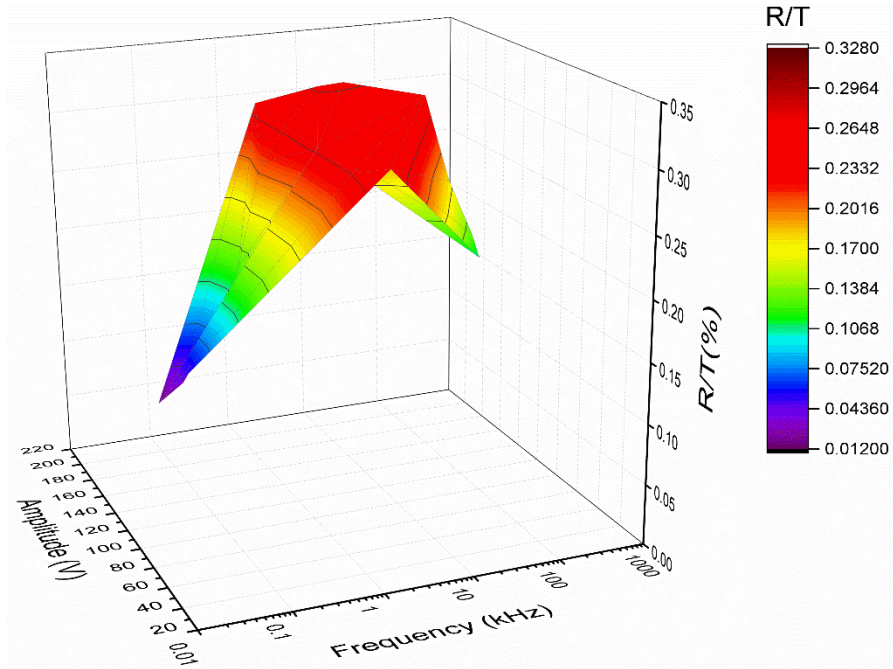
Figure 4-31- The 3D curve of R/T as a function of the amplitude and frequency.
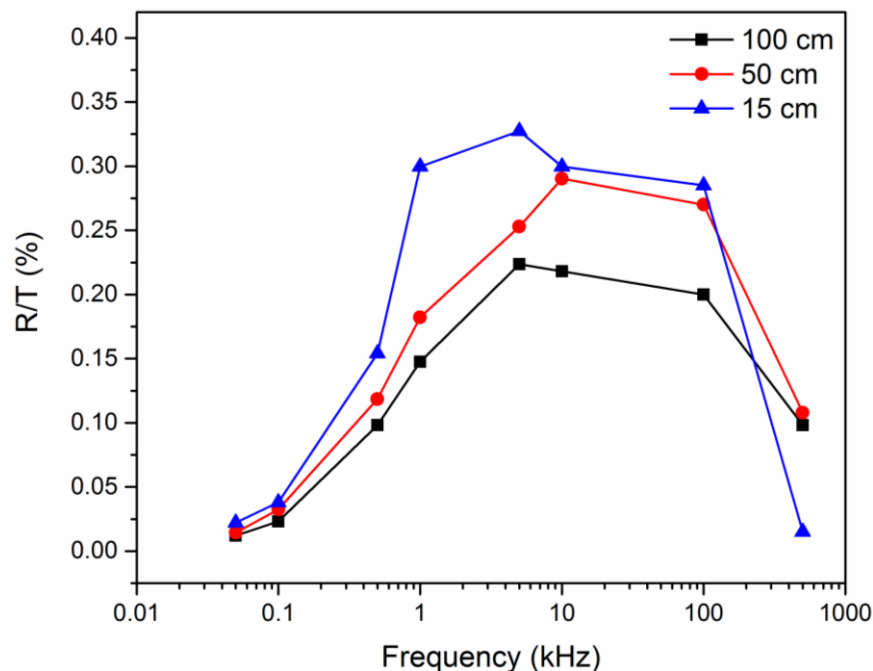
Figure 4-32- the variation of R/T value over the frequency range as a function of the distance.

As shown above, a range of 1 kHz to 100 kHz can be considered as an optimized range to enhance the efficiency of the PVDF sensor. This range is considered as an acoustic range. Hence, a more experimental was planned to evaluate the feasibility of the PVDF sensor to be used as an acoustic sensor.

4.6. Acoustic application:

The damage and deterioration are gaining significance in preventing the premature failure of structures such as offshore, platforms, dams, bridges, and underground buildings. A phenomenon associated with cracking has been emphasized by maintaining the structure both for safety and economic considerations. Among the techniques applied to detect cracking, acoustic emission (AE) system along with lead zirconate titanate (PZT) made transducers is now widely accepted and used in the field of civil engineering. The other piezoelectric materials including the single crystal PMNPT, PVDF, LiNbO$_3$, and ZnO are emerging as an appealing alternative to the classically used PZT and makes them as an exceptional candidate for sensing applications.

The previous results (section 4.4.1) proved the efficiency of the PVDF device in detecting the transmitted signal for a wide range of 1 kHz to 100 kHz. The results suggest of using this sensor for acoustic emission as a passive system and in the echo-pulse system as active testing in health monitoring of the structures. In this scope, a series of the experiments were conducted aiming to

evaluate the feasibility of the PVDF device to be used as an acoustic sensor. The feasibility of the PVDF device in detecting the acoustic emission wave was evaluated on cement paste beam. In this scope, a hammer has been used to generate acoustic waves nanofibers by periodic striking on the surface of a concrete beam. The viability of using PVDF sensor to detect the signal was evaluated by recording the voltage output using an oscilloscope. Figure 4-33 shows the experimental setup for the acoustic emission test on cement paste beam. It should be noted that the higher impact energy increases the voltage response measured by the PVDF sensor. Therefore, a digital sound meter was used to control the generated sound by a hammer. Figure 4-34 shows the voltage-time history responses of electrospun PVDF device mounted on the same substrate in which the peaks of positive and negative voltage outputs are recorded.
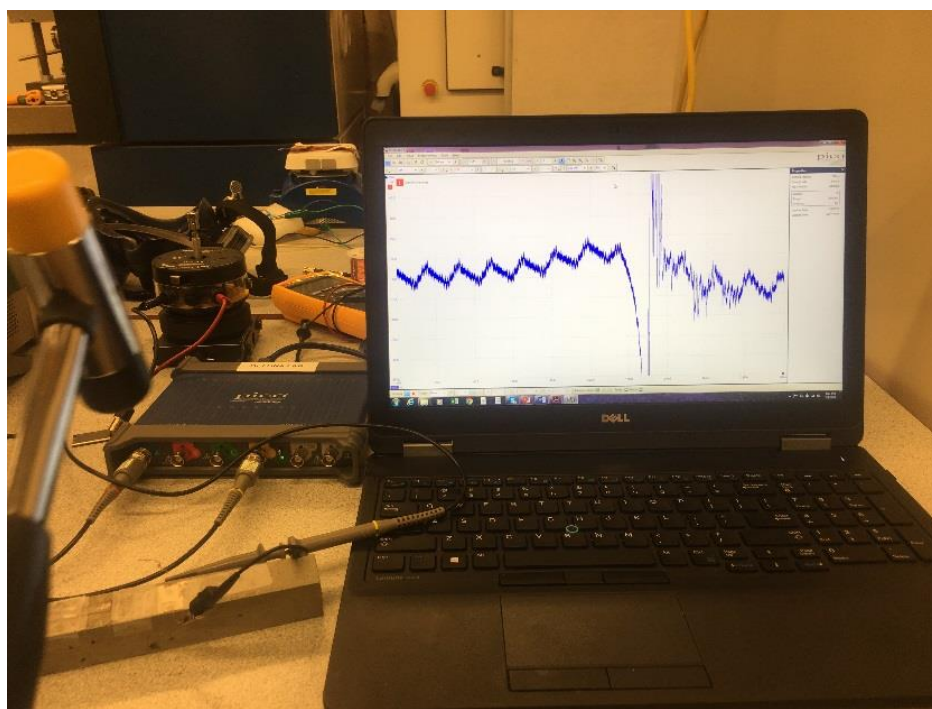
Figure 4-33- The experimental setup for the acoustic emission test.

The sound level of 86-89 dB was generated by each impact force. The generated surface acoustic waves have been monitored and detected using the electrospun PVDF device. These results clearly indicate that the sensor can detect different magnitudes of surface acoustic waves propagating on the surface. The higher of the impact energy applied to the concrete, the higher the voltage generated by electrospun PVDF AE sensor. During the experiment, the voltage reached ~100 mV and disappeared quickly due to the low power generated by the electrospun PVDF sensor.
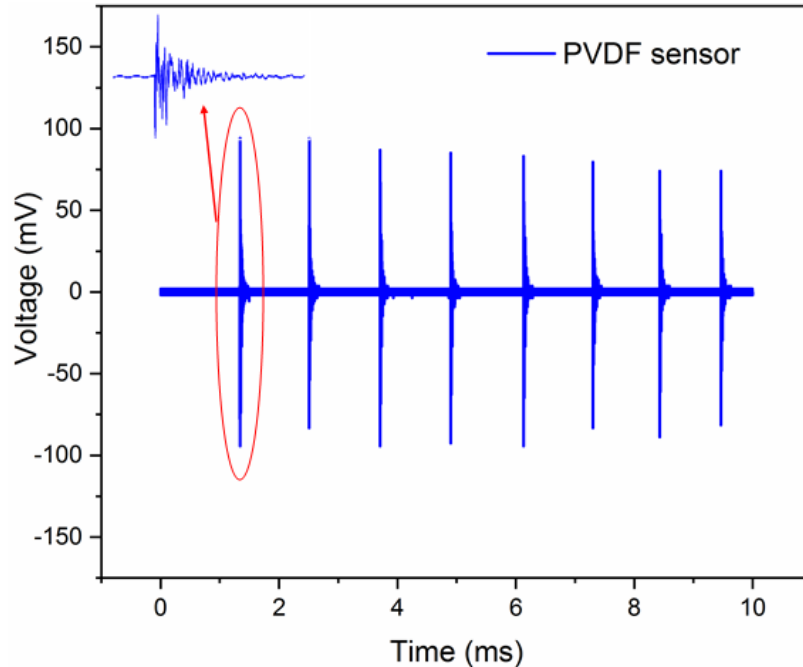
Figure 4-34-The voltage generation as a result of the surface waves induced by the periodic striking of a grounded steel bar on the composite substrate.

The voltage output reached up to 100 mV which is to be comparable to previous research results [146]. Chen et al. [146] developed an electrospun flexible AE sensor based on lead zirconate titanate (PZT) nanofiber composite membrane. An impact strike test was used to evaluate the efficiency of the PZT nanofiber to detect the acoustic waves. It was found that the output voltage can reached up to 100 mV in response to the simulated acoustic emission generated by the periodic impacts of a grounded steel bar. In summary, the PVDF sensor exhibits promising potential for both active and passive health monitoring system. The results indicate that the PVDF sensor can detect the generated Lamb wave which enables this device to be used to characterize the properties of the structural element. Also, the detection of the crack and structural defects can be determined using the pitch-catch method. The feasibility of using PVDF device as an acoustic sensor was also proved by conducting experiments on a cement paste beam. The results prove that the PVDF sensor can detect the acoustic emission wave.

CHAPTER 5.   CONCLUSION

This thesis aimed to design, fabricate and test a high efficient electrospun PVDF nanofiber for the energy harvesting and sensing application in civil infrastructure. The process-structure-property relations of electrospun PVDF nanofiber has been systematically studied during the course of my thesis work. A reliable RSM model was developed that enables accurate prediction of PVDF structure properties, particularly morphological and a fraction of the β-phase content. The model was further used to assess the effect of each individual electrospinning process parameters as well as the combined effects of different parameters on the electrospun PVDF properties. A numerical optimization was conducted to achieve a bead-free PVDF nanofiber with the maximum fraction of the β-phase. The RSM model was established which provides a thorough examination of PVDF nanofiber over the selected range of the electrospinning process parameters. The high values of coefficients of multiple determinations (R^2) showed the accuracy of the model to predict the characteristics of PVDF nanofiber in terms of both morphological and fraction of the β-phase content. The ANOVA results also confirmed that the inclusions of all model parameters are statistically significant based on very low P-value.

The results indicate that the higher concentration led to larger nanofiber size due to the higher solution viscosity and stronger intermolecular interactions. It is interesting to point out that, for a constant electrical field and flow rate, the higher DMF/acetone ratio led to finer fiber size, as higher acetone content increases the evaporation rate. The results show that the number of beads was reduced drastically for the solution with the concentration above 25 %. However, the high concentration solution itself doesn't necessarily result in a beads-free nanofiber. The increase in DMF/acetone ratio results in nanofiber characterized by more beads which might be due to the incomplete solvent evaporation. The fraction of β-phase is considerably affected by evaporation rate so that the high concentration of PVDF and DMF/acetone decreases the evaporation rate of the solution resulting in a formation of a high fraction β-phase content. A numerical optimization was also conducted to achieve a bead-free PVDF nanofiber with the maximum fraction of the β-phase. It was found that the electrospinning method is very effective to promote the β-phase formation in PVDF nanofiber. In fact, electrospun PVDF nanofibers were experienced high electrical field and mechanical stretching during the fabrication which eliminates a need for the post-treatment process.

This study proposes a core-shell structured PVDF-graphene oxide (GO) nanofiber composite, in which the polar phase content and piezoelectric properties are considerably improved. The results indicate that only 0.2 wt. % of GO is enough to nucleate most of the PVDF polymer chain. It was found that the β-phase content in core-shell structured PVDF-GO nanofiber composite can reach up to 92 % for which is 23% and 73 % higher than the neat electrospun PVDF and spin coated PVDF, respectively. This suggests that the core-shell structure of PVDF-GO is effective in improving the phase transformation of α-phase to β-phase, even at a low content of GO. As an interior core-shell, the GO is solidified into nanofiber form which increases the number of heterogeneous nucleation sites to interact with the PVDF polymer chain. The d_{33} piezoelectric coefficient of PVDF-GO was found to be 61 pm/V which is almost two times higher than PVDF nanofiber. The enhancement of the piezoelectric coefficient can be attributed to the higher β-phase content which can induce a stronger displacement in the sample as a result of the applied electrical field. This might be because of the interaction between the π-bond in GO with the fluorine atoms and hydrogen atoms on adjacent carbon atoms in PVDF polymer chains. The alignment of atoms at two sides of the polymer chain not only induces the beta phase formation but also results in a formation of a net polarized dipole moment along the core-shell structure of PVDG-GO nanofiber.

The feasibility of using PVDF device for energy harvesting and sensing applications was assessed by conducting a series of experiments. According to the results, the optimized frequency range for the device was found to be 45 Hz. The results indicated that the voltage output starts to decay at a higher frequency which can be due to the insufficient time for the PVDF nanofiber to be recovered from the induced strain. The variation of the amplitude has a great influence on the voltage output of the piezoelectric device. The voltage output of the PVDF device is enhanced with increasing the amplitude due to the higher amount of induced strain. In fact, the amount of induced strain can be considered as the main source of the available mechanical energy which can be fed into the piezoelectric device to be converted to the electrical energy. The results clearly show that both frequency and amplitude can affect the voltage output of the piezoelectric device. The highest obtained voltage output can be obtained at the frequency range between 30-45 Hz. The sensing ability of the PVDF device was assessed in both active and passive situations. A pitch-catch system was set up in the lab to assess the efficiency of the flexible PVDF device for active sensing application. A series of experiments were conducted to evaluate the effect of several parameters of the transmitted signal such as amplitude and frequency on the received signal. The

effect of transducer-sensor distance was also considered to evaluate the attenuation of the transmitted signal. The PVDF sensor was found to be effective in detecting the pulsed and continuous generated Lamb wave. It was found that the efficiency of the PVDF sensor in detecting the signal is not sensitive to the amplitude of the transmitted signal. Also, the transmitted signal's amplitude has an insignificant effect on the attenuation rate of the transmitted signal over the distance. It means that the efficiency of the PVDF sensor in detecting the Lamb wave signal is not affected by the amplitude of the transmitted signal. However, the efficiency of the PVDF sensor to detect the transmitted signal is highly affected by the distance between the transducer and receiver. The results indicate that the PVDF device is less efficient in detecting the transmitted signal either at a low-frequency range (<1 kHz) or the higher range of frequency (> 100 kHz). The optimized frequency was found to be in the range of 1 kHz to 100 kHz to enhance the efficiency of the PVDF sensor. The efficiency of PVDF sensor for detecting the acoustic wave was also studied by hammer impact testing. These results clearly indicate that the sensor is able to detect different magnitudes of surface acoustic waves propagating on the surface. The higher of the impact energy applied to the concrete, the higher the voltage generated by electrospun PVDF AE sensor. The results of this thesis can assist in adopting the electrospun PVDF piezoelectric sensor in a variety of sensing and energy harvesting applications in civil engineering infrastructure.

REFERENCES

1. Wang, Z. L., Zhu, G., Yang, Y., Wang, S., & Pan, C. (2012). Progress in nanogenerators for portable electronics. *Materials Today, 15*(12), 532-543. doi: http://dx.doi.org/10.1016/S1369-7021(13)70011-7

2. Zhou, C., Ghods, A., Yunghans, K., Saravade, V., Patel, P., Jiang, X., Kucukgok, B., Lu, N., Ferguson, I. (2017). *ZnO for solar cell and thermoelectric applications.* Paper presented at the Oxide-based Materials and Devices VIII.

3. Ghafari, E., Jiang, X., & Lu, N. (2017). Surface morphology and beta-phase formation of single polyvinylidene fluoride (PVDF) composite nanofibers. *Advanced Composites and Hybrid Materials*. doi: 10.1007/s42114-017-0016-z

4. Liu, Z., Yi, X., Wang, J., Kang, J., Melton, A., Shi, Y., Lu, N., Wang, J., Li, J., Ferguson, I. (2012). Ferromagnetism and its stability in n-type Gd-doped GaN: First-principles calculation. *Applied Physics Letters, 100*(23), 232408.

5. Liu, Z., Yi, X., Yu, Z., Yuan, G., Liu, Y., Wang, J., Li, J., Lu, N., Ferguson, I., Zhang, Y. (2016). Corrigendum: Impurity Resonant States p-type Doping in Wide-Band-Gap Nitrides. *Scientific reports, 6*, 23950.

6. Hussain, B., Raja, M., Lu, N., Ferguson, I. (2013). *Applications and synthesis of zinc oxide: an emerging wide bandgap material.* Paper presented at the High Capacity Optical Networks and Enabling Technologies (HONET-CNS), 2013 10th International Conference on.

7. Kucukgok, B., Wang, B., Melton, AG., Lu, N., Ferguson, IT. (2014). Comparison of thermoelectric properties of GaN and ZnO samples. *physica status solidi (c), 11*(3- 4), 894-897.

8. Hussain, B., Kucukgok, B., Raja, MYA., Klein, Benjamin., Lu, N., Ferguson, IT. (2014). *Is ZnO as a universal semiconductor material an oxymoron?* Paper presented at the Oxide-based Materials and Devices V.

9. Feng, Y., Jiang, X., Ghafari, E., Kucukgok, B., Zhang, C., Ferguson, I., Lu, N. (2017). Metal oxides for thermoelectric power generation and beyond. *Advanced Composites and Hybrid Materials*, 1-13.

10. Ghafari, E., Ghahari, SA., Feng, Y., Severgnini, F., Lu, N. (2016). Effect of Zinc oxide and Al-Zinc oxide nanoparticles on the rheological properties of cement paste. *Composites Part B: Engineering, 105*, 160-166.

11. Ghafari, E., Severgnini, F., Ghahari, S., Feng, Y., Lee, Eu J., Zhang, C., Jiang, X., Lu, N., Guo, Z., Chen, Y. (2018). Thermoelectric Nanocomposite for Energy Harvesting. *Multifunctional Nanocomposites for Energy and Environmental Applications*, 173-202.

12. Ghafari, E., Witkoske, E., Liu, Y., Zhang, C., Jiang, X., Bukowski, A., Kucukgok, B., Lundstrom, M., Ferguson, IT., Lu, N. (2017). Waste energy harvesting using III-nitrides materials. *III-Nitride Materials, Devices and Nano-Structures*, 37.

13. Wang, Z., Song, J. (2006). Piezoelectric nanogenerators based on zinc oxide nanowire arrays. *Science, 312*(5771), 242-246.

14. Gu, L., Cui, Nuanyang., Cheng, Li., Xu, Qi., Bai, Suo., Yuan, Miaomiao., Wu, Weiwei., Liu, Jinmei., Zhao, Yong., Ma, Fei. (2012). Flexible fiber nanogenerator with 209 V output voltage directly powers a light-emitting diode. *Nano Letters, 13*(1), 91-94.

15. Zhang, G., Xu, Shiyou., Shi, Yong. (2011). Electromechanical coupling of lead zirconate titanate nanofibres. *IET Micro & Nano Letters, 6*(1), 59-61.
16. Song, G., Gu, H., & Li, H. (2004). Application of the piezoelectric materials for health monitoring in civil engineering: an overview *Engineering, Construction, and Operations in Challenging Environments: Earth and Space 2004* (pp. 680-687).
17. Fang, J., Wang, Xungai., Lin, Tong. (2011). Electrical power generator from randomly oriented electrospun poly (vinylidene fluoride) nanofibre membranes. *Journal of Materials Chemistry, 21*(30), 11088-11091.
18. Chang, C., Tran, Van H., Wang, Junbo., Fuh, Yiin-Kuen., Lin, Liwei. (2010). Direct-write piezoelectric polymeric nanogenerator with high energy conversion efficiency. *Nano Letters, 10*(2), 726-731.
19. Bauer, S., & Bauer, F. (2008). Piezoelectric polymers and their applications. *Piezoelectricity: evolution and future of a technology, 114*, 157-180.
20. Xu, J., Dapino, M., Gallego-Perez, D., & Hansford, D. (2009). Microphone based on polyvinylidene fluoride (PVDF) micro-pillars and patterned electrodes. *Sensors and Actuators A: Physical, 153*(1), 24-32.
21. De Rosa, I. M., & Sarasini, F. (2010). Use of PVDF as acoustic emission sensor for in situ monitoring of mechanical behaviour of glass/epoxy laminates. *Polymer Testing, 29*(6), 749-758.
22. Li, B., Xu, C., Zheng, J., & Xu, C. (2014). Sensitivity of pressure sensors enhanced by doping silver nanowires. *Sensors, 14*(6), 9889-9899.
23. Hosseini, M., & Makhlouf, A. S. H. (2016). *Industrial Applications for Intelligent Polymers and Coatings*: Springer.
24. Yu, H., Huang, T., Lu, M., Mao, M., Zhang, Q., & Wang, H. (2013). Enhanced power output of an electrospun PVDF/MWCNTs-based nanogenerator by tuning its conductivity. *Nanotechnology, 24*(40), 405401.
25. Lei, T., Yu, L., Zheng, G., Wang, L., Wu, D., & Sun, D. (2015). Electrospinning-induced preferred dipole orientation in PVDF fibers. *Journal of Materials Science, 50*(12), 4342-4347.
26. Mandal, D., Yoon, S., & Kim, K. J. (2011). Origin of Piezoelectricity in an Electrospun Poly (vinylidene fluoride- trifluoroethylene) Nanofiber Web- Based Nanogenerator and Nano- Pressure Sensor. *Macromolecular rapid communications, 32*(11), 831-837.
27. Lee, B.-S., Park, B., Yang, H.-S., Han, J. W., Choong, C., Bae, J., . . . Chung, U.-I. (2014). Effects of substrate on piezoelectricity of electrospun poly (vinylidene fluoride)-nanofiber-based energy generators. *ACS applied materials & interfaces, 6*(5), 3520-3527.
28. Hansen, B. J., Liu, Y., Yang, R., & Wang, Z. L. (2010). Hybrid nanogenerator for concurrently harvesting biomechanical and biochemical energy. *ACS nano, 4*(7), 3647-3652.
29. Laxminarayana, K., & Jalili, N. (2005). Functional nanotube-based textiles: pathway to next generation fabrics with enhanced sensing capabilities. *Textile Research Journal, 75*(9), 670-680.
30. Ahn, Y., Lim, J. Y., Hong, S. M., Lee, J., Ha, J., Choi, H. J., & Seo, Y. (2013). Enhanced piezoelectric properties of electrospun poly (vinylidene fluoride)/multiwalled carbon nanotube composites due to high β-phase formation in poly (vinylidene fluoride). *The Journal of Physical Chemistry C, 117*(22), 11791-11799.

31.   Chang, J., & Lin, L. (2011). *Large array electrospun PVDF nanogenerators on a flexible substrate.* Paper presented at the Solid-State Sensors, Actuators and Microsystems Conference (TRANSDUCERS), 2011 16th International.

32.   Montgomery, D. C. (2005). Design and Analysis of Experiments: Response surface method and designs. New Jersey.

33.   Ghafari, E., Costa, H., Júlio, E. (2013). *Development of Ultra High Performance Self Compacting Concrete.* Paper presented at the Proceedings of the Fifth North American Conference on the SCC Design and Use of Self-Consolidating Concrete, Chicago, USA.

34.   Ghafari, E., Hugo,C., Júlio, E. (2014). RSM-based model to predict the performance of self-compacting UHPC reinforced with hybrid steel micro-fibers. *Construction and Building Materials, 66*(0), 375-383. doi: http://dx.doi.org/10.1016/j.conbuildmat.2014.05.064

35.   Ghafari, E., Costa, H., Júlio, E. (2015). Statistical mixture design approach for eco-efficient UHPC. *Cement and Concrete Composites, 55*(0), 17-25. doi: http://dx.doi.org/10.1016/j.cemconcomp.2014.07.016

36.   Alyamac, K., Ghafari, E., Ince, R. (2017). Development of eco-efficient self-compacting concrete with waste marble powder using the response surface method. *Journal of Cleaner Production, 144*, 192-202.

37.   Bodkhe, S., Rajesh, P., Kamle, S., Verma, V. (2014). Beta-phase enhancement in polyvinylidene fluoride through filler addition: comparing cellulose with carbon nanotubes and clay. *Journal of Polymer Research, 21*(5), 434.

38.   Tichý, J., Erhart, J., Kittinger, E., & Prívratská, J. (2010). *Fundamentals of piezoelectric sensorics: mechanical, dielectric, and thermodynamical properties of piezoelectric materials*: Springer Science & Business Media.

39.   Safari, A., & Akdogan, E. K. (2008). *Piezoelectric and acoustic materials for transducer applications*: Springer Science & Business Media.

40.   Xu, S., Hansen, B. J., & Wang, Z. L. (2010). Piezoelectric-nanowire-enabled power source for driving wireless microelectronics. *1*, 93. doi: 10.1038/ncomms1098 http://dharmasastra.live.cf.private.springer.com/articles/ncomms1098#supplementary-information

41.   He, X., & Yao, K. (2006). Crystallization mechanism and piezoelectric properties of solution-derived ferroelectric poly (vinylidene fluoride) thin films. *Applied Physics Letters, 89*(11), 112909.

42.   Sharma, M., Srinivas, V., Madras, G., & Bose, S. (2016). Outstanding dielectric constant and piezoelectric coefficient in electrospun nanofiber mats of PVDF containing silver decorated multiwall carbon nanotubes: assessing through piezoresponse force microscopy. *RSC Advances, 6*(8), 6251-6258.

43.   Kim, D. M., Eom, C.-B., Nagarajan, V., Ouyang, J., Ramesh, R., Vaithyanathan, V., & Schlom, D. G. (2006). Thickness dependence of structural and piezoelectric properties of epitaxial Pb (Zr 0.52 Ti 0.48) O 3 films on Si and Sr Ti O 3 substrates. *Applied Physics Letters, 88*(14), 142904.

44.   Zhang, G. (2015). Piezoelectric properties and applications of PZT nanofibers.

45.   Broitman, E., Soomro, M. Y., Lu, J., Willander, M., & Hultman, L. (2013). Nanoscale piezoelectric response of ZnO nanowires measured using a nanoindentation technique. *Physical Chemistry Chemical Physics, 15*(26), 11113-11118.

46.   Zhao, M.-H., Wang, Z.-L., & Mao, S. X. (2004). Piezoelectric characterization of individual zinc oxide nanobelt probed by piezoresponse force microscope. *Nano Letters, 4*(4), 587-590.

47.   Blumenstein, N. J., Streb, F., Walheim, S., Schimmel, T., Burghard, Z., & Bill, J. (2017). Template-controlled piezoactivity of ZnO thin films grown via a bioinspired approach. *Beilstein journal of nanotechnology, 8*, 296.

48.   Li, M., Wondergem, H., Spijkman, M., Asadi, K., Katsouras, I., Blom, P., De Leeuw, D. (2013). Revisiting the [delta]-phase of poly (vinylidene fluoride) for solution-processed ferroelectric thin films. *Nature materials, 12*(5), 433.

49.   Aqeel, S. M., Huanga, Z., Walton, J., Baker, C., Falkner, D., Liu, Z., Wang, Z. (2017). Advanced functional Polyvinylidene fluoride (PVDF)/Polyacrilonitrile (PAN) organic semiconductor assisted by aligned nanocarbon toward energy storage and conversion. *Advanced Composites Science*.

50.   Guo, H.-F., Li, Zhen-Sheng., Dong, Shi-Wu., Chen, Wei-Jun., Deng, Ling., Wang, Yu-Fei., Ying, Da-Jun. (2012). Piezoelectric PU/PVDF electrospun scaffolds for wound healing applications. *Colloids and Surfaces B: Biointerfaces, 96*, 29-36.

51.   Cozza, E., Monticelli, O., Marsano, E., Cebe, P. (2013). On the electrospinning of PVDF: influence of the experimental conditions on the nanofiber properties. *Polymer International, 62*(1), 41-48.

52.   Sencadas, V., Ribeiro, C., Bdikin, I., Kholkin, A., Lanceros- Mendez, S. (2012). Local piezoelectric response of single poly (vinylidene fluoride) electrospun fibers. *physica status solidi (a), 209*(12), 2605-2609.

53.   Damaraju, S., Wu, S., Jaffe, M., Arinzeh, T. (2013). Structural changes in PVDF fibers due to electrospinning and its effect on biological function. *Biomedical Materials, 8*(4), 045007.

54.   Bassiri-Gharb, N., Fujii, Ichiro., Hong, Eunki., Trolier-McKinstry, Susan., Taylor, David V., Damjanovic, Dragan. (2007). Domain wall contributions to the properties of piezoelectric thin films. *Journal of Electroceramics, 19*(1), 49-67.

55.   Ribeiro, C., Sencadas, V., Costa, C. M., Ribelles, J. L. G., & Lanceros-Méndez, S. (2011). Tailoring the morphology and crystallinity of poly (L-lactide acid) electrospun membranes. *Science and technology of advanced materials, 12*(1), 015001.

56.   Lee, Y., & Arinzeh, T. (2010). Electrospun Nanofibers for neural applications: CRC Press/Taylor and Francis: New York, NY, USA.

57.   Wang, H. B., Mullins, M. E., Cregg, J. M., Hurtado, A., Oudega, M., Trombley, M. T., & Gilbert, R. J. (2008). Creation of highly aligned electrospun poly-L-lactic acid fibers for nerve regeneration applications. *Journal of neural engineering, 6*(1), 016001.

58.   El-hadi, A. M., & Al-Jabri, F. Y. (2016). Influence of electrospinning parameters on fiber diameter and mechanical properties of poly (3-hydroxybutyrate)(PHB) and polyanilines (PANI) blends. *Polymers, 8*(3), 97.

59.   Pan, H., Li, L., Hu, L., & Cui, X. (2006). Continuous aligned polymer fibers produced by a modified electrospinning method. *Polymer, 47*(14), 4901-4904.

60.   Yin, Y., & Xiong, J. (2017). Effect of the Distribution of Fiber Orientation on the Mechanical Properties of Silk Fibroin/Polycaprolactone Nanofiber Mats. *Journal of Engineered Fabrics & Fibers (JEFF), 12*(3).

61.   Liu, Z., Pan, CT., Lin, LW., Li, HW., Ke, CA., Huang, JC., Wang, PS. (2013). *Mechanical properties of piezoelectric PVDF/MWCNT fibers prepared by flat/hollow cylindrical near-field electrospinning process.* Paper presented at the Nano/Micro Engineered and Molecular Systems (NEMS), 2013 8th IEEE International Conference on.

62.   Mokhtari, F., Latifi, M., & Shamshirsaz, M. (2016). Electrospinning/electrospray of polyvinylidene fluoride (PVDF): piezoelectric nanofibers. *The Journal of The Textile Institute, 107*(8), 1037-1055.

63.   Persano, L., Dagdeviren, C., Su, Y., Zhang, Y., Girardo, S., Pisignano, D., . . . Rogers, J. A. (2013). High performance piezoelectric devices based on aligned arrays of nanofibers of poly (vinylidenefluoride-co-trifluoroethylene). *Nature communications, 4*, 1633.

64.   Yee, W. A., Kong, J., Zhang, C., Liu, T., Kotaki, M., & Lu, X. (2012). Polymorphism of electrospun polyvinylidene difluoride/carbon nanotube (CNT) nanocomposites: Synergistic effects of CNT surface chemistry, extensional force and supercritical carbon dioxide treatment. *Polymer, 53*(22), 5097-5102.

65.   Wu, C. M., & Chou, M. H. (2016). Polymorphism, piezoelectricity and sound absorption of electrospun PVDF membranes with and without carbon nanotubes. *Composites Science and Technology, 127*, 127-133.

66.   Bhavanasi, V., Kumar, V., Parida, K., Wang, J., & Lee, P. S. (2015). Enhanced piezoelectric energy harvesting performance of flexible PVDF-TrFE bilayer films with graphene oxide. *ACS applied materials & interfaces, 8*(1), 521-529.

67.   Rahman, M. A., Lee, B.-C., Phan, D.-T., & Chung, G.-S. (2013). Fabrication and characterization of highly efficient flexible energy harvesters using PVDF–graphene nanocomposites. *Smart materials and Structures, 22*(8), 085017.

68.   Mokhtari, F., Shamshirsaz, M., Latifi, M. (2016). Investigation of β phase formation in piezoelectric response of electrospun polyvinylidene fluoride nanofibers: LiCl additive and increasing fibers tension. *Polymer Engineering & Science, 56*(1), 61-70.

69.   Fashandi, H., Abolhasani, M. M., Sandoghdar, P., Zohdi, N., Li, Q., & Naebe, M. (2016). Morphological changes towards enhancing piezoelectric properties of PVDF electrical generators using cellulose nanocrystals. *Cellulose, 23*(6), 3625-3637.

70.   Liu, Y.-L., Li, Y., Xu, J.-T., & Fan, Z.-Q. (2010). Cooperative effect of electrospinning and nanoclay on formation of polar crystalline phases in poly (vinylidene fluoride). *ACS applied materials & interfaces, 2*(6), 1759-1768.

71.   Bafqi, M. S. S., Bagherzadeh, R., & Latifi, M. (2015). Fabrication of composite PVDF-ZnO nanofiber mats by electrospinning for energy scavenging application with enhanced efficiency. *Journal of Polymer Research, 22*(7), 130.

72.   Nunes-Pereira, J., Sencadas, V., Correia, V., Rocha, J. G., & Lanceros-Méndez, S. (2013). Energy harvesting performance of piezoelectric electrospun polymer fibers and polymer/ceramic composites. *Sensors and Actuators A: Physical, 196*, 55-62.

73.   Lee, C., Wood, D., Edmondson, D., Yao, D., Erickson, A. E., Tsao, C. T., . . . Zhang, M. (2016). Electrospun uniaxially-aligned composite nanofibers as highly-efficient piezoelectric material. *Ceramics International, 42*(2), 2734-2740.

74.   Zeng, W., Tao, X.-M., Chen, S., Shang, S., Chan, H. L. W., & Choy, S. H. (2013). Highly durable all-fiber nanogenerator for mechanical energy harvesting. *Energy & Environmental Science, 6*(9), 2631-2638.

75. Yun, J. S., Park, C. K., Jeong, Y. H., Cho, J. H., Paik, J.-H., Yoon, S. H., & Hwang, K.-R. (2016). The fabrication and characterization of piezoelectric PZT/PVDF electrospun nanofiber composites. *Nanomaterials and Nanotechnology, 6*, 20.

76. Ou, Z., Liu, ZH., Pan, CT., Lin, LW., Chen, YJ., Lai, HW. (2012). *Study on piezoelectric properties of near-field electrospinning PVDF/MWCNT nano-fiber.* Paper presented at the Nano/Micro Engineered and Molecular Systems (NEMS), 2012 7th IEEE International Conference on.

77. Adhikary, P., Biswas, A., & Mandal, D. (2016). Improved sensitivity of wearable nanogenerators made of electrospun Eu3+ doped P (VDF-HFP)/graphene composite nanofibers for self-powered voice recognition. *Nanotechnology, 27*(49), 495501.

78. Im, J. Y., Kim, S., Choi, H. J., & Seo, Y. (2014). *Effect of Elongational Deformation on the B‐ Phase Formation of Poly (vinylidene Fluoride)/Multiwalled Carbon Nanotube Composites and Their Piezoelectric Properties.* Paper presented at the Macromolecular Symposia.

79. Wang, S.-H., Wan, Y., Sun, B., Liu, L.-Z., & Xu, W. (2014). Mechanical and electrical properties of electrospun PVDF/MWCNT ultrafine fibers using rotating collector. *Nanoscale research letters, 9*(1), 522. doi: 10.1186/1556-276x-9-522

80. Siddiqui, S., Kim, D.-I., Duy, L. T., Nguyen, M. T., Muhammad, S., Yoon, W.-S., & Lee, N.-E. (2015). High-performance flexible lead-free nanocomposite piezoelectric nanogenerator for biomechanical energy harvesting and storage. *Nano Energy, 15*(Supplement C), 177-185. doi: https://doi.org/10.1016/j.nanoen.2015.04.030

81. Wang, Z., Pan, X., He, Y., Hu, Y., Gu, H., & Wang, Y. (2015). Piezoelectric nanowires in energy harvesting applications. *Advances in Materials Science and Engineering, 2015*.

82. Wang, Y., Zheng, JM., Ren, GY., Zhang, PH., Xu, C.,. (2011). A flexible piezoelectric force sensor based on PVDF fabrics. *Smart materials and Structures, 20*(4), 045009.

83. Xin, Y., Qi, X., Tian, H., Guo, C., Li, X., Lin, J., & Wang, C. (2016). Full-fiber piezoelectric sensor by straight PVDF/nanoclay nanofibers. *Materials Letters, 164*, 136-139.

84. Pan, X., Wang, Z., Cao, Z., Zhang, S., He, Y., Zhang, Y., . . . Gu, H. (2016). A self-powered vibration sensor based on electrospun poly (vinylidene fluoride) nanofibres with enhanced piezoelectric response. *Smart materials and Structures, 25*(10), 105010.

85. Garain, S., Jana, S., Sinha, T. K., & Mandal, D. (2016). Design of in situ poled Ce3+-Doped electrospun PVDF/Graphene composite nanofibers for fabrication of nanopressure sensor and ultrasensitive acoustic nanogenerator. *ACS applied materials & interfaces, 8*(7), 4532-4540.

86. Lee, J. S., Shin, K.-Y., Cheong, O. J., Kim, J. H., & Jang, J. (2015). Highly sensitive and multifunctional tactile sensor using free-standing ZnO/PVDF thin film with graphene electrodes for pressure and temperature monitoring. *Scientific reports, 5*, 7887.

87. Rathod, V., Mahapatra, D. R., Jain, A., & Gayathri, A. (2010). Characterization of a large-area PVDF thin film for electro-mechanical and ultrasonic sensing applications. *Sensors and Actuators A: Physical, 163*(1), 164-171.

88. Gu, H., Lloyd, G. M., & Wang, M. L. (2005). *Interdigitated PVDF transducer for Lamb wave generation and reception.* Paper presented at the Smart Structures and Materials.

89. Meyers, F. N., Loh, K. J., Dodds, J. S., & Baltazar, A. (2013). Active sensing and damage detection using piezoelectric zinc oxide-based nanocomposites. *Nanotechnology, 24*(18), 185501.

90. Lang, C., Fang, J., Shao, H., Ding, X., & Lin, T. (2016). High-sensitivity acoustic sensors from nanofibre webs. *Nature communications, 7*.

91. Taylor, G. (1964). Disintegration of Water Drops in an Electric Field. *Proceedings of the Royal Society of London A: Mathematical, Physical and Engineering Sciences, 280*(1382), 383-397. doi: 10.1098/rspa.1964.0151

92. Ghafari, E., Feng, Y., Liu, Y., Ferguson, I., Lu, N. (2017). Investigating process-structure relations of ZnO nanofiber via electrospinning method. *Composites Part B: Engineering, 116*, 40-45.

93. Yarin, A. L., Koombhongse, S., & Reneker, D. H. (2001). Bending instability in electrospinning of nanofibers. *Journal of Applied Physics, 89*(5), 3018-3026. doi: doi:http://dx.doi.org/10.1063/1.1333035

94. Abolhasani, M. M., Shirvanimoghaddam, K., & Naebe, M. (2017). PVDF/graphene composite nanofibers with enhanced piezoelectric performance for development of robust nanogenerators. *Composites Science and Technology, 138*, 49-56.

95. Ghafari, E., Bandarabadi, M., Costa, H., Júlio, E. . (2012). *Design of UHPC using Artificial Neural Networks* Paper presented at the 10th International Symposium on Brittle Matrix Composites, Warsaw, Poland.

96. Ghafari, E., Bandarabadi, M., Costa, H., Júlio, E. (2015). Prediction of Fresh and Hardened State Properties of UHPC: Comparative Study of Statistical Mixture Design and an Artificial Neural Network Model. *Journal of Materials in Civil Engineering*.

97. Ghafari, E., Costa, H., Júlio, E. (2014). *New robust design approach for optmized sustainable UHPC.* Paper presented at the The Fourth International fib congress Mumbai.

98. Ghafari, E., Costa, H., Júlio, E, Portugal, A., Durães, L. (2014). The effect of nanosilica addition on flowability, strength and transport properties of ultra high performance concrete. *Materials & Design, 59*, 1-9.

99. Ghafari, E., Costa, H., Júlio, E. (2015). Critical review on eco-efficient ultra high performance concrete enhanced with nano-materials. *Construction and Building Materials, 101, Part 1*, 201-208. doi: http://dx.doi.org/10.1016/j.conbuildmat.2015.10.066

100. Ghafari, E., Arezoumandi, M., Costa, H., Júlio, E. (2015). Influence of nano-silica addition on durability of UHPC. *Construction and Building Materials, 94*, 181-188. doi: http://dx.doi.org/10.1016/j.conbuildmat.2015.07.009

101. Ghafari, E., Ghahari, S., Costa, H., Júlio, E., Portugal, A., Durães, L. (2016). Effect of supplementary cementitious materials on autogenous shrinkage of ultra-high performance concrete. *Construction and Building Materials, 127*, 43-48.

102. Ghafari, E., Costa, H., Júlio, E., Portugal, A., Durães, L. (2012). *Optimization of UHPC by adding nanomaterials.* Paper presented at the Proceedings of 3rd international symposium on ultra-high-performance concrete and nanotechnology for high performance construction materials. Kassel (Germany).

103. Esmaeeli, H. S., Farnam, Y., Haddock, J. E., Zavattieri, P. D., & Weiss, W. J. (2018). Numerical analysis of the freeze-thaw performance of cementitious composites that contain phase change material (PCM). *Materials & Design*.

104. Esmaeeli, H. S., Farnam, Y., Bentz, D. P., Zavattieri, P. D., & Weiss, W. J. (2017). Numerical simulation of the freeze–thaw behavior of mortar containing deicing salt solution. *Materials and structures, 50*(1), 96.

105. Miller, I., Albert, E., Spragg, R., Antico, F., Ashraf, W., Barrett, T., . . . Tian, Q. (2014). Determining the moisture content of pre-wetted lightweight aggregate: assessing the variability of the paper towel and centrifuge methods.

106. Antico, F., De la Varga, I., Esmaeeli, H., Nantung, T., Zavattieri, P., & Weiss, W. (2015). Using accelerated pavement testing to examine traffic opening criteria for concrete pavements. *Construction and Building Materials, 96*, 86-95.

107. Simon, M. J., Lagergren, E.S, Wathne, L.G. . (1999). *Optimizing High-Performance Concrete Mixtures Using Statistical Response Surface Methods.* Paper presented at the International Symposium on Utilization of High-Strength/High-Performance Concrete, Oslo, Norway.

108. Feys, D., Asghari, A., Ghafari, E., Hernandez, A. M. L., Van Der Vurst, F., & De Schutter, G. (2014). Influence of mixing procedure on robustness of self-consolidating concrete. *Center for Transportation Infrastructure and Safety*.

109. Ghafari, E., Feys, D., Khayat, K. (2016). Feasibility of using natural SCMs in concrete for infrastructure applications. *Construction and Building Materials, 127*, 724-732.

110. Ghafari, E., Baig, A., Nicoletta, K., Feys, D., Ferron, R.D., Khayat, K.H. (2014). Admixture Compatibility of Alternative Supplementary Cementitious Materials for Pavement and Structural Concrete: NUTC.

111. Ghafari, E., Costa, H., Júlio, E. . (2012). *Design of UHPFRC with enhanced ductility and flowability.* Paper presented at the 8 th Rilem conference on fiber reinforced concrete, Guimares ,Portugal.

112. Costa, L., Bretas, R., Gregorio, R. (2010). Effect of solution concentration on the electrospray/electrospinning transition and on the crystalline phase of PVDF. *Materials Sciences and Applications, 1*(04), 247.

113. Liu, Y., He, Ji- H., Yu, J., Zeng, H. (2008). Controlling numbers and sizes of beads in electrospun nanofibers. *Polymer international, 57*(4), 632-636.

114. Miyoshi, T., Toyohara, K., Minematsu, H. (2005). Preparation of ultrafine fibrous zein membranes via electrospinning. *Polymer international, 54*(8), 1187-1190.

115. Yuan, X., Zhang, Y., Dong, C., Sheng, J. (2004). Morphology of ultrafine polysulfone fibers prepared by electrospinning. *Polymer international, 53*(11), 1704-1710.

116. Yarin, A. (1993). *Free liquid jets and films: hydrodynamics and rheology*: Longman Publishing Group.

117. Entov, V., Shmaryan, LE. (1997). Numerical modeling of the capillary breakup of jets of polymeric liquids. *Fluid dynamics, 32*(5), 696-703.

118. Correia, D., Gonçalves, R., Ribeiro, C., Sencadas, V., Botelho, G., Ribelles, J., Lanceros-Méndez, S. (2014). Electrosprayed poly (vinylidene fluoride) microparticles for tissue engineering applications. *RSC Advances, 4*(62), 33013-33021.

119. Li, Z., Wang, C. (2013). Effects of working parameters on electrospinning *One-dimensional nanostructures* (pp. 15-28): Springer.

120. Martins, P., Lopes, AC., Lanceros-Mendez, S. (2014). Electroactive phases of poly (vinylidene fluoride): determination, processing and applications. *Progress in polymer science, 39*(4), 683-706.

121. Chinaglia, D., Gregorio, R., Stefanello, J., Pisani Altafim, R., Wirges, W., Wang, F., Gerhard, R. (2010). Influence of the solvent evaporation rate on the crystalline phases of solution- cast poly (vinylidene fluoride) films. *Journal of Applied Polymer Science, 116*(2), 785-791.

122. Andrew, J., Clarke, DR. (2008). Effect of electrospinning on the ferroelectric phase content of polyvinylidene difluoride fibers. *Langmuir, 24*(3), 670-672.

123. Derringer, G. C., Suich, R. (1980). Simultaneous Optimization of Several Response Variables. *Journal of Quality Technology*, *12*(4), 214-219.

124. Yaqoob, U., Uddin, A. I., & Chung, G.-S. (2016). The effect of reduced graphene oxide on the dielectric and ferroelectric properties of PVDF–BaTiO 3 nanocomposites. *RSC Advances, 6*(36), 30747-30754.

125. Shahriary, L., & Athawale, A. A. (2014). Graphene oxide synthesized by using modified hummers approach. *Int. J. Renew. Energy Environ. Eng, 2*(01), 58-63.

126. Duan, W. H., Wang, Q., & Quek, S. T. (2010). Applications of piezoelectric materials in structural health monitoring and repair: Selected research examples. *Materials, 3*(12), 5169-5194.

127. Lessing, J., Glavan, A. C., Walker, S. B., Keplinger, C., Lewis, J. A., & Whitesides, G. M. (2014). Inkjet Printing of Conductive Inks with High Lateral Resolution on Omniphobic "RF Paper" for Paper‐ Based Electronics and MEMS. *Advanced Materials, 26*(27), 4677-4682.

128. Silverbrook, K. (2006). Inkjet printer comprising MEMS temperature sensors: Google Patents.

129. Feng, D., Yan, Y., Yang, X., Jin, G., & Fan, S. (2005). Novel integrated light‐guide plates for liquid crystal display backlight. *Journal of optics A: pure and applied optics, 7*(3), 111.

130. Huang, L., Huang, Y., Liang, J., Wan, X., & Chen, Y. (2011). Graphene-based conducting inks for direct inkjet printing of flexible conductive patterns and their applications in electric circuits and chemical sensors. *Nano Research, 4*(7), 675-684.

131. Abe, K., Suzuki, K., & Citterio, D. (2008). Inkjet-printed microfluidic multianalyte chemical sensing paper. *Analytical chemistry, 80*(18), 6928-6934.

132. Yin, Z., Huang, Y., Bu, N., Wang, X., & Xiong, Y. (2010). Inkjet printing for flexible electronics: Materials, processes and equipments. *Chinese Science Bulletin, 55*(30), 3383-3407. doi: 10.1007/s11434-010-3251-y

133. Singh, M., Haverinen, H. M., Dhagat, P., & Jabbour, G. E. (2010). Inkjet printing—process and its applications. *Advanced Materials, 22*(6), 673-685.

134. Fouad, O., Ismail, A., Zaki, Z., & Mohamed, R. (2006). Zinc oxide thin films prepared by thermal evaporation deposition and its photocatalytic activity. *Applied Catalysis B: Environmental, 62*(1), 144-149.

135. Ponzoni, A., Comini, E., Ferroni, M., & Sberveglieri, G. (2005). Nanostructured WO 3 deposited by modified thermal evaporation for gas-sensing applications. *Thin Solid Films, 490*(1), 81-85.

136. Liu, M., Johnston, M. B., & Snaith, H. J. (2013). Efficient planar heterojunction perovskite solar cells by vapour deposition. *Nature, 501*(7467), 395-398.

137. Zhang, Y. (2014). *Piezoelectric Based Energy Harvesting on Low Frequency Vibrations of Civil Infrastructures.*

138. Peigney, M., & Siegert, D. (2013). Piezoelectric energy harvesting from traffic-induced bridge vibrations. *Smart materials and Structures, 22*(9), 095019.

139. Kon, S., Oldham, K., & Horowitz, R. (2007). *Piezoresistive and piezoelectric MEMS strain sensors for vibration detection.* Paper presented at the Proc. SPIE.

140. Zhao, X., Gao, H., Zhang, G., Ayhan, B., Yan, F., Kwan, C., & Rose, J. L. (2007). Active health monitoring of an aircraft wing with embedded piezoelectric sensor/actuator network: I. Defect detection, localization and growth monitoring. *Smart materials and Structures, 16*(4), 1208.

141. Rathod, V., & Mahapatra, D. R. (2011). Ultrasonic Lamb wave based monitoring of corrosion type of damage in plate using a circular array of piezoelectric transducers. *NDT & E International, 44*(7), 628-636.

142. Feucht, G., Schleicher, A., & Frank, G. (2001). Piezoelectric gas sensor: Google Patents.

143. Giurgiutiu, V. (2005). Tuned Lamb wave excitation and detection with piezoelectric wafer active sensors for structural health monitoring. *Journal of Intelligent material systems and structures, 16*(4), 291-305.

144. Diamanti, K., & Soutis, C. (2010). Structural health monitoring techniques for aircraft composite structures. *Progress in Aerospace Sciences, 46*(8), 342-352.

145. Raghavan, A., & Cesnik, C. E. (2007). Review of guided-wave structural health monitoring. *Shock and Vibration Digest, 39*(2), 91-116.

146. Chen, X., Guo, S., Li, J., Zhang, G., Lu, M., & Shi, Y. (2013). Flexible piezoelectric nanofiber composite membranes as high performance acoustic emission sensors. *Sensors and Actuators A: Physical, 199*, 372-378.

VITA

Ehsan Ghafari earned his B.Sc. from Azad University, his M.Sc. from International University of Imam Khomeini and his Ph.D. from Technical University of Lisbon. He joined Civil Engineering Materials Group at Purdue University in spring 2015. Ehsan's doctoral thesis aimed to investigate the feasibility of using a piezoelectric material/device for sensing/energy harvesting in civil infrastructure applications. During graduate study, he has received Goetz Graduate research award and ACPA concrete pavement research scholarship for his research. His research interests include (1) developing novel characterization, sensing, and nondestructive evaluation techniques, (2) developing novel materials and devices for energy harvesting in civil infrastructure and (3) advanced and sustainable cementitious materials for civil infrastructure.